MICROCOPY RESOLUTION TEST CHART

NATIONAL BUREAU OF STANDARDS-1963-A

ADVANCED SIMULATION RESEARCH

Volume II — Vacuum Energy Storage

Maxwell Laboratories, Inc.
9244 Balboa Avenue
San Diego, California 92123

30 September 1975

Final Report for Period 1 August 1974—31 July 1975

CONTRACT No. DNA 001-74-C-0012

Prepared for

Director

DEFENSE NUCLEAR AGENCY

Washington, D. C. 20305

REPORT DOCUMENTATION PAGE		READ INSTRUCTIONS BEFORE COMPLETING FORM
1. REPORT NUMBER DNA 4297F-2	2. GOVT ACCESSION NO.	3. RECIPIENT'S CATALOG NUMBER
4. TITLE (and Subtitle) ADVANCED SIMULATION RESEARCH. Volume II—Vacuum Energy Storage.		5. TYPE OF REPORT & PERIOD COVERED Final Report for Period 1 Aug 74—31 Jul 75
		6. PERFORMING ORG. REPORT NUMBER MLR-498
7. AUTHOR(s) W. Clark, A. Mondelli P. Korn, N. Rostoker		8. CONTRACT OR GRANT NUMBER(s) DNA 001-74-C-0012
9. PERFORMING ORGANIZATION NAME AND ADDRESS Maxwell Laboratories, Inc. 9244 Balboa Avenue San Diego, California 92123		10. PROGRAM ELEMENT, PROJECT, TASK AREA & WORK UNIT NUMBERS Subtask T99QAXLA014-25
11. CONTROLLING OFFICE NAME AND ADDRESS Director Defense Nuclear Agency Washington, D.C. 20305		12. REPORT DATE 30 Sep 75
		13. NUMBER OF PAGES 152
14. MONITORING AGENCY NAME & ADDRESS(if different from Controlling Office)		15. SECURITY CLASS. (of this report) UNCLASSIFIED
		15a. DECLASSIFICATION/DOWNGRADING SCHEDULE

16. DISTRIBUTION STATEMENT (of this Report)

Approved for public release, distribution unlimited.

17. DISTRIBUTION STATEMENT (of the abstract entered in Block 20, if different from Report)

18. SUPPLEMENTARY NOTES

This work sponsored by the Defense Nuclear Agency under Subtask T99QAXLA01425.

19. KEY WORDS (Continue on reverse side if necessary and identify by block number)

Theoretical Program
Magnetic Field
Diverter Loop
Azimuthal Drift

20. ABSTRACT (Continue on reverse side if necessary and identify by block number)

The STP experiment has been placed in operation during this contract period. A number of electron injectors have been explored with the injected charge shown to scale linearly with the injector bias voltage. Injected charge levels ~100 micro-coulombs, which corresponds to potential well depths of ~300 kV, have been measured as will be described in this report. Vertical magnetic field coils have been installed on the experiment, and preparations for high-energy electron injection have been completed.

DD FORM 1473 EDITION OF 1 NOV 65 IS OBSOLETE
1 JAN 73

20. ABSTRACT (Continued)

Theoretical studies of high-energy injection, including single-particle and fully-relativistic self-consistent calculations, are presented. In addition, a theoretical study of switching energy stored in the torus is reported.

ACCESSION for

NTIS	White Section	
DDC	Buff Section	☐
UNANNOUNCED		☐
JUSTIFICATION		

BY
DISTRIBUTION/AVAILABILITY CODES

| Dist. | AVAIL. and/or SPECIAL |
| A | | |

CONTENTS

ILLUSTRATIONS

3

4

SECTION 7

VACUUM ENERGY STORAGE

7.1   THEORETICAL PROGRAM

Theoretical consideration of high-energy electron beam injection and switching for the DNA Small Toroidal Pulseline (STP) have been actively pursued during the past year. In addition, investigation of the equilibrium of an unneutralized electron beam using a fully relativistic rigid rotor model as well as the development of a set of relativistic fluid equations for further equilibrium and stability calculations are reported. Fully relativistic equilibria are required to study the entire equilibrium parameter space, including the regime where the perpendicular motion is relativistic. In this domain the theoretical bounds on stored charge and ν/γ consistent with equilibrium at a given value of magnetic guide field can be properly explored. To extend our ability to calculate equilibria and stability in a realistic toroidal geometry requires the development of a set of fluid equations for non-neutral, relativistic plasma. A two-mass realization of such a set of equations is presented in this report.

In addition to the self-consistent equilibrium calculations, a computer code has been developed to facilitate the design of an energetic electron injector. This code calculates the trajectory of a test electron from the fully-relativistic equations of motion in toroidal geometry. The self-consistent equilibrium fields of a core of background electrons are included, as well as a toroidal magnetic guide field, a vertical magnetic field and a diverter field. This code permits a study of the electron dynamics in the torus. The importance of vertical field for canceling the electron drifts due to toroidal curvature and grad B will be reported.

Finally, a means of switching the torus through the use of vertical magnetic fields will be presented. A design for achieving the required switching time will be shown in detail.

7

7.1.1 High-Energy Electron Injection for STP

A relativistic electrostatic torus can store γ_o times more charge or γ_o^2 times more field energy than is possible is a non-relativistic system of the same dimensions for a given magnetic field strength. To realize these advantages, however, the electrons must be injected with relativistic energy. The fundamental limit on stored charge derives from the condition for crossed-field electron drift to be energetically possible. In the presence of the space-charge electrical field, E_r, the self-magnetic field, B_θ, and the toroidal guide field, B_ω, the electrons execute a poloidal drift with velocity v_θ given by

$$\frac{v_\theta}{c} = - \frac{E_r - \beta_o B_\theta}{B_\omega} = - \frac{E_r}{\gamma_o^2 B_\omega}$$

where $B_\theta = \beta_o E_r$ and $\gamma_o = (1 - \beta_o^2)^{-1/2}$. The total kinetic energy of the electron, including the poloidal drift, is given by

$$\gamma = [1 - \beta_o^2 - (v_\theta/c)^2]^{-1/2} = \frac{\gamma_o}{\sqrt{1 - \left(\frac{\gamma_o v_\theta}{c}\right)^2}} \, ,$$

from which we obtain the condition $\gamma_o v_\theta/c < 1$. For $\gamma_o v_\theta/c = 1$, the kinetic energy of the electron is infinite since this corresponds to $v'_\theta = \gamma_o v_\theta = c$ in the reference frame where the axial beam velocity is zero.

The energy for the drift motion is drawn from the stored field energy and presents an "energy penalty" when $\gamma_o v_\theta/c$ is near unity. The fractional energy, $(\gamma - \gamma_o)/\gamma_o$, is plotted in Figure 7-1 as a function of $\gamma_o v_\theta/c$. From the figure we see that for $\gamma_o v_\theta/c \le 1/2$ when the last electron is injected at the torus wall we obtain conservative design criterion for a relativistic injection system. As the electrons are magnetically compressed away from the wall, the value of $\gamma_o v_\theta/c$ decreases linearly with radius. The theoretical maximum for $\gamma_o v_\theta/c$ can be determined by
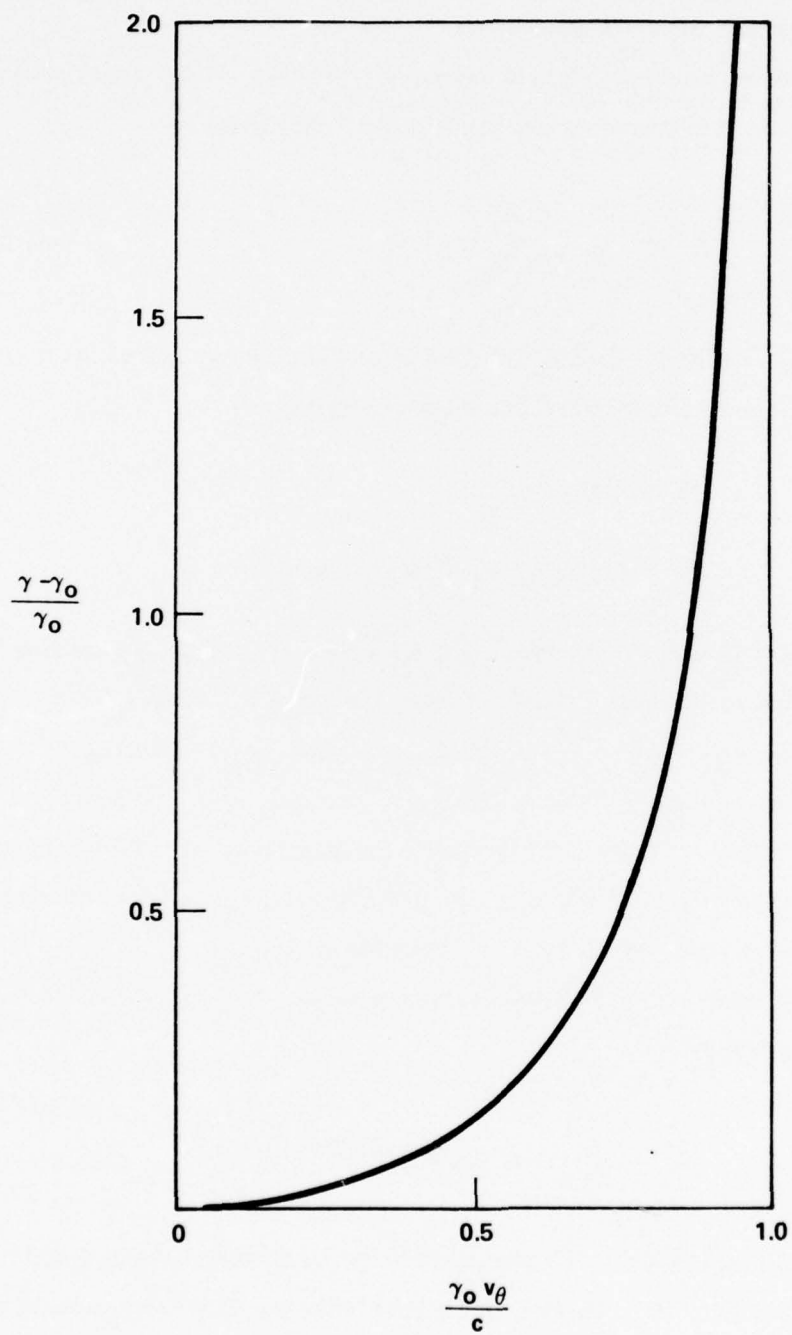
Figure 7-1. Fractional Kinetic Energy vs. $\gamma_0 v_\theta / c$.

9

studying fully-relativistic beam equilibria. Such studies have been made and will be discussed in a separate section of this report.

If we denote the maximum allowed values of $\gamma_o v_\theta / c$ by η, we obtain an expression for the maximum stored charge in the device. We write

$$\frac{\gamma_o v_\theta}{c} = - \frac{E_r}{\gamma_o B_\theta} = \eta$$

and use $E_r = - 2N_b e / b$ with $Q = 2\pi R \, N_b e$ and $r = b$ for the minor radius of the torus. The resulting expression for the maximum stored charge is

$$Q = \eta \pi R \, b \, \gamma_o B_\theta$$

$$= 0.424 \; \eta \gamma_o B_\theta \; (kG) \; \text{millicoulombs.}$$

The second line here uses $R = 50$ cm and $b = 8.1$ cm, which are typical parameters for the STP. This expression is plotted in Figure 7-2 for $\eta = 0.5$ and $B_\theta = B_o$ $\sin (\pi t / 2\tau)$. On this figure we observe that for $B_o = 10$ kG we can inject up to 2.1 mC with $\gamma_o = 1$, provided we inject electrons all the way to peak field. To compress the electrons away from the wall, we must terminate the injection prior to the time of peak field, with a corresponding reduction in injected charge. By using a relativistic injector, $\gamma_o > 1$, we increase the allowed charge by the factor γ_o.

For a given value of injected charge, Q, the energy stored in the fields of the electron beam is given by

$$W_f = \frac{Q^2}{2\pi R} \; (1 + \beta_o^{\,2}) \; [\, 1/4 + \ln b/a \,]$$

where a = the final beam radius. We assume Q is the maximum allowed, i.e., $Q = \eta \pi R \, b \gamma_o B_o \sin (\pi t_f / 2\tau)$, where t_f is the time when the final electron is injected. The final beam radius, a, is then given by

10
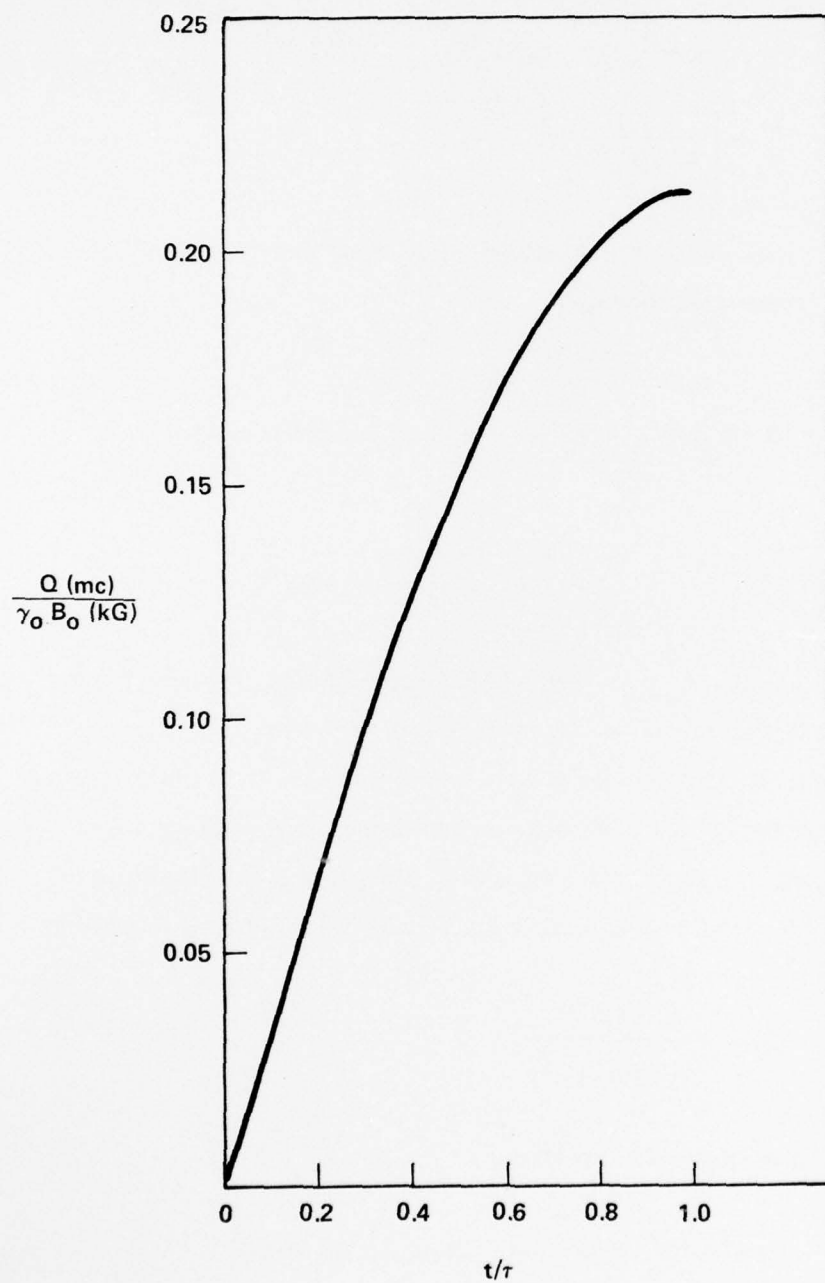
Figure 7-2. Maximum Stored Charge vs. Time for $\eta = 0.5$.

11

$$a^2 B_o = b^2 B_o \sin(\pi t_f / 2\tau)$$

or

$$\frac{b}{a} = \left[\frac{1}{\sin(\pi t_f / 2\tau)} \right]^{1/2} .$$

Combining these results, we obtain an expression for the final stored field energy in terms of the injection termination time t_f,

$$W_f = \frac{\eta^2}{8} (1 + \beta_o^2) \pi R b^2 \gamma_o^2 B_o^2 \sin^2(\pi t_f / 2\tau) [1 - 2\ln \sin(\pi t_f / 2\tau)]$$

or

$$W_f = 257.65 \eta^2 \gamma_o^2 B_o^2 (kG) \sin^2(\pi t_f / 2\tau) [1 - 2\ln \sin(\pi t_f / 2\tau)] \text{ Joules}$$

for R = 50 cm, b = 8.1 cm and $\beta_o^2 \simeq 1$. This expression is plotted in Figure 7-3 for $\eta = 0.5$. We see that the stored energy increases with t_f as we would expect.

We now turn to a calculation of the power density available from switching such a device. A mechanism for switching the beam in one transit time is described in detail in a later section of this report. If the final field energy, W_f, calculated above is released in one transit time, $2\pi R/c$, the power delivered per unit area is given by

$$P = \frac{W_f}{(2\pi R/c)(\pi a^2)} .$$

Using earlier results, this expression becomes,

$$P = \frac{\eta^2 c}{16\pi} (1 + \beta_o^2) \gamma_o^2 B_o^2 \sin(\pi t_f / 2\tau) [1 - 2\ln \sin(\pi t_f / 2\tau)]$$

$$= 1.2 \times 10^8 \eta^2 \gamma_o^2 B_o^2 (kG) \sin(\pi t_f / 2\tau) [1 - 2\ln \sin(\pi t_f / 2\tau)] \text{ Watts/cm}^2 .$$
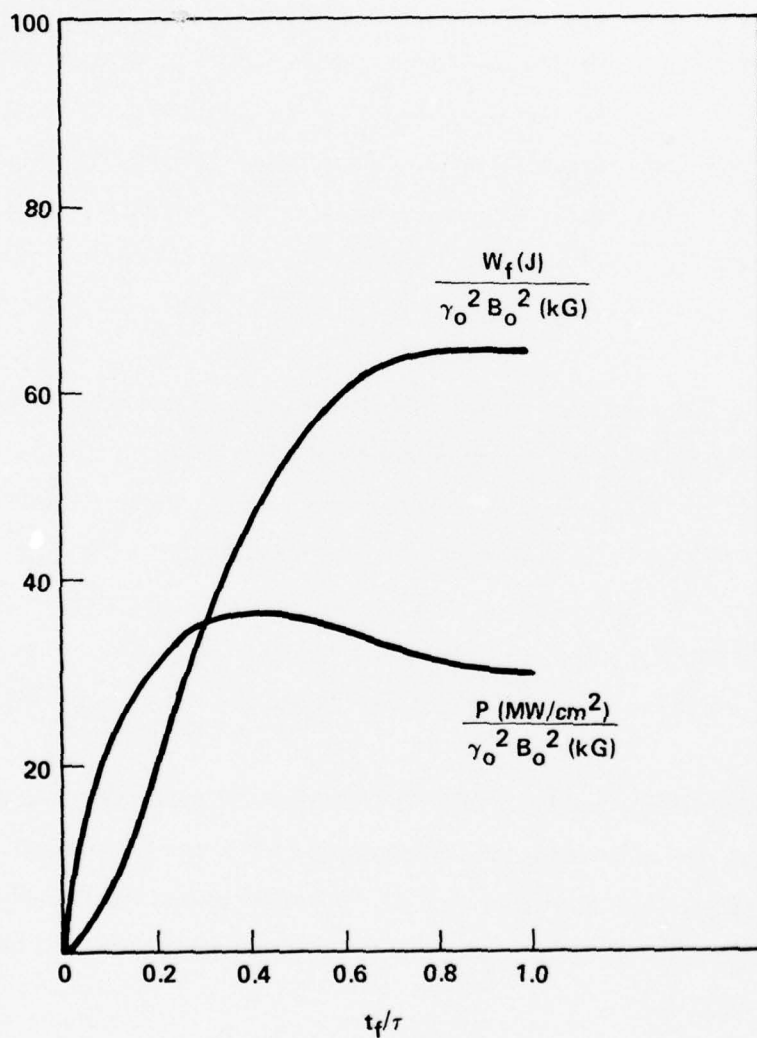
Figure 7-3. Stored Field Energy and Output Power Density Versus
Injection Termination. Time for $\eta = 0.5$.

13

This expression is also plotted on Figure 7-3 for $\eta = 0.5$, and the result shows a peak in output power density when injection is terminated at $t_f/\tau \simeq 0.4$. The peak occurs because earlier termination of injection leads to a more tightly-pinched beam, but also results in less stored energy. We should emphasize that these results are valid as long as the drift limit, $\gamma_o v_\theta/c \leq \eta$, is the most stringent limit on charge injection.

We now examine Figures 7-2 and 7-3 to determine a set of design parameters for a relativistic STP. Assume that we terminate injection at the maximum output power point, $t_f/\tau \simeq 0.4$, and use $B_o = 10$ kG (the STP field coils can reach 12-15 kG). The non-relativistic thermionic injector is then limited to 1.2 mC stored charge corresponding to 4.5 kJ stored field energy. With a relativistic injector consisting of a low-current beam of 1 MeV electrons ($\gamma_o = 3$), the stored charge will be limited to 3.6 mC and 40 kJ will be stored in the self-fields of the beam. The final beam radius will be 6.2 cm.

The remainder of this section will present some simple estimates of the type of injection system required. Detailed studies of the relativistic injector are under way to examine the electron trajectories for various injector geometries using a single-particle model for the injected beam, but including the self-fields of electrons already in the torus. For a low-current injector, such a model yields a reliable calculation of the injected electron trajectories. The estimates to be presented below, therefore, should be regarded as an order-of-magnitude survey of the injector requirements.

Consider an injected beam of 1 MeV electrons with current i and pulse duration τ_p. The beam radius is assumed to be approximately 1 cm. The inductance of such a beam of length $2\pi R$ is of order $L \sim 1 \mu H$. Since the beam transit time around the torus is $2\pi R/c \sim 10$ ns, the rate at which the total current I within the torus increases is approximately

$$\frac{dI}{dt} \simeq \frac{i}{2\pi R/c} .$$

14

Clearly, a multi-turn injection is mandatory. The induced emf, L(dI/dt), associated with injection of the beam must be balanced by the transformer. Without a transformer, the induced emf would stop the beam before injection could be completed. If the injection current, i, is too large, the induced emf will not be completely cancelled by the transformer, and the beam would be degraded in energy during injection. The STP transformer can produce $V_L \simeq 3$ kV around the torus. We therefore have

$$L \frac{dI}{dt} \simeq (10^{-6} \text{ H}) \frac{i \text{ (Amps)}}{10^{-8} \text{ sec}} \simeq 3 \times 10^3 \text{ Volts}$$

or

$$i \simeq 30 \text{ Amps}$$

for the average injection current. From our earlier considerations, we wish to inject $Q \simeq 3.6$ mC into the torus. Since this charge is provided by the injector, we must require

$$Q = i \tau_p$$

which determines the injection pulse duration,

$$\tau_p \simeq 120 \text{ } \mu s.$$

The magnetic field typically rises in $\tau \simeq 3.5$ ms, and for injection to terminate at $t_f/\tau \simeq 0.4$, we have $t_f \simeq 1.4$ ms, which allows ample room for an injection window. A lower injection current with a longer pulse duration may be preferable for obtaining uniformity in the final beam, and would be compatible with the transformer.

7.1.2 Single-Particle Orbit Calculations

A computer code has been developed to facilitate the design of a relativistic injection system for an electrostatic torus. The trajectory of a test electron is computed using the fully relativistic equations of motion in toroidal geometry. A thermionic (or other) injector is assumed to have supplied a core of charge within the torus at the

15

time the relativistic electron is injected. This core provides a rotational transform in the particle orbits to cancel the vertical drift due to the centrifugal and grad B forces. Vertical magnetic field can also be utilized to cancel the vertical drifts, thereby eliminating the need for rotational transform. The fields due to the core electrons are computed from self-consistent equilibrium solutions. The electrostatic and self-magnetic fields of the core electrons, including the diamagnetic contribution to the toroidal field are all present in the equations of motion. In addition, the code provides for a loop diverter field to distort the magnetic field lines in the vicinity of the injector, and a vertical field to adjust the equilibrium location.

The following parameters are input variables in the code, and are therefore arbitrary:

1. <u>Test Electron</u>

      initial position of the test electron

      initial energy of the test electron

      direction of the initial momentum vector of the test electron

2. <u>Electron Cloud</u>

      quantity of previously injected charge

      radius of the electron cloud

      relativistic factor (γ_o) of the electron cloud

3. <u>Geometry of the Toroidal Vessel</u>

      major radius and minor radius

4. <u>Diverter Loop Quantities</u>

      current in loop

      radius of loop

      location of loop center

      direction of loop axis

5. <u>Guide Field, $B_o \sin (\pi t/2\tau)$</u>

      B_o and τ

6. Initial and Final Time in Computer Run and Time Step for Integration of Equations of Motion

7. Vertical Field, B_v

Coordinates

Figure 7-4 shows the toroidal coordinate system as well as local and global cartesian coordinates. The problem is solved in the global cartesian system in order to facilitate the inclusion of the diverter field, which is non-toroidal. The transformation from toroidal coordinates (r, θ, φ) to global cartesian coordinates (x, y, z) is given by

$$x = R \cos \varphi$$
$$y = -R \sin \varphi$$
$$z = r \sin \theta.$$

where $R = R_o + r \cos \theta$. The inverse transformation is

$$R = \sqrt{x^2 + y^2}$$
$$\tan \varphi = -y/x$$
$$r = \sqrt{(R - R_o)^2 + z^2}$$
$$\tan \theta = z/(R - R_o).$$

The unit vectors in the global cartesian system are

$$\hat{e}_x = \hat{e}_r \cos \theta \cos \varphi - \hat{e}_\theta \sin \theta \cos \varphi - \hat{e}_\varphi \sin \varphi$$
$$\hat{e}_y = -\hat{e}_r \cos \theta \sin \varphi + \hat{e}_\theta \sin \theta \sin \varphi - \hat{e}_\varphi \cos \varphi$$
$$\hat{e}_z = \hat{e}_r \sin \theta + \hat{e}_\theta \cos \theta.$$

17
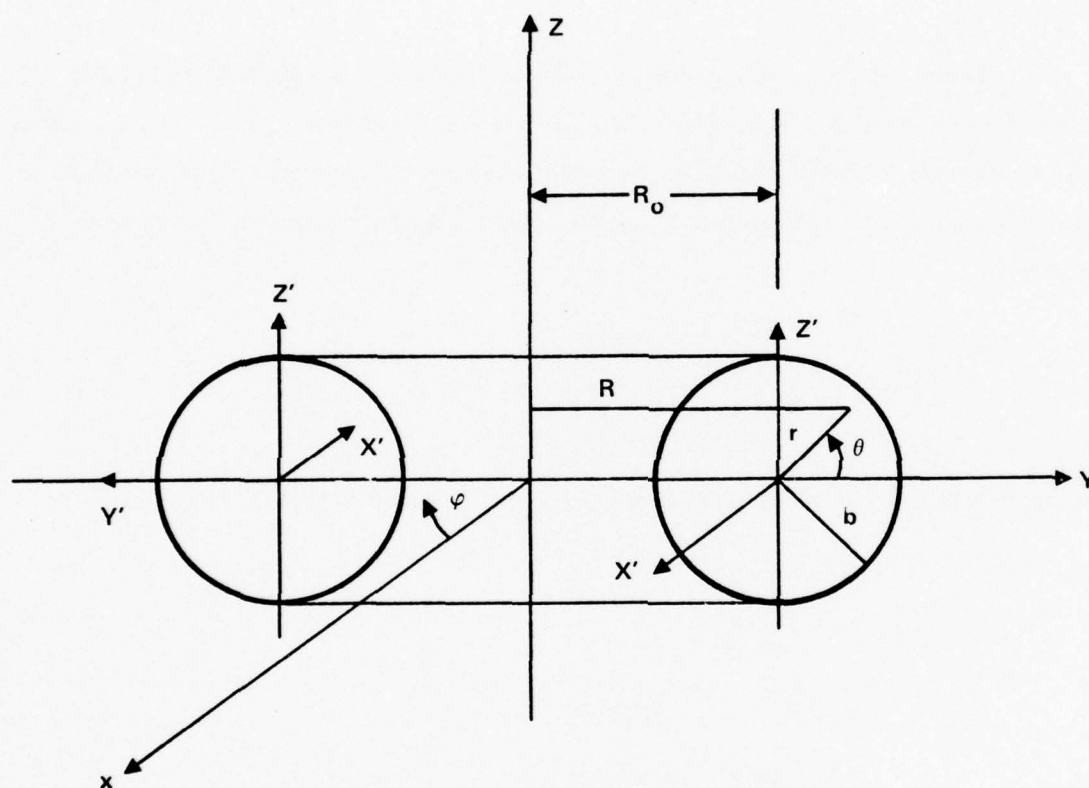
Figure 7-4. Toroidal Geometry.

18

Given any vector, $\underline{A} = \hat{e}_r A_r + \hat{e}_\theta A_\theta + \hat{e}_\wp A_\wp$, in toroidal coordinates, the components in global cartesian coordinates are

$$A_x = \hat{e}_x \cdot \underline{A} = (A_r \cos\theta - A_\theta \sin\theta)\cos\wp - A_\wp \sin\wp$$

$$A_y = \hat{e}_y \cdot \underline{A} = -A_\wp \cos\wp - (A_r \cos\theta - A_\theta \sin\theta)\sin\wp$$

$$A_z = \hat{e}_z \cdot \underline{A} = A_r \sin\theta + A_\theta \cos\theta.$$

Fields

The code is written entirely in the cgs-Gaussian electrostatic system of units. The self fields of the electron cloud are

$$E_r = \frac{Q}{\pi R_o a} \begin{cases} r/a & r \leq a \\[2em] a/r & a \leq r \leq b \end{cases}$$

$$B_\theta = \beta_o E_r.$$

The toroidal guide field with the diamagnetic contribution of the electron cloud is given by

$$B_\wp \begin{cases} B_o \sin(\pi t/2\tau)\left[1 - \left(\dfrac{Q}{\pi R_o a^2}\right)^2 (1 - r^2/a^2)\right]\dfrac{R_o}{R} & r \leq a \\[2.5em] \dfrac{R_o}{R} B_o \sin(\pi t/2\tau) & a \leq r \leq b. \end{cases}$$

In addition, there is an inductive electric field, E_θ, due to the time dependence of $B_\wp$

$$E_\theta = -\frac{r}{2c}\frac{\partial B_\wp}{\partial t} \cong -\frac{r}{2c}\left(\frac{\pi B_o}{2\tau}\right)\cos\left(\frac{\pi t}{2\tau}\right).$$

Diverter Loop

The diverter is modeled as a single-turn filamentary loop. Later versions of the code will stack such loops into a finite-length solenoidal field. The diverter field is calculated in the coordinate system shown in Figure 7-5. The vector $\underline{\zeta}$ defines the axis of the loop as well as the direction of current flow in the loop (by the righthand rule). The loop radius, a_ℓ, and the current in the loop, I_ℓ, are input variables in the code. In addition, we specify the location of the center of the loop $(r_\ell, \theta_\ell, \omega_\ell)$ and the coordinates of an arbitrary point on the positive half of the loop axis $(r_{ax}, \theta_{ax}, \omega_{ax})$. The point at which we wish to know the field is (r, θ, ω). Using the transformation equations, we find the coordinates of these points in the global cartesian system

$$(r_\ell, \theta_\ell, \omega_\ell) \rightarrow (x_\ell, y_\ell, z_\ell)$$

$$(r_{ax}, \theta_{ax}, \omega_{ax}) \rightarrow (x_{ax}, y_{ax}, z_{ax})$$

$$(r, \theta, \omega) \rightarrow (x, y, z)$$

We define

$$\underline{\zeta} = (x_{ax} - x_\ell, \ y_{ax} - y_\ell, \ z_{ax} - z_\ell)$$

$$\underline{\rho} = (x - x_\ell, \ y - y_\ell, \ z - z_\ell)$$

where $\underline{\rho}$ is the vector pointing from the center of the loop to the field point. The loop field is then given by
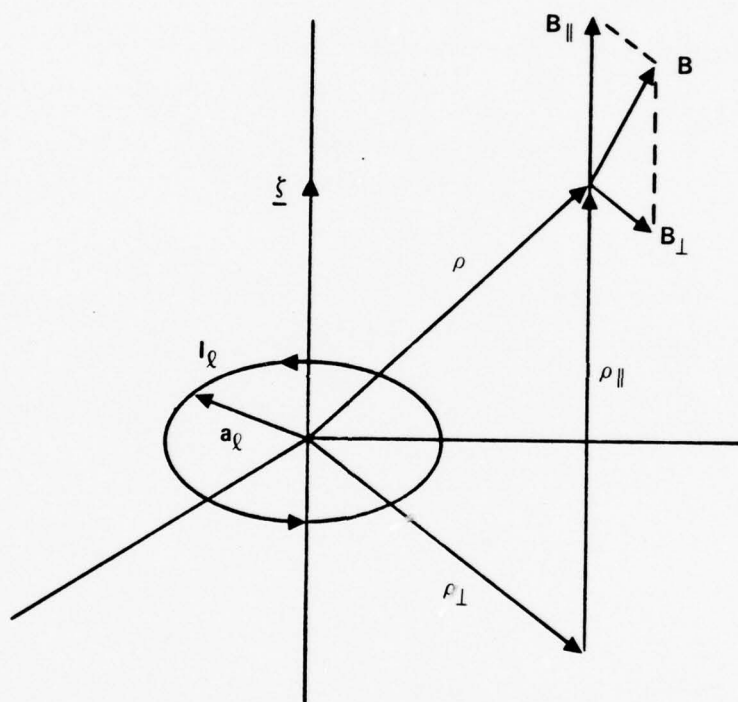
Figure 7-5. Loop Coordinates.

$$B_\perp = \frac{I_\ell}{c} \frac{2\rho_\parallel / \rho_\perp}{\sqrt{(a_\ell + \rho_\perp)^2 + \rho_\parallel^2}} \left[-K(k) + \frac{a_\ell^2 + \rho_\perp^2 + \rho_\parallel^2}{(a_\ell - \rho_\perp)^2 + \rho_\parallel^2} E(k) \right]$$

$$B_\parallel = \frac{I_\ell}{c} \frac{2}{\sqrt{(a_\ell + \rho_\perp)^2 + \rho_\parallel^2}} \left[K(k) + \frac{a_\ell^2 - \rho_\perp^2 - \rho_\parallel^2}{(a_\ell - \rho_\perp)^2 + \rho_\parallel^2} E(k) \right]$$

where $K(k)$ and $E(k)$ are the complete elliptic integrals,

$$K(k) \equiv \int_0^{\pi/2} \frac{d\alpha}{\sqrt{1 - k^2 \sin^2 \alpha}}$$

$$E(k) \equiv \int_0^{\pi/2} d\alpha \sqrt{1 - k^2 \sin^2 \alpha}$$

with

$$k^2 = \frac{4 a_\ell \rho_\perp}{(a_\ell + \rho_\perp)^2 + \rho_\parallel^2}$$

and

$$\rho_\parallel = \underline{\zeta} \cdot \underline{\rho} / \zeta$$

$$\rho_\perp = \sqrt{\rho^2 - \rho_\parallel^2} .$$

The loop field in the global cartesian coordinate system is then

$$\underline{B}_{loop} = B_\parallel \, \underline{\zeta} / \zeta + B_\perp \, \underline{\rho}_\perp / \rho_\perp$$

where

$$\underline{\rho}_\perp = \underline{\zeta} \times \underline{\rho} \times \underline{\zeta} / \zeta^2 .$$

22

Equations of Motion

The code solves the fully relativistic equations of motion,

$$\frac{dx}{dt} = \underline{v} = \frac{p}{m \sqrt{1 + p^2/m^2 c^2}}$$

$$\frac{dp}{dt} = -e \left[\underline{E} + \frac{1}{c} \ \underline{v} \times \underline{B} \right]$$

by a numerical integration technique similar to the classical Runge-Kutta procedure.

Output of Code

The code makes two plots, a projection of the electron trajectory in the x-y plane and a projection in the local x-z plane. These two plots provide the complete shape of the orbit. In addition, the code prints out the position and momentum components of the test electron at each time step, thereby allowing the time history of the particle to be followed.

We have run a number of simple problems in order to check the accuracy of the code. In one case, the calculation time step was reduced from 10^{-10} sec to 10^{-11} sec with no change in the output. In another example, we reversed the sign of the toroidal guide field and caused the toroidal curvature and grad B drifts to change direction.

One set of test calculations were of pure toroidal drifts. The torus was emptied, $Q = 0$, and the test electron launched in the toroidal direction with no initial momentum in either the radial or the azimuthal directions. The diverter loop was not activated, $I_{\ell} = 0$. In these calculations we expect the electron to execute an upward vertical drift with speed

$$v_z = \frac{\gamma_o \beta_o^2 mc^3}{e R_o B_\varphi} \ .$$

23

The results of these calculations are shown in Figures 7-6 through 7-8. In each case, the distance to wall is 7.746 cm, since the electron begins 2 cm off axis. From the known time of flight of the electron to the wall, we can calculate the electron drift speed, which we compare with the theoretical value. The following table summarizes the results.

Figure	γ	B_o (kG)	V_z (Theoretical) (cm/ns)	V_z (Computer) (cm/ns)
7-6	2	5	1.382	1.383
7-7	3	5	2.456	2.421
7-8	3	10	1.228	1.229

The small differences between the computed and theoretical values of v_z are entirely consistent with the finite Larmor radius effects which are included in the code. The largest deviation, Figure 7-7, corresponds to the largest Larmor radius.

In the next set of test calculations, we constructed HIPAC equilibria. The test electron started at rest, 2 cm off the minor axis. The torus contained a finite amount of charge, Q, and the azimuthal electron drift was expected with speed

$$v_\theta = \omega r$$

$$\omega = \frac{Qc}{\pi R_o a^2 B_o}.$$

Figure 7-9 shows the result for Q = 10 μC and $\gamma_o = 1.0001$ for the electron cloud. The test electron executed a perfect azimuthal drift. The calculated precession half-period, π / ω, was 9.75 ns, and the test electron required 9.6 ns to precess half way around the minor axis. The calculated Larmor period and Larmor radius also agreed with the computer results.

Figure 7-10 shows the same calculation with Q = 100 μC. The orbits are larger and the precession faster, as expected. Both Figures 7-9 and 7-10 represent 10 ns of electron travel. In Figure 7-11, we repeat the calculation with Q = 100 μC, but now

58

Y

0

-58
-58   0   58
X

Q   = 0
γ   = 2
B$_O$ = 5KG

8

Z′

0

-8
-8   0   8
Y′

Q   = 0
γ   = 2
B$_O$ = 5KG
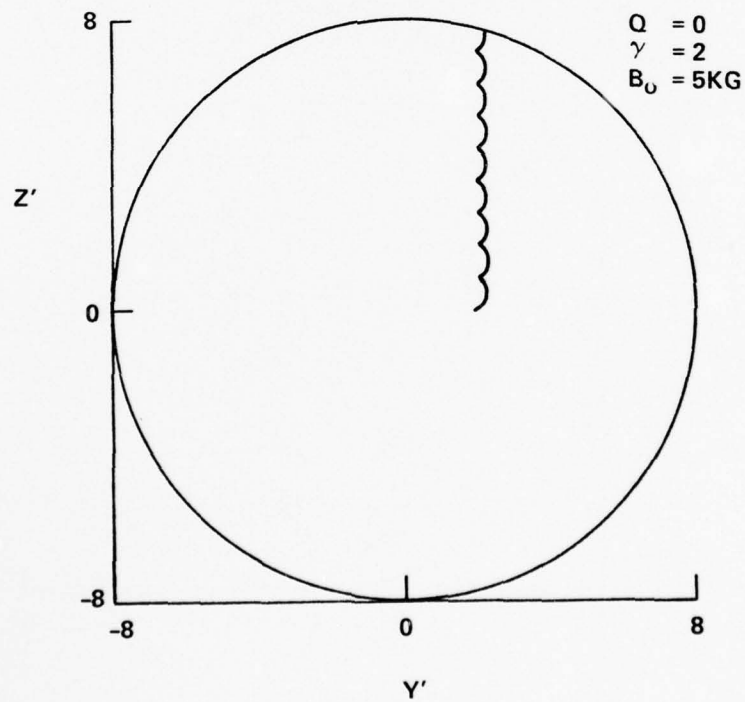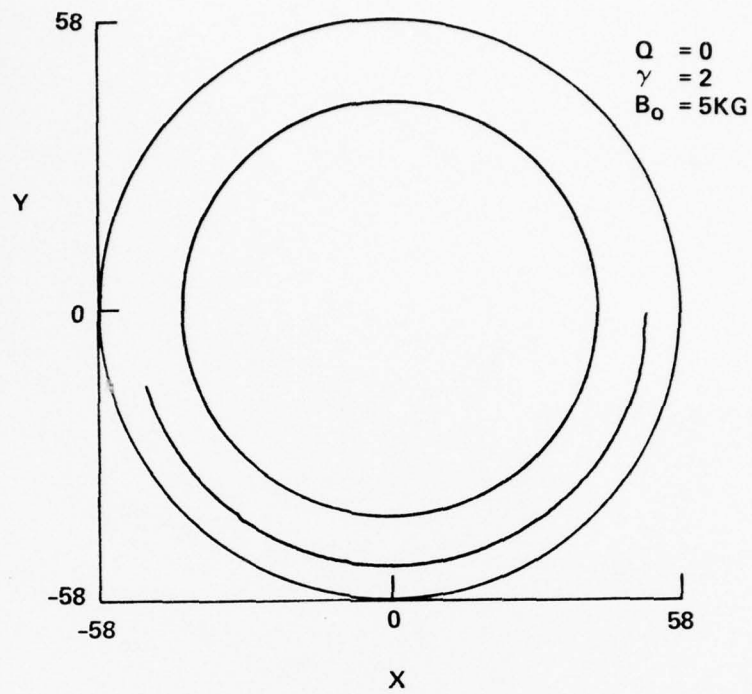
Figure 7-6. Vertical Drift γ = 2, B$_O$ = 5 kG.
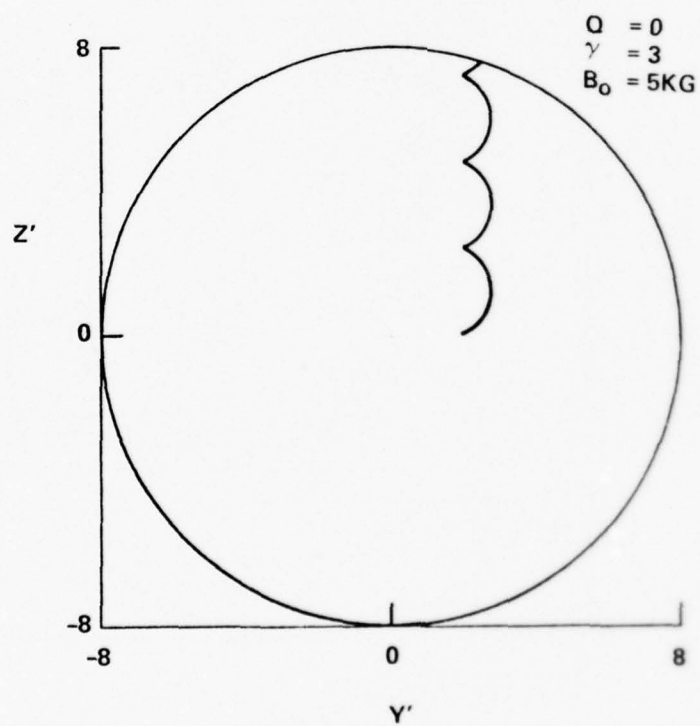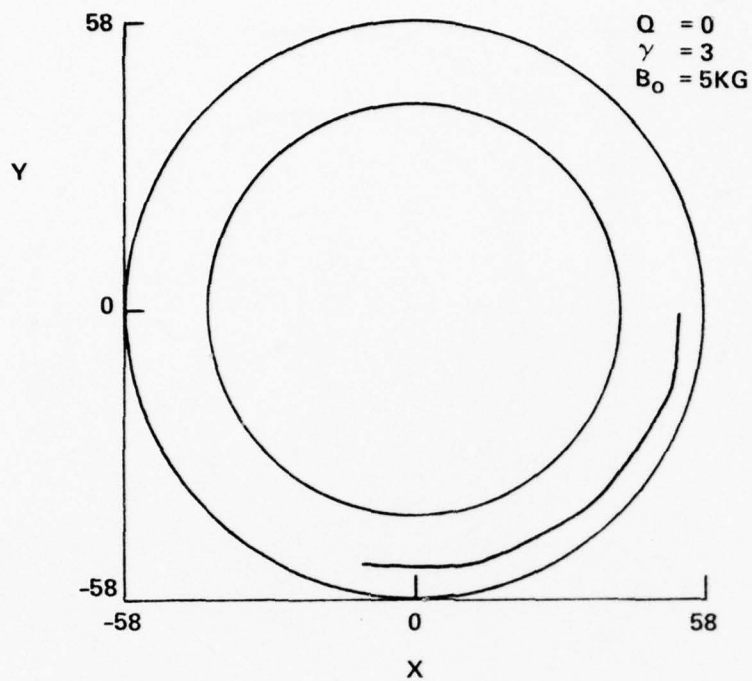
Figure 7-7. Vertical Drift $\gamma = 3$, $B_o = 5$ kG.

26
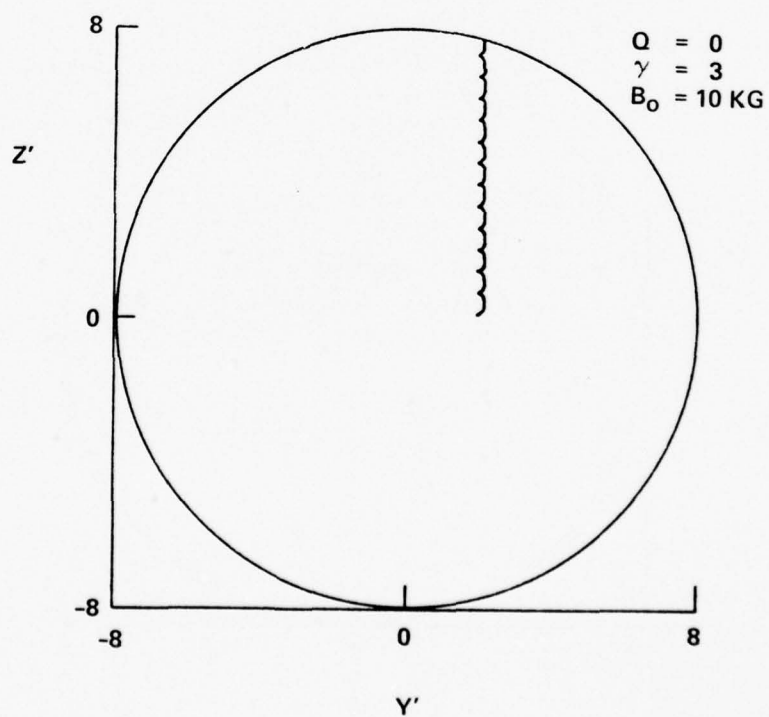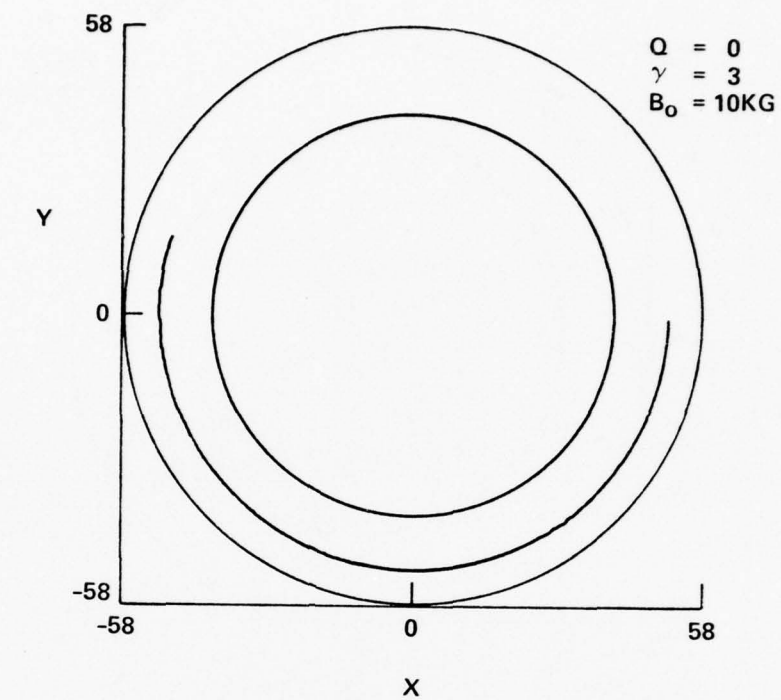
Figure 7-8. Vertical Drift $\gamma = 3$, $B_o = 10$ kG.
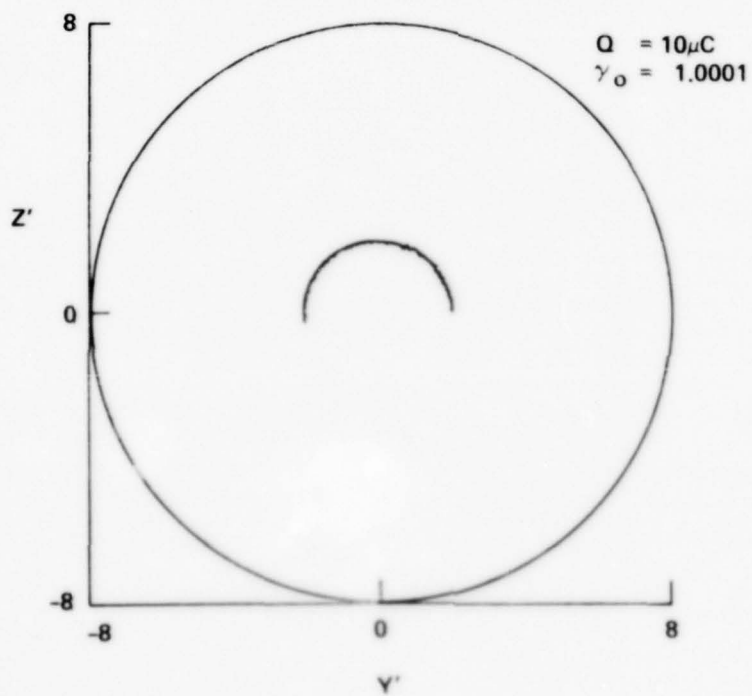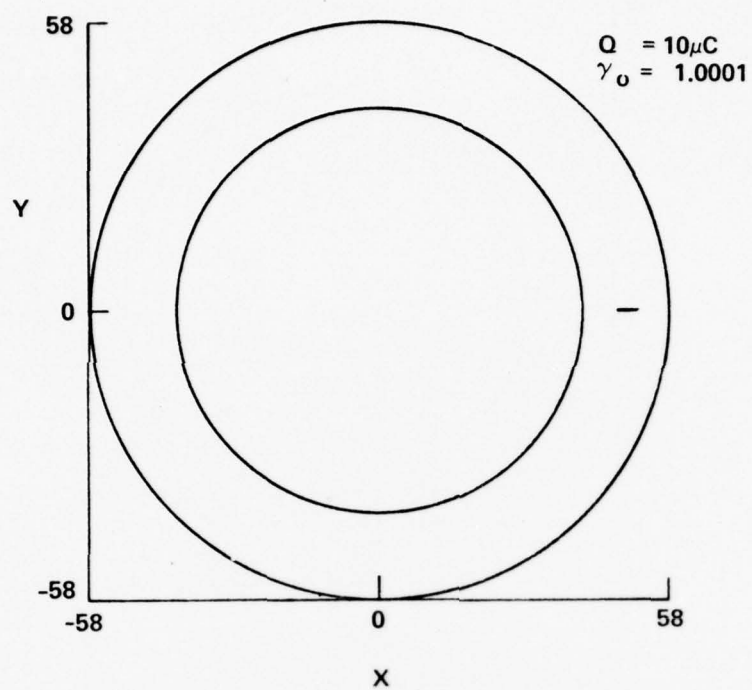
Figure 7-9. Azimuthal Drift $Q = 10 \mu c$, $\gamma_o = 1.0001$.
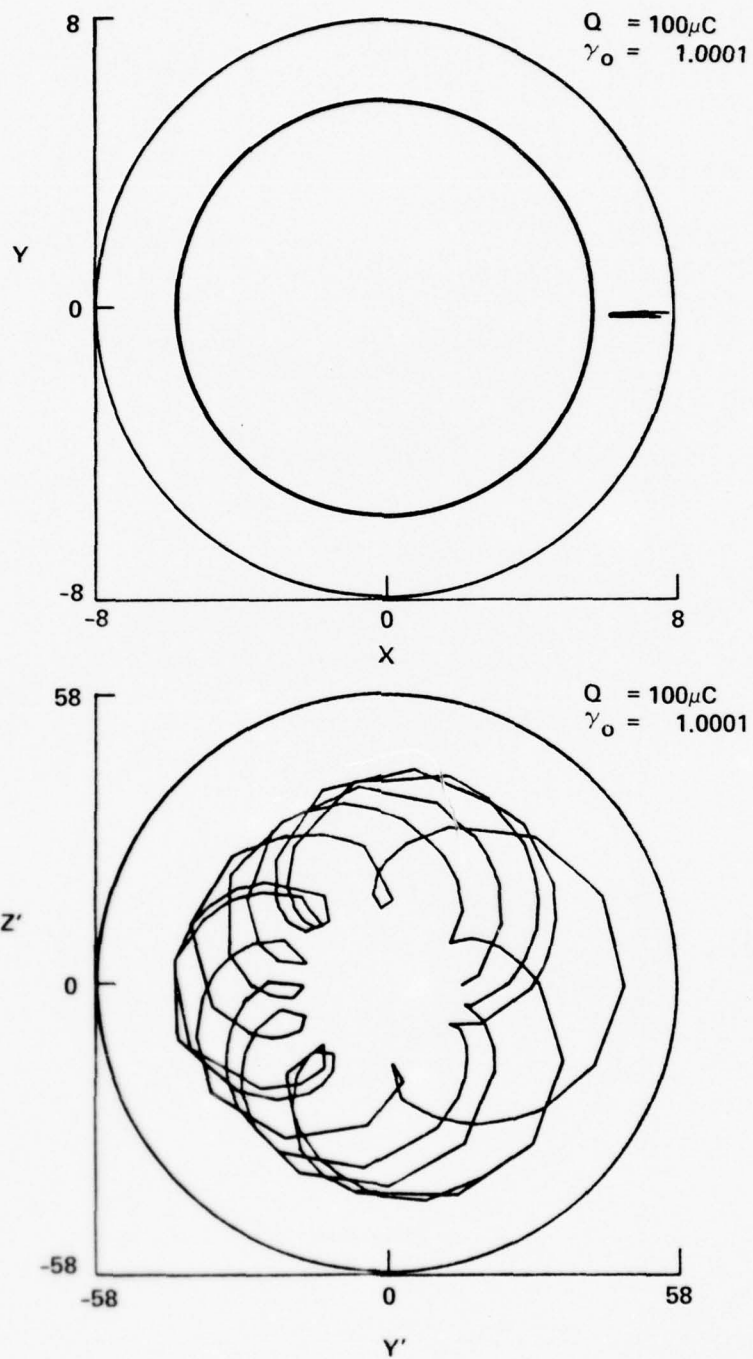
Figure 7-10. Azimuthal Drift $Q = 100 \, \mu c$, $\gamma_o = 1.0001$.

29
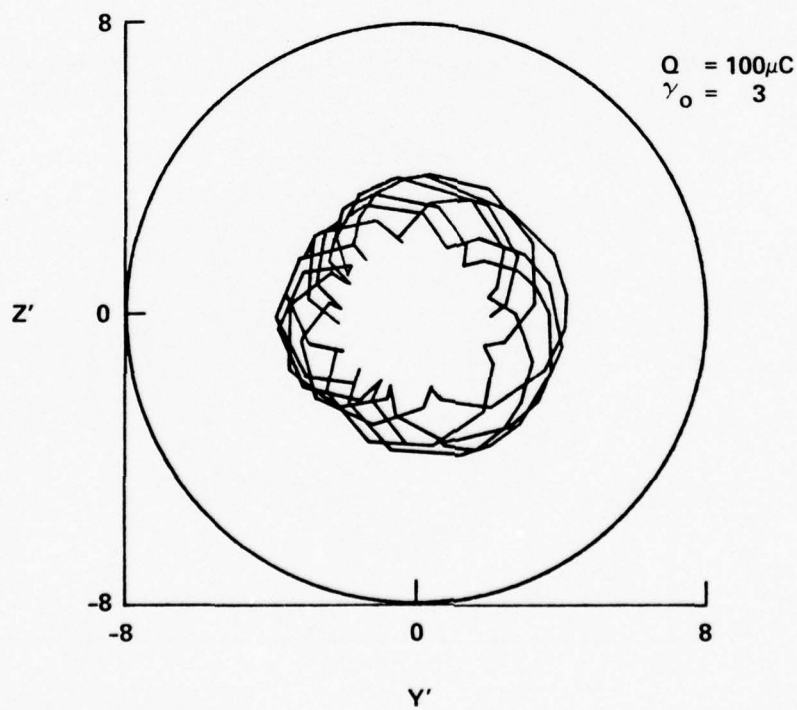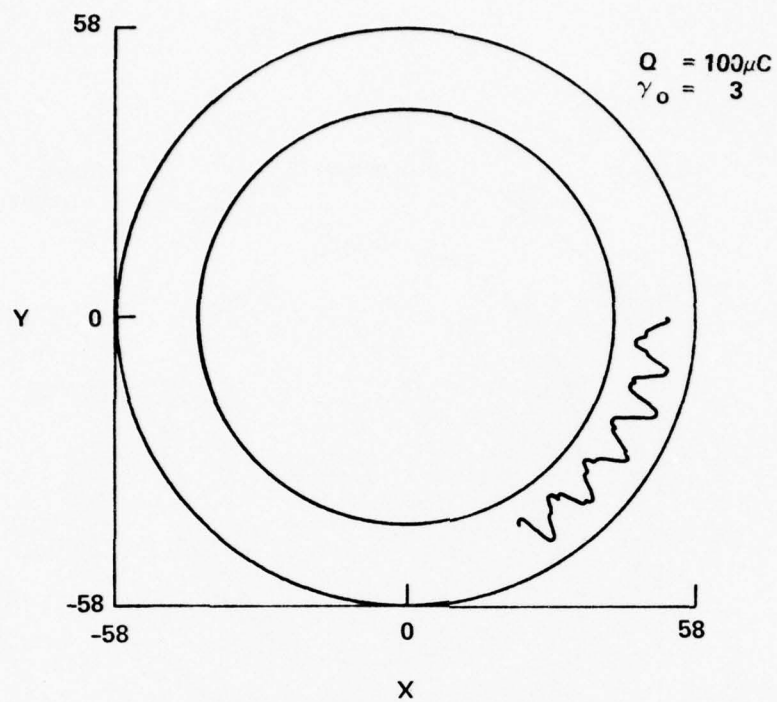
Figure 7-11. Azimuthal Drift Q = 100 μc, γ_o = 3.

$\gamma_o = 3$ for the electron cloud. The test electron still begins at rest. The orbit now is smaller because the radial force is decreased by the presence of B_θ. The test electron drifts in the toroidal direction due to $\Delta B \times \hat{e}_\theta B_\theta$.

Figures 7-12 and 7-13 show the results of test runs in which the torus contained $100\ \mu C$ of charge, and the test electron was launched in the toroidal direction with relativistic energy. In Figure 7-12, the test electron was launched with $\gamma = 2$, and the curvature drift overpowered the azimuthal drift, causing the test electron to hit the wall. In Figure 7-13, we reduced the test-particle energy to $\gamma = 1.5$, and obtained a stable, confined orbit. We note that the center of the orbit in the x-z plane does not coincide with the center of the conducting wall; but is shifted toward the inner wall of the torus. The trajectory can be centered in the torus through the application of a vertical field, B_z.

The major problem encountered in relativistic electron injection from the torus wall is that the electron trajectory lies close to the wall and is not concentric with the walls. The inevitable result, therefore, is that unaided electrons will hit the wall. One exception, which is not experimentally feasible, is to launch the electron from the inner wall of the torus. Since the trajectories are displaced toward this wall, an unaided electron will be trapped within the torus. This situation is illustrated in Figure 7-14, which shows the trajectory of an electron having $\gamma = 1.2$ launched from the inner wall with $p_\theta = p_\omega$ and $p_r = 0$. The electron remains in the torus during the entire 10 ns duration of the computer run. When the electron is launched in an identical manner from the lower wall of the torus, it hits the upper wall as shown in Figure 7-15.

To overcome these difficulties, we use external magnetic fields to assist in electron injection. The two basic types of external field under consideration are the vertical magnetic field, B_z, and the diverter field. The diverter field, a simple current loop near the injection point, serves to locally distort the magnetic field lines near the injector so that electrons can be introduced along field lines which run to the interior of the torus. In this way, the electron trajectory is moved away from the wall and the centering of the orbit becomes less critical. The successful operation

31
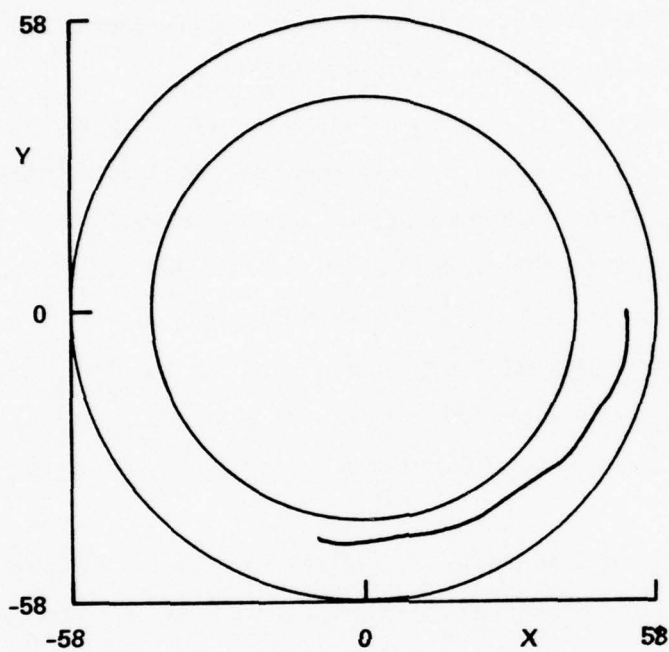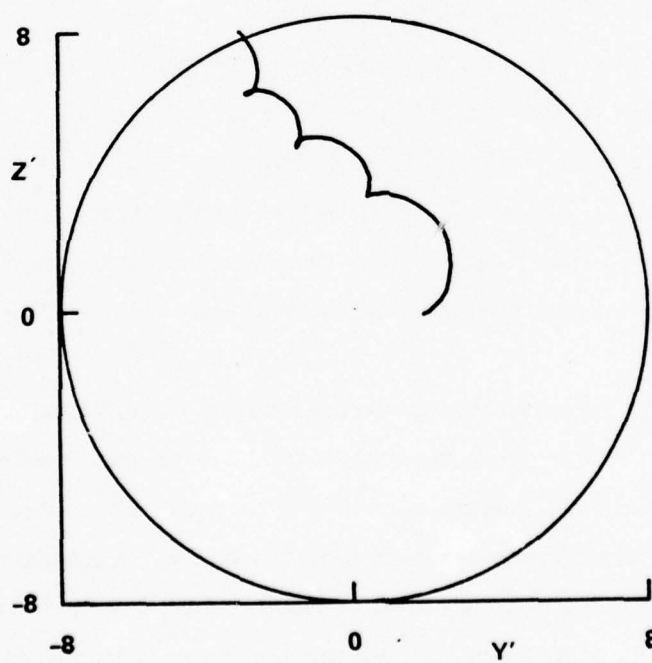
Figure 7-12. Particle Orbit $Q = 100 \mu c$, $\gamma = \gamma_o = 2$.
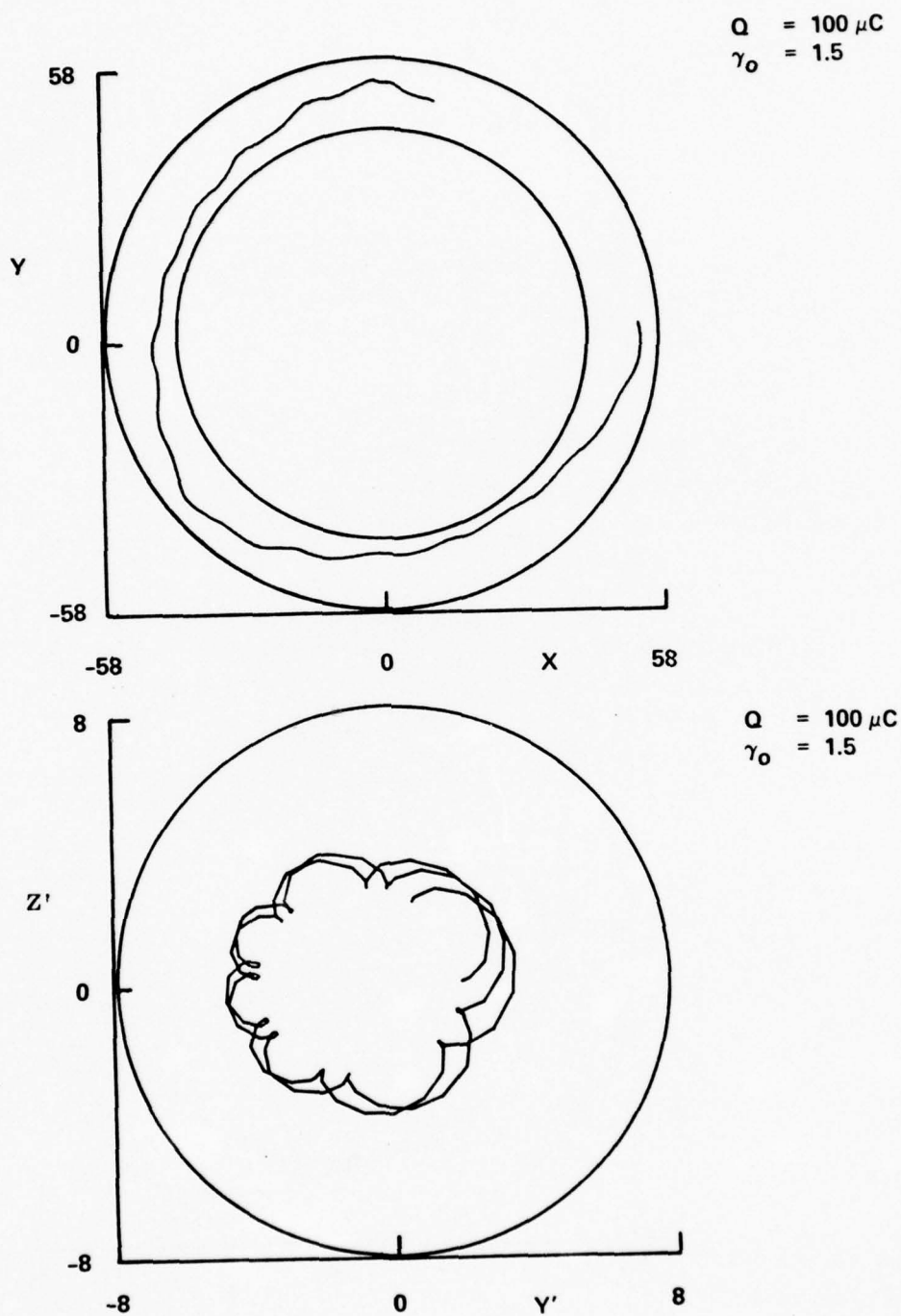
Figure 7-13. Particle Orbit $Q = 100\ \mu c$, $\gamma = \gamma_o = 1.5$.

33
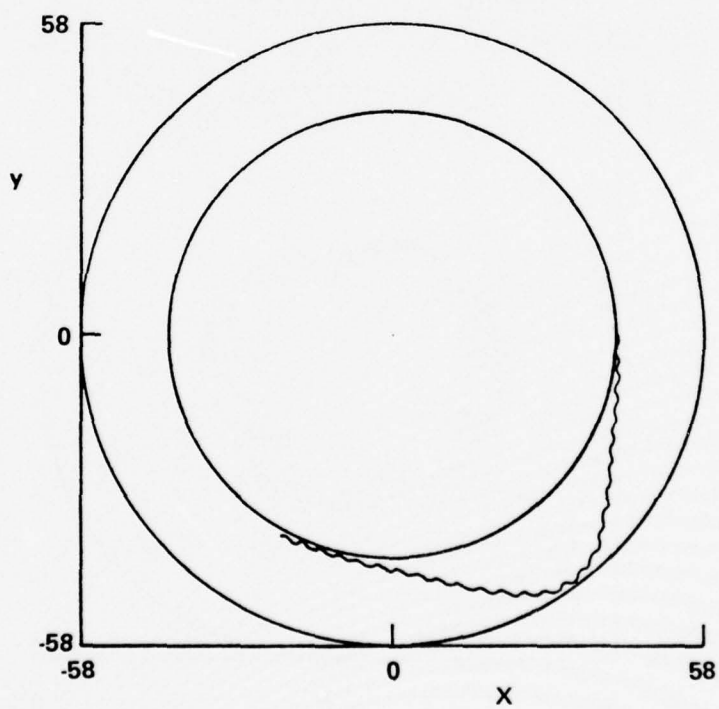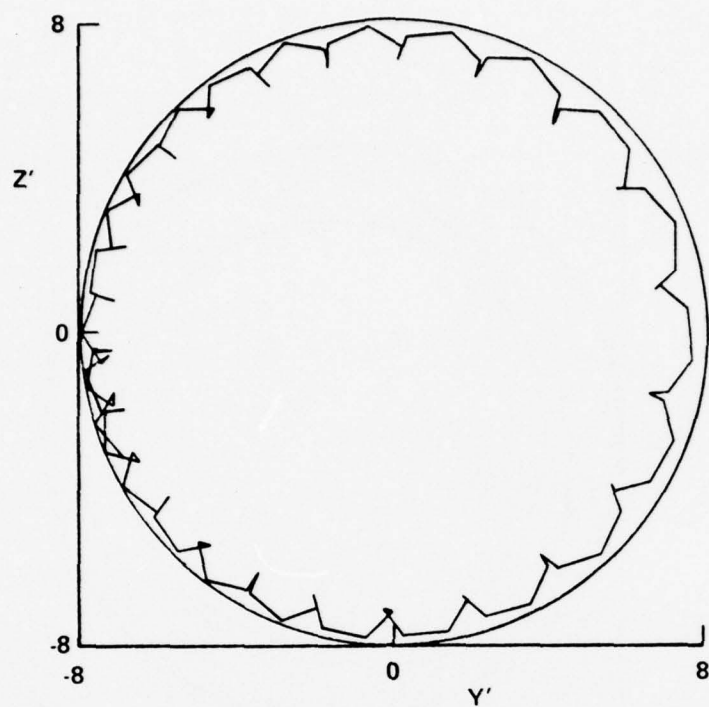
Figure 7-14. Un-Aided Electron Injection From Inner Wall With $\gamma = 1.2$, $P_r = 0$, $P_\theta = P_\varphi$.
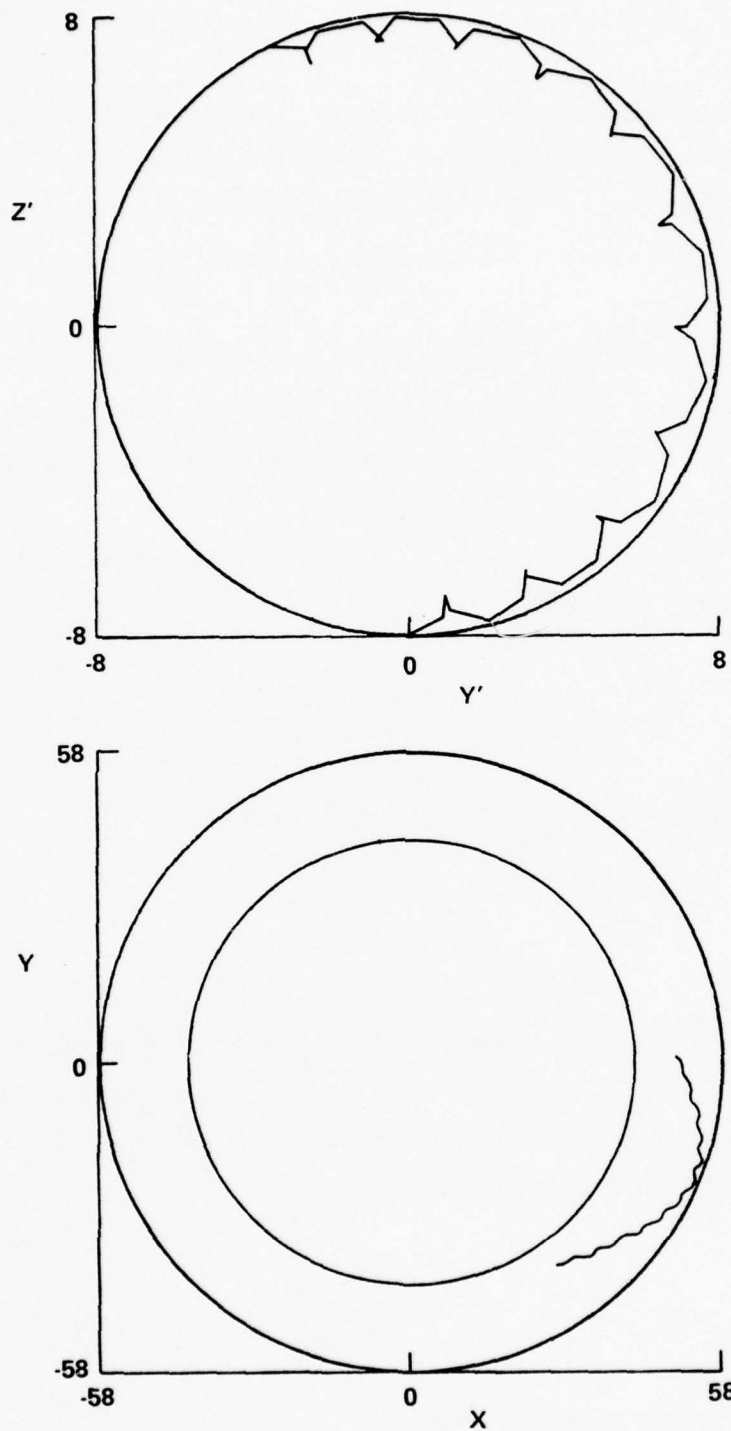
Figure 7-15. Un-Aided Electron Injection From Lower Wall With $\gamma = 1.2$, $P_r = 0$, $P_\theta = P_\varphi$.

of the diverter depends on the local magnetic perturbation being large enough to allow electron injection, yet small enough that the electron is unlikely to leave the torus through the diverter after only a few transits of the torus. The injected electrons must remain within the torus for $\geqq 1$ μs, which is the expected duration of the high-energy electron pulse.

The vertical magnetic field acts to displace the electron orbits toward the outer wall of the torus, thereby allowing us to make the orbit concentric with the torus wall. Through the use of this field we can relax the diverter field, making successful containment of the injected electrons easier.

The vertical magnetic field B_z acts by producing a force on the electron in the direction of the major radius,

$$F_R = \frac{e}{c} \, v_\circ B_z,$$

which, when coupled to $B_\circ$, produces a vertical drift;

$$v_z = v_\circ \frac{B_z}{B_\circ} \, .$$

This drift competes with the vertical drift due to grad B and centrifugal forces. To displace the beam toward the outer wall of the torus, the vertical field must produce a v_z drift which tends to cancel the toroidal geometry drifts. Neglecting $v_\perp/v_\circ$ relative to unity, the curvature drifts are given by

$$v_{zc} = \frac{\beta^2 \gamma m c^3}{eRB_\circ} \, .$$

For these two drifts to cancel, we require

$$B_z = - \frac{\gamma \beta m c^2}{eR} \simeq - 34 \, \gamma \beta \ \text{Gauss}$$

36

for R = 50 cm. Note that a negative (downward) vertical field is required to center the orbit when $v_{\circlearrowleft}$ is positive. This analysis indicates that the vertical magnetic field can be employed to remove the need for a rotational transform by canceling the vertical drifts due to toroidal geometry (curvature and grad B).

In Figure 7-7 we displayed the upward vertical drift of a test electron with $\gamma = 3$. From the above discussion, it appears that $B_z = -96$ Gauss should just cancel this drift. Figure 7-16 shows that the expected result is realized when we rerun this example with the inclusion of vertical field.

In Figure 7-12, we saw that $Q = 100 \, \mu C$ did not provide sufficient rotational transform to contain a test electron with $\gamma = 2$. By adding a vertical magnetic field, $B_z = -59$ Gauss, however, we can eliminate the need for the rotational transform and the test electron is contained as shown in Figure 7-17. Note also that the contained orbit is concentric with the torus wall. The inward shift due to the superposition of vertical and poloidal drifts has been eliminated by the inclusion of the vertical magnetic field.

Studies are underway to inject relativistic electrons from near the torus wall. Using vertical field to center the trajectory, the results shown in Figure 7-18 were obtained. The electron was injected with $\gamma = 1.5$, $p_r = 0$, $p_\theta = p_{\circlearrowleft}$ from an internal injector 1 cm from the torus wall. Multi-turn confinement of the electron is evident in the figure, which shows only the first 250 ns of the trajectory. The injector was treated as an obstacle in the code and enclosed a 1 cm x 1 cm x 1 cm volume near the torus wall. In this particular example, the test electron struck the injector after 908 ns. Smaller injectors, with electrons emitted close to the edge of the injector should be investigated in an effort to determine if such an internal injector can form the basis of a high-energy electron source.

7.1.3 Self-Consistent Relativistic Equilibria

There are several approximate calculations for self-consistent relativistic equilibria. The simplest approach is to assume that the electron motion in the "beam frame" is non-relativistic and to then transform the resulting equilibrium to the
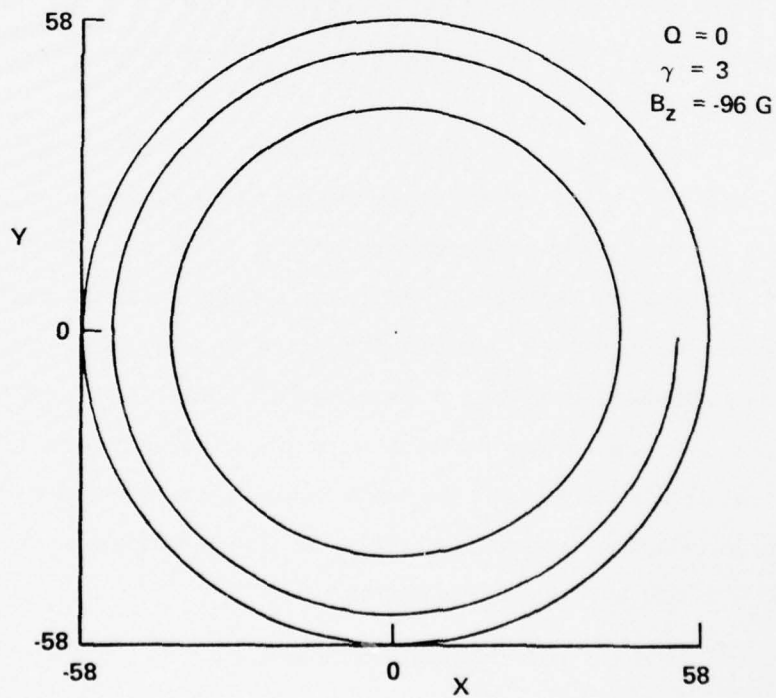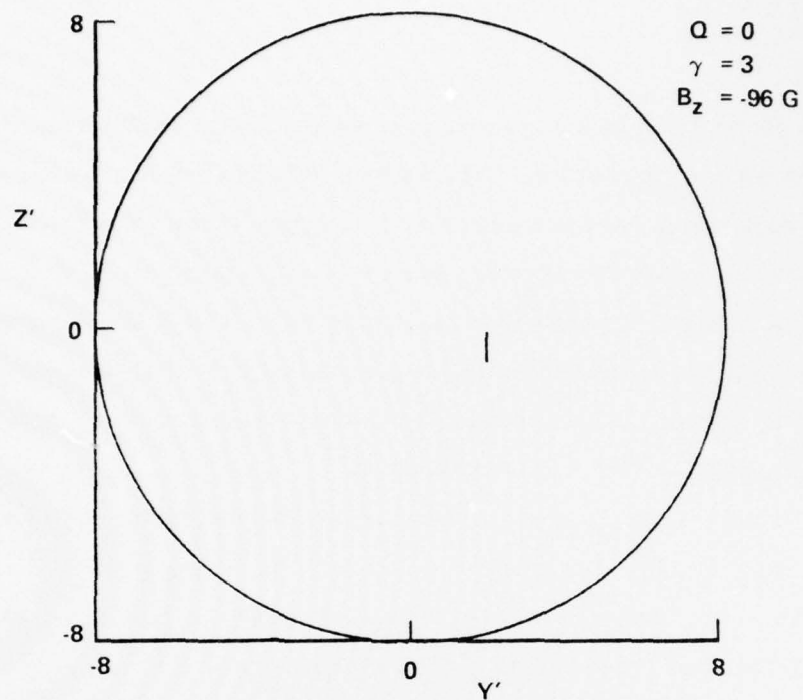
Figure 7-16. Cancellation of Vertical Drift by Vertical Magnetic Field ($Q = 0$, $\gamma = 3$, $B_z = -96G$).

38
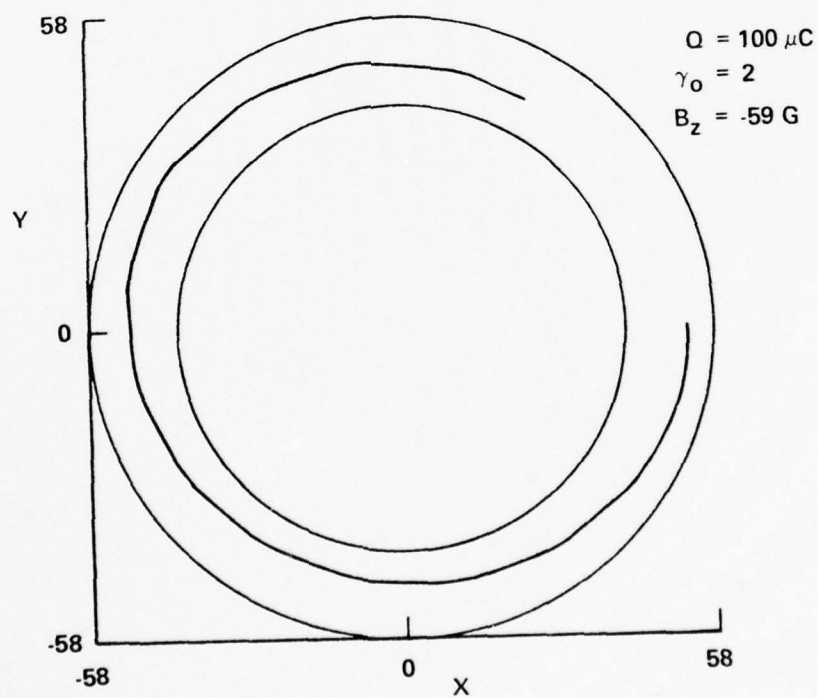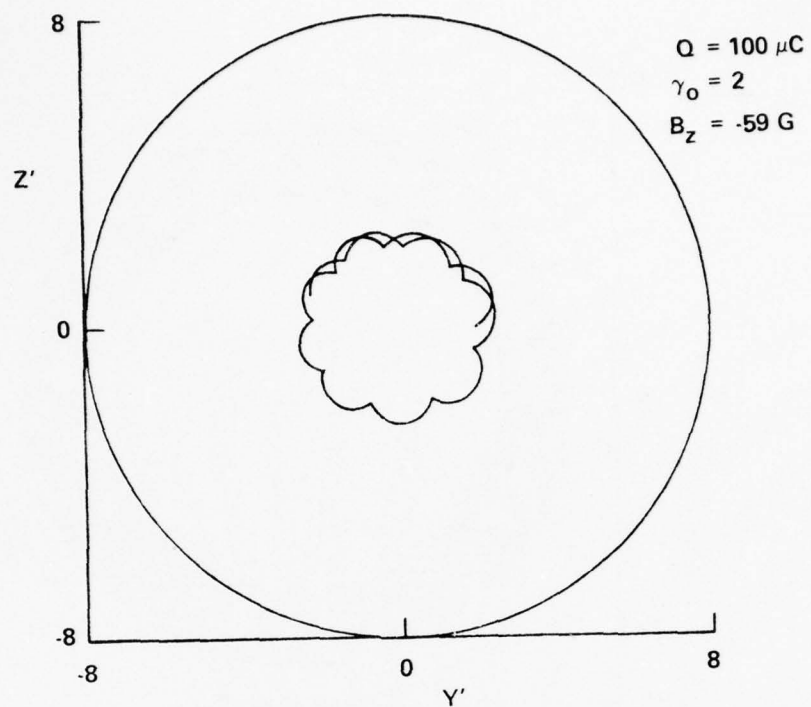
Figure 7-17. Centering and Containment of Electron Trajectory With Vertical Field
$(Q = 100 \, \mu C, \, \gamma = 2, \, B_z = -59G)$.
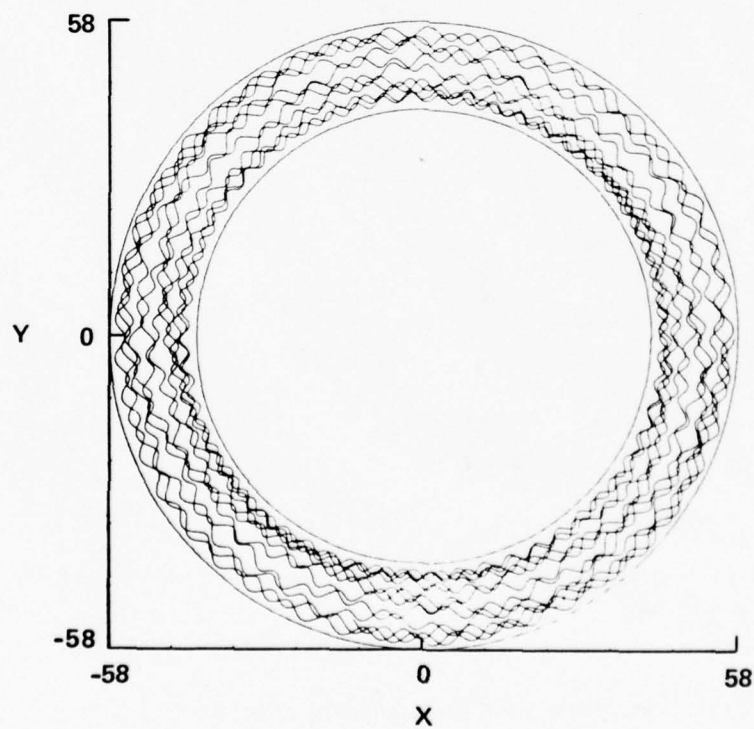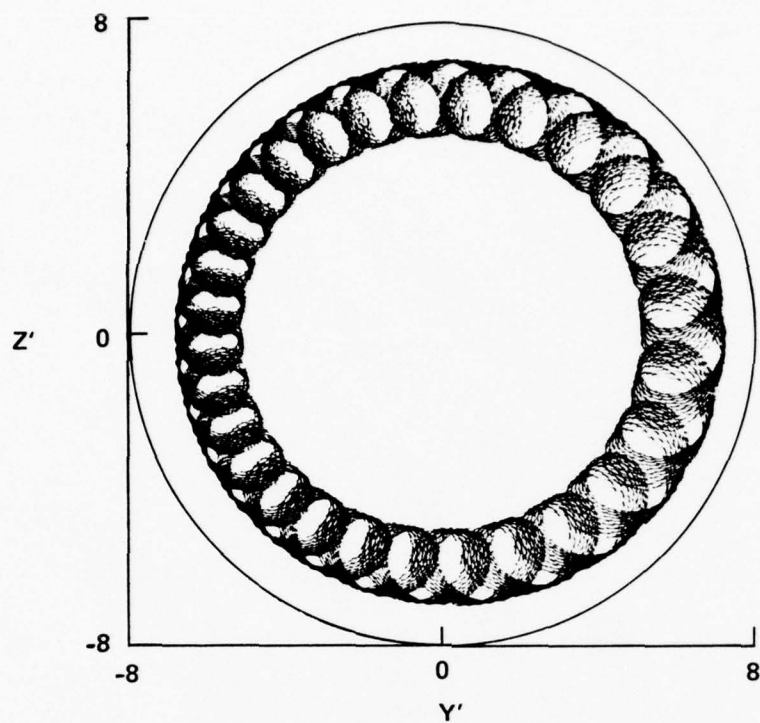
Figure 7-18. Multi-Turn Injection of a High-Energy Electron.

40

laboratory frame via the Lorentz transformation. The result so obtained will be shown to be equivalent to working in the laboratory frame using the "two-mass" approximation, to be described below, in an expansion to second order in the small parameter, q, where

$$q^2 \equiv \frac{1}{2\gamma_o^2} \left(\frac{\omega_p}{\Omega_o} \right)^2 \ll 1.$$

This expansion will be shown to be valid when $\nu / \gamma_o^3 \ll 1/4$.

Starting with the beam frame (denoted by prime), and assuming the motion to be non-relativistic, we obtain the single-particle constants of motion,

$$H' = \frac{1}{2} m v'^2 - e \Phi' (r')$$

$$P'_\theta = r' m v'_\theta - \frac{e}{c} r' A'_\theta (r')$$

$$P'_z = m v'_z$$

where all quantities are assumed to depend on the radial coordinate only. Any function of these constants will satisfy the stationary Vlasov equation, and we use

$$F (r', \underline{v}') = \frac{m}{2\pi} n'_o \delta \left[H' - \omega' P'_\theta - \xi' \right] \delta (v'_z)$$

$$= \frac{m}{2\pi} n'_o \delta \left[\frac{1}{2} m v'^2_\perp - g' (r') \right] \delta (v'_z)$$

where

$$v'^2_\perp \equiv v'^2_r + (v'_\theta - \omega' r')^2$$

and

$$g' (r') \equiv e \Phi' - \frac{e \omega' r'}{c} A'_\theta + \frac{1}{2} m (\omega' r')^2 + \xi' \quad .$$

41

By computing the moments of $F(r, \underline{v})$, we see that this equilibrium corresponds to a uniform density rigid-rotor with a finite beam radius, a. The non-vanishing moments are

$$n'(r') = \begin{cases} n'_o & r' \leq a' \\ \\ 0 & r > a' \end{cases}$$

$$n'(r')\langle v'_\theta \rangle = \begin{cases} n'_o \, \omega' r' & r' \leq a' \\ \\ 0 & r' > a' \end{cases}$$

$$n'(r') \langle v'^2_r \rangle = n'(r') \langle (v'_\theta - \omega' r')^2 \rangle = \begin{cases} \dfrac{n'_o}{m} \, g'(r') & r' \leq a' \\ \\ 0 & r' > a' \end{cases}$$

where the beam radius is given by

$$g'(a') = 0$$

together with the conditions for self-consistency,

$$g'(r' > a') < 0$$

$$g'(r' < a') > 0$$

which must be verified a posteriori.

We may also define a transverse "thermal" velocity

$$\langle v'^2_\perp \rangle = \left[\langle v'^2_r \rangle + \langle v'^2_\theta \rangle \right]_{r' = 0} = \frac{2}{m} \, g'(0) \ .$$

42

The self-consistent fields are obtained from Maxwell's equations

$$\frac{1}{r'} \frac{d}{dr'} r' \frac{d\Phi'}{dr'} = \begin{cases} 4\pi \, en'_o & r' \le a' \\ \\ 0 & r' > a' \end{cases}$$

$$\frac{d}{dr'} \frac{1}{r'} \frac{d}{dr'} r' A'_\theta = \begin{cases} 4\pi \, en'_o \, \omega' \, r'/c & r' \le a' \\ \\ 0 & r' > a' \, . \end{cases}$$

Assuming the presence of a conducting shell of radius b', with Φ' (b') = 0, we obtain

$$\Phi' (r') = \begin{cases} -N' \, e \left[1 + 2\ell n \, \frac{b'}{a'} - \left(\frac{r'}{a'}\right)^2 \right] & r' \le a' \\ \\ 2 N' \, e\ell n \, \frac{r'}{b'} & a' \le r' \le b' \end{cases}$$

$$E'_r(r') = -\frac{2N'e}{a'} \begin{cases} r'/a' & r' \le a' \\ \\ a'/r' & a' \le r' \le b' \end{cases}$$

$$A'_\theta (r') = \begin{cases} \frac{1}{2} B'_o r' - N'e \, \frac{\omega' r'}{c} \left[1 - \frac{1}{2} \left(\frac{r'}{a'}\right)^2 \right] & r' \le a' \\ \\ \frac{1}{2} B'_o r' - N'e \left(\frac{\omega' a'}{c}\right) \frac{a'}{r'} & a' \le r' \le b' \end{cases}$$

$$B'_z (r') = \begin{cases} B'_o - \frac{2N'e}{a'} \left(\frac{\omega' a'}{c}\right) \left[1 - \left(\frac{r'}{a'}\right)^2 \right] & r' \le a' \\ \\ B'_o & a' \le r' \le b' \, . \end{cases}$$

43

Returning now to $g'(r')$, we must verify the conditions for self-consistency and derive the relationship between the beam radius and ω'. The equation $g'(a') = 0$ implies

$$\xi' = 2N'e^2 \ell n \frac{b}{a} + \frac{1}{2} eB'_o a' \left(\frac{\omega' a'}{c} \right) - \frac{1}{2} N'e^2 \left(\frac{\omega' a'}{c} \right)^2$$
$$- \frac{1}{2} mc^2 \left(\frac{\omega' a'}{c} \right)^2 \quad .$$

Using this expression, we obtain

$$g'(r'<a') = \left\{ \frac{eB'_o a'}{2} \left(\frac{\omega' a'}{c} \right) - N'e^2 - \frac{1}{2} N'e^2 \left(\frac{\omega' a'}{c} \right)^2 \left[1 - \left(\frac{r'}{a'} \right)^2 \right] \right.$$
$$\left. - \frac{1}{2} mc^2 \left(\frac{\omega' a'}{c} \right)^2 \right\} \left[1 - \left(\frac{r'}{a'} \right)^2 \right]$$

which must satisfy $g'(r' < a') > 0$, or

$$\frac{\Omega'_o}{\omega'} > \frac{1}{2} \quad \frac{\omega'_p}{\omega'} \left[1 + \frac{1}{2} \left(\frac{\omega' a'}{c} \right)^2 \right] + \frac{\omega'}{\omega'_p} \quad .$$

Similarly, for $r' > a'$ we obtain

$$g'(r'>a') = 2N'e^2 \ell n \frac{r'}{a'} + \left\{ \frac{1}{2} mc^2 \left(\frac{\omega' a'}{c} \right)^2 - \frac{1}{2} eB'_o a' \left(\frac{\omega' a'}{c} \right) \right\} \left[\left(\frac{r'}{a'} \right)^2 - 1 \right]$$

which must satisfy $g'(r' > a') < 0$, or

$$\frac{\Omega'_o}{\omega'_p} > \frac{1}{2} \frac{\omega'_p}{\omega'} + \frac{\omega'}{\omega'_p} \quad .$$

Finally, using

$$\frac{1}{2} m \langle v_{\perp}'^{2} \rangle = g'(0) = -N'e^{2} \left[1 + 2 \ln \frac{b'}{a'} \right] + \xi'$$

we obtain a quadratic equation for ω',

$$\left(\frac{\omega' a'}{c} \right)^{2} \left[1 + \frac{1}{4} \left(\frac{\omega_{p}' a'}{c} \right)^{2} \right] - \left(\frac{\Omega' a'}{c} \right) \left(\frac{\omega' a'}{c} \right) + \left[\frac{1}{2} \left(\frac{\omega_{p}' a'}{c} \right)^{2} + \frac{\langle v_{\perp}'^{2} \rangle}{c^{2}} \right] = 0$$

which has two solutions, $\omega_{\pm}'$, given by

$$\omega_{\pm}' = \frac{1}{2 \left[1 + \frac{1}{4} \left(\frac{\omega_{p}' a'}{c} \right)^{2} \right]} \left\{ \frac{\Omega_{o}' a'}{c} \right.$$

$$\left. \pm \sqrt{ \left(\frac{\Omega_{o}' a'}{c} \right)^{2} - 4 \left[1 + \frac{1}{4} \left(\frac{\omega_{p}' a'}{c} \right)^{2} \right] \left[\frac{1}{2} \left(\frac{\omega_{p}' a'}{c} \right)^{2} + \frac{\langle v_{\perp}'^{2} \rangle}{c^{2}} \right] } \right\} .$$

The requirement that $\omega_{\pm}'$ be real introduces an additional condition,

$$\left(\frac{\Omega_{o}'}{\omega_{p}'} \right)^{2} \geq 2 \left[1 + \frac{1}{4} \left(\frac{\omega_{p}' a'}{c} \right)^{2} \right] \left[1 + 2 \frac{\langle v_{\perp}'^{2} \rangle}{c^{2}} \left(\frac{c}{\omega_{p}' a'} \right)^{2} \right] .$$

If this equation is satisfied and $\langle v_{\perp}'^{2} \rangle > 0$, then a self-consistent equilibrium has been found. We can prove this statement by rewriting the quadratic equation for ω', as

$$\frac{\Omega_{o}'}{\omega_{p}'} = \frac{\omega'}{\omega_{p}'} \left[1 + \frac{1}{4} \left(\frac{\omega_{p}' a'}{c} \right)^{2} \right] + \frac{1}{2} \frac{\omega_{p}'}{\omega'} \left[1 + 2 \frac{\langle v_{\perp}'^{2} \rangle}{\omega_{p}'^{2} a'^{2}} \right]$$

which satisfies the conditions for equilibrium provided $\langle v_{\perp}'^{2} \rangle > 0$.

45

To transform to the laboratory frame, we use a Lorentz transformation

$$r = r', \quad a = a', \quad b = b'$$

$$\omega = \omega'/\gamma_o$$

$$v_\perp = v'_\perp/\gamma_o$$

$$\Phi' = \gamma_o (\Phi - \beta_o A_z)$$

$$A'_z = 0 = \gamma_o (A_z - \beta_o \Phi) \text{ or } A_z = \beta_o \Phi, \quad B_\theta = \beta_o E_r$$

$$A'_\theta = A_\theta \text{ or } B'_o = B_o, \quad B'_z = B_z .$$

The plasma and cyclotron frequencies transform to

$$\Omega_p^2 = \frac{\omega_p'^2}{\gamma_o^2} = \frac{4\pi n_o' e^2}{\gamma_o^2 m} = \frac{4\pi n_o e^2}{\gamma_o^3 m} \equiv \frac{\omega_p^2}{\gamma_o^2}$$

$$\Omega_o = \frac{\Omega_o'}{\gamma_o} = \frac{eB_o}{\gamma_o mc}$$

with $\omega_p^2 = 4\pi n_o e^2/\gamma_o m$. The self-consistent rigid-rotor frequency is

$$\omega_\pm = \frac{\Omega_o}{2\left[1 + \frac{1}{4}\left(\frac{\omega_p a}{c}\right)^2\right]} \left\{ 1 \pm \sqrt{1 - \frac{2}{\gamma_o^2}\left(\frac{\omega_p}{\Omega_o}\right)^2 \left[1 + \frac{1}{4}\left(\frac{\omega_p a}{c}\right)^2\right]\left[1 + 2\gamma_o^2 \frac{\langle v_\perp^2\rangle}{\omega_p^2 a^2}\right]} \right\}$$

46

and the condition for equilibrium is

$$q^2 \equiv \frac{1}{2\gamma_o^2} \left(\frac{\omega_p}{\Omega_o}\right)^2 \leq \left\{ 4\left[1 + \frac{1}{4}\left(\frac{\omega_p a}{c}\right)^2\right]\left[1 + 2\gamma_o^2 \frac{\langle v_\perp^2\rangle}{\omega_p^2 a^2}\right]\right\}^{-1}$$

which we plot in Figure 7-19. From the figure we see that $q^2 \ll 1$ is required when $\omega_p a/c$ is large. Since $\nu/\gamma_o = .25\,(\omega_p a/c)^2$ is the ratio of beam field energy to particle kinetic energy, we see that q^2 is a small parameter for equilibria which store energy mainly in the beam self fields.

This equilibrium may also be computed in the laboratory frame, using the "two-mass" approximation, where the axial velocity is written as $v_z = V_o + (v_z - V_o)$ with the assumptions, $V_o \gg v_\perp$, $|v_z - V_o|$ and V_o assumed to be constant. In this approximation we may write

$$\frac{d}{dt}(\gamma m \underline{v}) = \gamma m \underline{\dot{v}}_\perp + \gamma^3 m \underline{\dot{v}}_\parallel$$

$$\simeq \gamma_o m \underline{\dot{v}}_\perp + \gamma_o^3 m \dot{v}_z e_z$$

$$\underline{\dot{v}}_\parallel = \underline{v}(v \cdot \underline{\dot{v}})/v^2, \quad \underline{\dot{v}}_\perp = \underline{\dot{v}} - \underline{\dot{v}}_\parallel,$$

where $\gamma_o = (1 - \beta_o^2)^{-1/2}$ and $\beta_o = V_o/c$. The single-particle equations of motion are

$$\gamma_o m\left[\frac{dv_r}{dt} - \frac{v_\theta^2}{r}\right] = -e\left[E_r + \frac{1}{c}\left(v_\theta B_z - v_z B_\theta\right)\right]$$

$$\gamma_o m\left[\frac{dv_\theta}{dt} + \frac{v_r v_\theta}{r}\right] = \frac{e}{c} v_r B_z$$

$$\gamma_o^3 m \frac{dv_z}{dt} = -\frac{e}{c} v_r B_\theta = \frac{e}{c}\frac{dA_z}{dt} \simeq 0 \ .$$

47
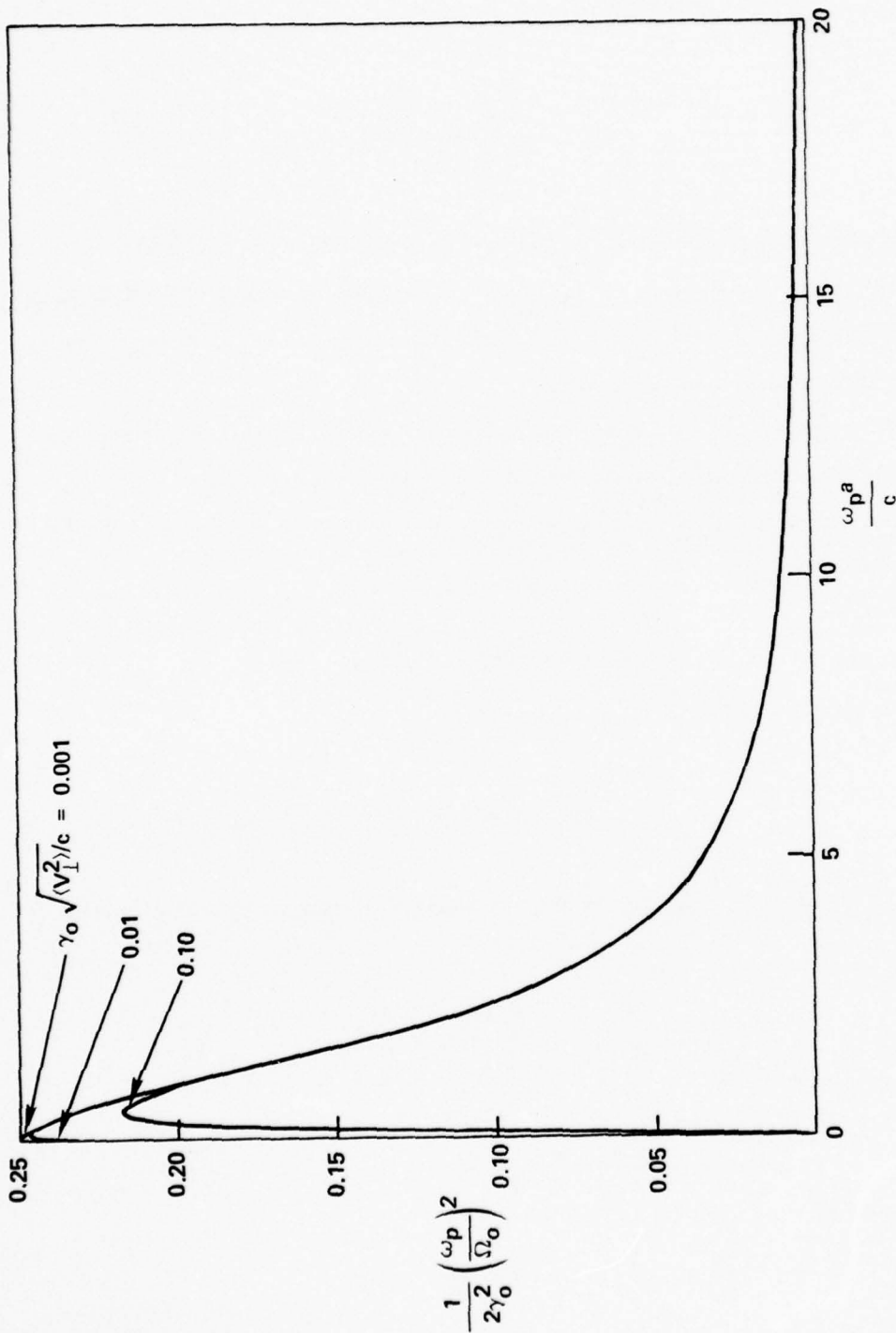
Figure 7-19. q^2 Versus $\omega_p a/c$ for the Rostoker–Hieronymus Two-Mass Equilibrium.

48

These equations were derived from an expansion to second order in the small parameter, q, keeping terms to order q^2, by Rostoker and Hieronymus.

The claim, $dA_z/dt \simeq 0$, implies the constancy of v_z. In fact, the canonical axial momentum,

$$P_z = \gamma_o^3 m v_z - \frac{e}{c} A_z$$

is the exact constant of the motion. To have $dA_z/dt \simeq 0$ to order q^2, we must establish that the change in v_z during the particle orbit is of higher order. The radial variation in the trajectory of a single electron which executes an azimuthal drift at velocity $v_\theta = \omega r$ is

$$\Delta r = \frac{2v_\theta}{\Omega_o} = \frac{2\omega r}{\Omega_o}$$

and using $\omega \simeq q^2 \Omega_o$ (neglecting $\langle v_\perp^2 \rangle / c^2$), we have

$$\frac{\Delta r}{r} \simeq 2q^2 .$$

The change is $A_z(r)$ over Δr is

$$\Delta A_z \simeq \frac{dA_z}{dr} \Delta r = \left(\frac{2Ne\beta_o r}{a^2} \right) \left(2q^2 r \right) .$$

From the constancy of P_z, we see that the change in v_z over the electron trajectory is

$$\Delta v_z = \frac{e}{\gamma_o^3 mc} \Delta A_z ,$$

49

or

$$\frac{\Delta v_z}{\beta_o c} = \frac{q^2}{\gamma_o^2} \left(\frac{r}{a}\right)^2 \left(\frac{\omega_p a}{c}\right)^2 = q^2 \left(\frac{r}{a}\right)^2 \frac{4\nu}{\gamma_o^3} \ .$$

To satisfy

$$\frac{\Delta v_z}{\beta_o c} \ll q^2 \ .$$

for second-order constancy in v_z, we must require

$$\frac{\nu}{\gamma_o^3} \ll \frac{1}{4}$$

With this assumption, the single-particle constants of motion are

$$H_\perp = \frac{1}{2} \gamma_o m \left(v_r^2 + v_\theta^2\right) - e \left(\Phi - \beta_o A_z\right)$$

$$P_\theta = \gamma_o mrv_\theta - \frac{e}{c} r A_\theta$$

$$v_z \simeq V_o$$

correct to order q^2. The distribution function

$$F(r, \underline{v}) = \frac{\gamma_o mn_o}{2\pi} \delta \left[H_\perp - \omega P_\theta - \xi_o\right] \delta \left[v_z - V_o\right]$$

yields the same equilibrium as was previously obtained by assuming non-relativistic motion in the beam frame.

50

If we attempt to use the two mass approximation with the full constants of motion,

$$H = \frac{1}{2} \gamma_o m \left(v_r^2 + v_\theta^2 \right) + \frac{1}{2} \gamma_o^3 m v_z^2 - e\,\Phi(r)$$

$$P_\theta = \gamma_o m r v_\theta - \frac{e}{c} r A_\theta(r)$$

$$P_z = \gamma_o^3 m v_z - \frac{e}{c} A_z(r)$$

in the distribution function,

$$F(r, \underline{v}) = \frac{\gamma_o^4 m^2}{2\pi} \, n_o \, \delta \left[H - \omega\, P_\theta - \xi_o \right] \delta \left[P_z - \gamma_o^3 m V_o \right] \,,$$

the macroscopic velocity in the axial direction is found to be

$$\langle v_z \rangle = V_o \, I_o \left(\frac{\omega_p r}{\gamma_o c} \right)$$

for $r \le a$, where I_o is the modified Bessel function of zero order. To satisfy the requirements of the two-mass approximation, $V_o \gg \left| v_z - V_o \right|$, we must have

$$\frac{\omega_p a}{\gamma_o c} \ll 1$$

or again

$$\frac{\nu}{\gamma_o^3} \ll \frac{1}{4} \,.$$

With this inequality, we may expand the Bessel function and we recover the previous equilibrium. The two-mass approximation, therefore, corresponds to assuming non-relativistic motion in the beam frame and appears valid when $\nu/\gamma_o^3 \ll 1/4$. A more

51

exact condition for the validity of the two-mass approximation will emerge below, where we discuss fully-relativistic self-consistent rigid-rotor equilibria.

In terms of the fully-relativistic single-particle constants of motion in the beam frame (prime),

$$H' = mc^2 \sqrt{1 + (p'/mc)^2} - e\Phi'$$

$$P'_\theta = r'(p'_\theta - \frac{e}{c} A'_\theta)$$

$$P'_z = p'_z$$

where $p'_z = \gamma' mv'_z$ and $p'_\theta = \gamma' mv'_\theta = (p'_y x' - p'_x y')/r' = p'_\perp \sin(\phi - \theta)$, we consider an equilibrium distribution function of the form

$$F(\underline{r}', \underline{p}') = K'\delta\left[H' - \omega' P'_\theta - \xi'_o\right]\delta(p'_z) \quad .$$

Introducing the variable $y = \sqrt{1 + (p'_\perp/mc)^2}$, the density and macroscopic velocity may be evaluated as follows

$$n'(r') = \int F(\underline{r}', \underline{p}')\,d\underline{p}'$$

$$= K'm \int_1^\infty y\,dy \int_0^{2\pi} d\phi\,\delta\left[y - \frac{\omega' r'}{c} \sqrt{y^2 - 1} \sin(\phi - \theta) - g'(r')\right]$$

$$n'(r')\langle v'_\theta \rangle = K'm \int_1^\infty y\,dy \int_0^{2\pi} d\phi\, \frac{c\sqrt{y^2 - 1}}{y} \sin(\phi - \theta)$$

$$\delta\left[y - \frac{\omega' r'}{c} \sqrt{y^2 - 1} \sin(\phi - \theta) - g'(r')\right]$$

52

where

$$g'(r') = \frac{1}{mc^2} \left[\xi'_o - \frac{e\,\omega'r'}{c} A'_\theta + e\,\Phi' \right] .$$

To carry out the indicated integrations, the δ-function may be expressed as

$$\frac{1}{\frac{\omega'r'}{c} \sqrt{y^2 - 1}} \quad \frac{2}{\left| \cos \omega_o \right|} \quad \delta(\omega - \omega_o)$$

where

$$\cos \omega_o = \frac{\left\{ \left(\frac{\omega'r'}{c}\right)^2 (y^2 - 1) - \left[y - g'(r') \right]^2 \right\}^{1/2}}{\left(\frac{\omega'r'}{2}\right)^2 \sqrt{y^2 - 1}}$$

with the requirement

$$\left(\frac{\omega'r'}{c}\right)^2 \left(y^2 - 1\right) \geq \left[y - g'(r') \right]^2 .$$

To satisfy this equation, y must lie in the range, $y_- \leq y \leq y_+$, where

$$y_\pm = \frac{1}{1 - \left(\frac{\omega'r'}{c}\right)^2} \left\{ g'(r') \pm \frac{\omega'r'}{c} \sqrt{g'^2(r') - \left[1 - \left(\omega'r'/c\right)^2 \right]} \right\}$$

as shown in Figure 7-20. The two intersections y_-, y_+ coalesce to one when $g'(r') = \sqrt{1 - (\omega'r'/c)^2}$ in which case $y_\pm = \sqrt{1 - (\omega'r'/c)^2}$ > 1. The radius of the beam is defined by

$$g'(a') = \sqrt{1 - (\omega'a'/c)^2}$$

53
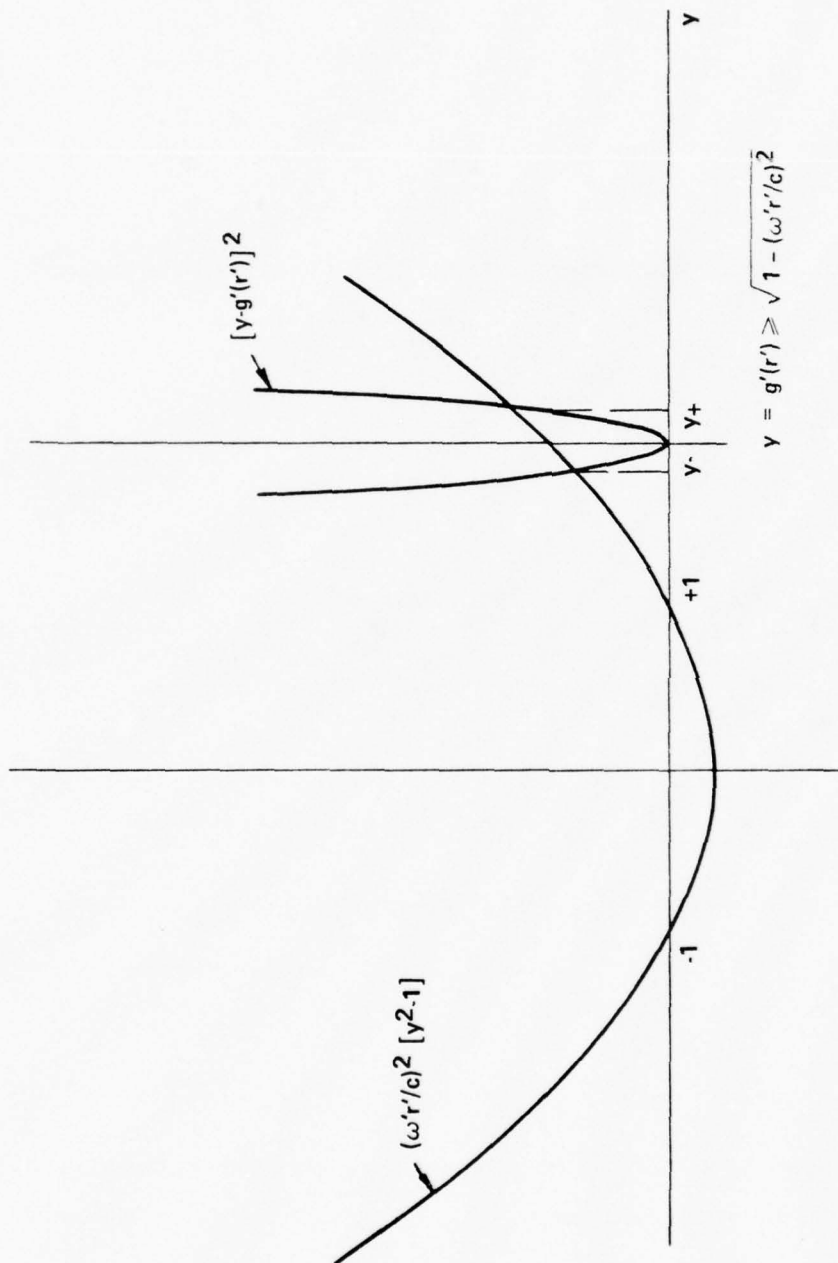
Figure 7-20. Condition for Equilibrium, $y_- \leq y \leq y_+$.

with the additional requirements that

$$g'(r' > a') < \sqrt{1 - (\omega'r'/c)^2}$$

$$g'(r' < a') > \sqrt{1 - (\omega'r'/c)^2}$$

which must be verified <u>a posteriori.</u> These conditions ensure that the density vanishes for $r' > a'$ and is finite for $r' < a'$.

The moments of the distribution function may now be evaluated as follows:

$$n'(r') = K'm \int_{y_-}^{y_+} \sqrt{\frac{2y\,dy}{(\omega'r'/c)^2\,(y^2 - 1) - [y - g'(r')]^2}}$$

$$n'(r')\langle v'_\theta \rangle = \frac{K'mc^2}{\omega'r'} \int_{y_-}^{y_+} \sqrt{\frac{2\,[y - g'(r')]\,dy}{(\omega'r'/c)^2\,(y^2 - 1) - [y - g'(r')]^2}}$$

which yields the moments of $F(r', \underline{p}')$,

$$n'(r') = \frac{2\pi K'mg'(r')}{[1 - (\omega'r'/c)^2]^{3/2}} \equiv \frac{n'_o}{g'_o}\, g'(r')\,\gamma'^3_{\perp}(r')$$

$$\langle v'_\theta \rangle = \omega'r'$$

for $r' \leq a'$. The moments vanish for $r' > a'$. We have defined $n'_o = n'(r' = 0)$, $g'_o = g'(r' = 0)$ and $\gamma'_\perp = [1 - (\omega'r'/c)^2]^{-1/2}$.

We now transform to the laboratory frame and write Maxwell's equations. In the laboratory frame we have

$$n(r) = \frac{n_o}{g_o} g(r) \gamma_\perp^3 (r)$$

$$\langle v_{\hat\theta} \rangle = \omega r$$

$$\langle v_z \rangle = V_o$$

where

$$\gamma_\perp = [1 - (\gamma_o \omega r/c)^2]^{-1/2}$$

$$g(r) = \frac{\gamma_o}{mc^2} [\xi_o - \frac{e \omega r}{c} A_\theta + e (\Phi - \beta_o A_z)]$$

$$\xi_o = \xi'_o /\gamma_o .$$

Maxwell's equations may therefore be written as

$$\frac{1}{r} \frac{d}{dr} r E_r = \frac{-4\pi e n_o}{\xi_o} [\xi_o - \frac{e \omega r}{c} A_\theta + e (\Phi - \beta_o A_z)] \gamma_\perp^3 (r)$$

$$\frac{dB_z}{dr} = \frac{4\pi e n_o}{\xi_o} [\xi_o - \frac{e \omega r}{c} A_\theta + e (\Phi - \beta_o A_z)] \frac{\omega r}{c} \gamma_\perp^3 (r) .$$

By multiplying the first equation by $\omega r/c$ and adding to the second equation, we obtain

$$\frac{d}{dr} [B_z + \frac{\omega r}{c} E_r] = 0$$

or

$$B_z(r) + \frac{\omega r}{c} E_r(r) = B_z(0) \equiv B_i .$$

With this relation we can reduce the problem to a single equation for E_r,

$$\frac{d}{dr} \, \frac{1}{r\gamma_\perp^3} \, \frac{d}{dr} \, r E_r \; = \; \frac{1}{L_o^2} \; \left[\frac{E_r}{\gamma_\perp^2} \; + \; B_i \gamma_o^2 \, \frac{\omega r}{c} \right]$$

where

$$\frac{1}{L_o^2} \; = \; \frac{4\pi n_o e^2}{\gamma_o^2 \xi_o} \; .$$

This equation can be solved analytically in the limit $\gamma_\perp \simeq 1$, where the perpendicular motion is non-relativistic.   Define the dimensionless variables

$$x \; = \; r/L_o$$

$$f \; = \; E_r/B_i$$

$$\bar{\omega} \; = \; \omega L_o/c$$

$$\eta \; = \; \frac{\omega_p L_o}{c} \, \frac{\omega_p}{\Omega_i}$$

where

$$\omega_p^2 \; = \; \frac{4\pi n_o e^2}{\gamma_o m}$$

$$\Omega_i \; = \; \frac{e B_i}{\gamma_o mc} \; .$$

For $\gamma_\perp \simeq 1$, we obtain

$$\frac{d^2 f}{dx^2} \; + \; \frac{1}{x} \, \frac{df}{dx} \; - \; \left(1 + \frac{1}{x^2}\right) \, f = \gamma_o^2 \, \bar{\omega} x$$

57

with boundary conditions $f(0) = 0$, $f'(0) = -\eta/2$.

The solution is then

$$f(x) = [2\gamma_o^2\, \overline{\omega} - \eta]\, I_1(x) - \gamma_o^2\, \overline{\omega}\, x$$

and the corresponding potentials are

$$\Phi(x) = -\frac{\xi_o\gamma_o^2}{e}\, [1 - I_o(x)] + 2\gamma_o^2\, \overline{\omega} B_i L_o\, [1 - I_o(x) + \frac{x^2}{4}]$$

$$A_z(x) = \beta_o \Phi(x)$$

$$A_\theta(x) = B_i L_o\, [\frac{x}{2} + (\gamma_o^2\, \overline{\omega})^2\, \frac{x^3}{4} + \overline{\omega}\, (\eta - 2\gamma_o^2\, \overline{\omega})\, x\, I_2(x)]$$

where $\Phi(0) = 0$ has been assumed. From the equation for $g(r)$ we see that

$$g_o = g(0) = \frac{\gamma_o \xi_o}{mc^2} = (\frac{\omega_p L_o}{c})^2$$

and

$$\frac{g(r)}{g_o} = I_o(x) + \frac{2\gamma_o^2\, \overline{\omega}}{\eta}\, [1 - I_o(x) + \frac{x^2}{4}]$$

$$-\frac{\gamma_o^2\, \overline{\omega} x}{\eta}\, [\frac{x}{2} + (\overline{\omega}\gamma_o^2)^2\, \frac{x^3}{4} + \overline{\omega}(\eta - 2\overline{\omega}\gamma_o^2)\, x\, I_2(x)]$$

where $I_o(x)$, $I_1(x)$ and $I_2(x)$ are modified Bessel functions.

The assumption $\gamma_\perp \simeq 1$ implies that the diamagnetic contribution to B_z be small. In fact, the solution presented above is not exactly self-consistent as may be seen by computing the density from the solution for $f(x)$

$$n(x) = -n_o \frac{1}{\eta x} \frac{d}{dx} x f$$

$$= n_o \left[\left(1 - \frac{2\gamma_o^2 \bar{\omega}}{\eta}\right) I_o(x) + \frac{2\gamma_o^2 \bar{\omega}}{\eta} \right]$$

$$= \frac{n_o}{g_o} g(r)$$

which yields

$$\frac{g(r)}{g_o} = I_o(x) + \frac{2\gamma_o^2 \bar{\omega}}{\eta} \left[1 - I_o(x)\right]$$

which differs from the previous expression for $g(r)/g_o$ by just the diamagnetic contribution to A_θ, and is consistent with assuming $\gamma_\perp \simeq 1$.

In terms of

$$\bar{\omega}_o = \frac{1}{2\gamma_o^2} \eta$$

or

$$\omega_o = \frac{1}{2\gamma_o^2} \frac{\omega_p^2}{\Omega_i}$$

59

the equation for $g(r)/g_o$ becomes

$$\frac{g(r)}{g_o} = (1 - \frac{\bar{\omega}}{\bar{\omega}_o}) I_o(x) + \frac{\bar{\omega}}{\bar{\omega}_o}$$

and

$$\frac{g(a)}{g_o} = (1 - \frac{\bar{\omega}}{\bar{\omega}_o}) I_o(\frac{a}{L_o}) + \frac{\bar{\omega}}{\bar{\omega}_o}$$

defines the radius of the beam so that

$$\frac{\bar{\omega}}{\bar{\omega}_o} = \frac{I_o(a/L_o) - g_o^{-1}}{I_o(a/L_o) - 1}.$$

If $a/L_o \simeq \omega_p a/c \gg 1$, we obtain $\bar{\omega} \simeq \bar{\omega}_o$, and the density is approximately uniform. For this case the fields are

$$E_r(r) \simeq - 2\pi e n_o r$$

$$B_\theta(r) = \beta_o E_r$$

$$B_z(r) = B_i + \frac{2Ne\omega_o}{c}(\frac{r}{a})^2.$$

The conditions for this simple equilibrium are $\omega_p a/c > 1$ and $\omega_o a/c < 1/\gamma_o$, which may be summarized as

$$1/4 < \nu/\gamma_o < (\gamma_o^2/r)(\Omega_o/\omega_p)^2$$

where $\Omega_o = eB_o/\gamma_o mc$ and $B_o = B_i + 2Ne\omega_o/c$. This equation implies $B_i > B_o/2$, which places a limit on the diamagnetism of the beam. When this equation is satisfied, the resulting equilibrium is the same as that obtained using the two-mass approximation. This inequality, therefore, gives the condition for validity of the two-mass approximation.

60

We now turn to the numerical solution of the field equation for arbitrary $\gamma_\perp$. In terms of the dimensionless variables, we have

$$\frac{d}{dx} \frac{1}{x\gamma_\perp^3} \frac{d}{dx} xf = \frac{f}{2\gamma_\perp^2} + \gamma_0^2 \bar{\omega} x$$

with $f(o) = 0$ and $f'(o) = -\eta/2$. This equation may be expressed as two first-order differential equations,

$$\frac{df}{dx} = \gamma_\perp^3 h - \frac{1}{x} f$$

$$\frac{dh}{dx} = \frac{f}{2\gamma_\perp^2} + \gamma_0^2 \bar{\omega} x$$

with $f(o) = 0$ and $h(o) = -\eta$. In this notation

$$\gamma_\perp(x) = \left[1 - (\gamma_0 \bar{\omega} x)^2 \right]^{-1/2}$$

and the problem is specified by three input variables, γ_0, $\bar{\omega}$ and η. The physical range of x is $0 \leq x < x_c$, where $x_c = (\gamma_0 \bar{\omega})^{-1}$ is the point where $\gamma_\perp(x)$ becomes infinite.

We can reduce the problem to a two-variable parameter space with the following transformation:

$$\bar{x} = \gamma_0 \bar{\omega} x$$

$$\bar{f} = f/\gamma_0$$

$$\bar{h} = -h/\eta$$

with which we obtain

$$\frac{df}{d\bar{x}} = -\frac{\gamma_\perp^3 (\eta/\gamma_o)}{(\gamma_o \bar{\omega})} \; h - \frac{1}{\bar{x}} \; \bar{f}$$

$$\frac{dh}{d\bar{x}} = -\frac{1}{(\eta/\gamma_o)(\gamma_o \bar{\omega}) \gamma_\perp^2} \; f - \frac{\bar{x}}{(\eta/\gamma_o)(\gamma_o \bar{\omega})}$$

with $\bar{f}(o) = 0$ and $\bar{h}(o) = 1$. Here, $\gamma_\perp(\bar{x}) = (1 - \bar{x}^2)^{-1/2}$ and $0 \leq \bar{x} < 1$ is the physical range of $\bar{x}$. The problem now has only two input parameters, $\gamma_o \bar{\omega}$ and η/γ_o. These equations are solved by a standard Runge-Kutta integration procedure.

The two input parameters represent a two-dimensional parameter space which we may depict as a plane. Our first interest is to define the subset of this plane in which self-consistent equilibria exist. This region of the plane will be referred to as the equilibrium parameter space.

The density is given by

$$n(x)/n_o = -\frac{\gamma_o \omega}{\eta/\gamma_o} \; \frac{1}{\bar{x}} \; \frac{d}{d\bar{x}} \; \bar{x} \bar{f}(\bar{x})$$

$$= \gamma_\perp^3(\bar{x}) \; \bar{h}(\bar{x})$$

$$= \gamma_\perp^3(\bar{x}) \; \bar{g}(\bar{x})/g_o$$

or

$$\bar{g}(\bar{x})/g_o = \bar{h}(\bar{x}).$$

62

The condition for equilibrium is

$$g(\bar{x}) > \gamma_\perp^{-1}(\bar{x}) \text{ for } \bar{x} < \bar{a}$$

$$g(\bar{x}) < \gamma_\perp^{-1}(\bar{x}) \text{ for } \bar{x} > \bar{a}$$

with the beam radius, $\bar{x} = \bar{a}$, given by $g(\bar{a}) = \gamma_\perp^{-1}(\bar{a})$.

Since $g(o)/g_o = \gamma^{-1}(o) = 1$, we can satisfy the first condition only if $g_o > 1$. Furthermore, since $\gamma_\perp^{-1}(1) = 0$, the second condition requires that $\bar{h}(\bar{x})$ pass through zero somewhere in the interval, $0 < \bar{x} < 1$. Figure 7-21 illustrates the two types of equilibrium solutions which are possible. Curve "a" has the properly $\bar{h}(\bar{x}) < \gamma_\perp^{-1}(\bar{x})$ for all $\bar{x}$. Consequently, any $\bar{x}$ in the range $0 < \bar{x} < x_{max}$, where $\bar{h}(x_{max}) = 0$, can be the self-consistent beam radius with the suitable choice of g_o,

$$g_o = [\bar{h}(\bar{x}) \, \gamma_\perp(\bar{x})]^{-1}.$$

Curve "b", on the other hand, allows self-consistent solutions with beam radii in the range, $x_{min} < \bar{x} < x_{max}$, where $\bar{h}(x_{min}) = \gamma_\perp^{-1}(x_{min})$ and $\bar{h}(x_{max}) = 0$. Any $\bar{x}$ in this range can be the self-consistent beam radius with g_o given above.

For $\bar{x} > \bar{a}$, we must calculate $\bar{h}(\bar{x})$ from the vacuum field equations, with continuity at $\bar{x} = \bar{a}$ imposed as a boundary condition on the potentials and their first derivatives. The resulting expression is

$$\bar{h}(\bar{x} > \bar{a}) = \bar{h}(\bar{a}) - \frac{1}{2} \frac{\bar{a}^2}{(\gamma_o \, \omega)(\eta/\gamma_o)} \left[1 - \bar{a}\,\bar{f}(\bar{a})\right]\left[\frac{\bar{x}^2}{\bar{a}^2} - 1\right]$$

$$- \frac{\bar{a}\,\bar{f}(\bar{a})}{(\gamma_o \, \bar{\omega})(\eta/\gamma_o)} \, \ell n \left(\frac{\bar{x}}{\bar{a}}\right)$$

which must pass through zero somewhere in the internal, $\bar{a} < \bar{x} < 1$, as noted above.
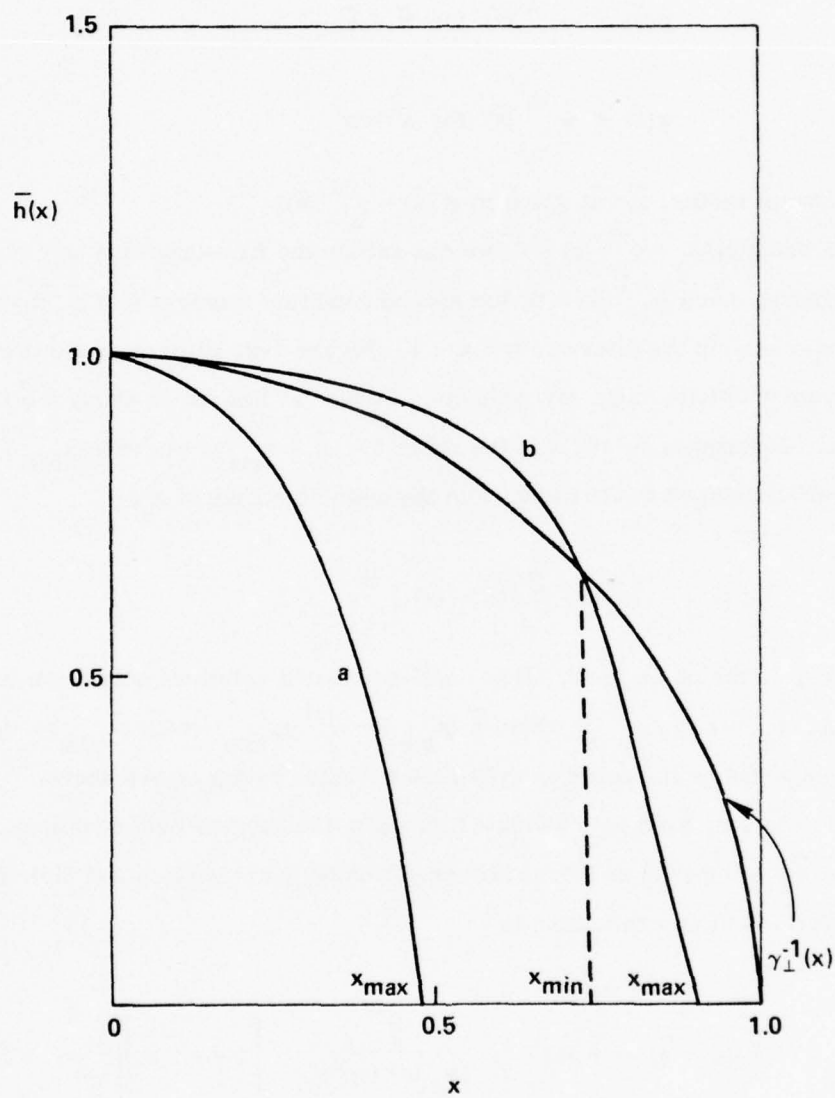
Figure 7-21. Equilibrium Solutions.

64

If we fix $\gamma_o \bar{\omega}$ and vary η/γ_o, we always find equilibrium solutions for small values of η/γ_o. As we increase η/γ_o, there is invariably some value at which the solution no longer satisfies $\bar{h}(\bar{x}) = 0$ somewhere in the $0 < \bar{x} < 1$ interval. Equilibrium solutions exist, therefore, only for η/γ_o less than a maximum value which depends on $\gamma_o \bar{\omega}$. The region of the parameter space where equilibria can be found is shown in Figure 7-22. For $\gamma_o \bar{\omega} < 0.3$ the equilibrium parameter space is bounded by the curve $\eta/\gamma_o = 2 \gamma_o \omega$, which is just the familiar result,

$$\omega = \frac{1}{2\gamma_o^2} \quad \frac{\omega_p^2}{\Omega_i} \; .$$

For larger values of $\gamma_o \bar{\omega}$, the boundary curve peaks at $\eta/\gamma_o = 0.63$ and $\gamma_o \bar{\omega} = 0.45$, and then falls off, approaching the curve $\eta/\gamma_o = 1/(2\gamma_o \bar{\omega})$ for $\gamma_o \bar{\omega} > 2$. In this region the maximum value of η is independent of γ_o.

The equilibrium parameter space shown in Figure 7-22 includes all possible equilibria. For application to an energy storage device, those equilibria which correspond to high ν/γ_o beams with large beam-field energy compared to the guide field energy are of particular interest. It is necessary, therefore, to examine the characteristics of the equilibria which are possible in various regions of the equilibrium parameter space.

Having fixed $\gamma_o \bar{\omega}$ and η/γ_o within the equilibrium parameter space, we can solve the field equations for $\bar{f}(\bar{x})$ and $\bar{h}(\bar{x})$, and we then know

$$\frac{\bar{n}(\bar{x})}{n_o} = \gamma_\perp^3 (\bar{x}) \, \bar{h}(\bar{x})$$

$$\frac{E_r(\bar{x})}{B_i} = \frac{1}{R_o} \qquad \frac{B_\theta(\bar{x})}{B_i} = \gamma_o \bar{f}(\bar{x})$$

$$\frac{B_z(\bar{x})}{B_i} = 1 - \bar{x} \, \bar{f}(\bar{x}) \quad .$$

65
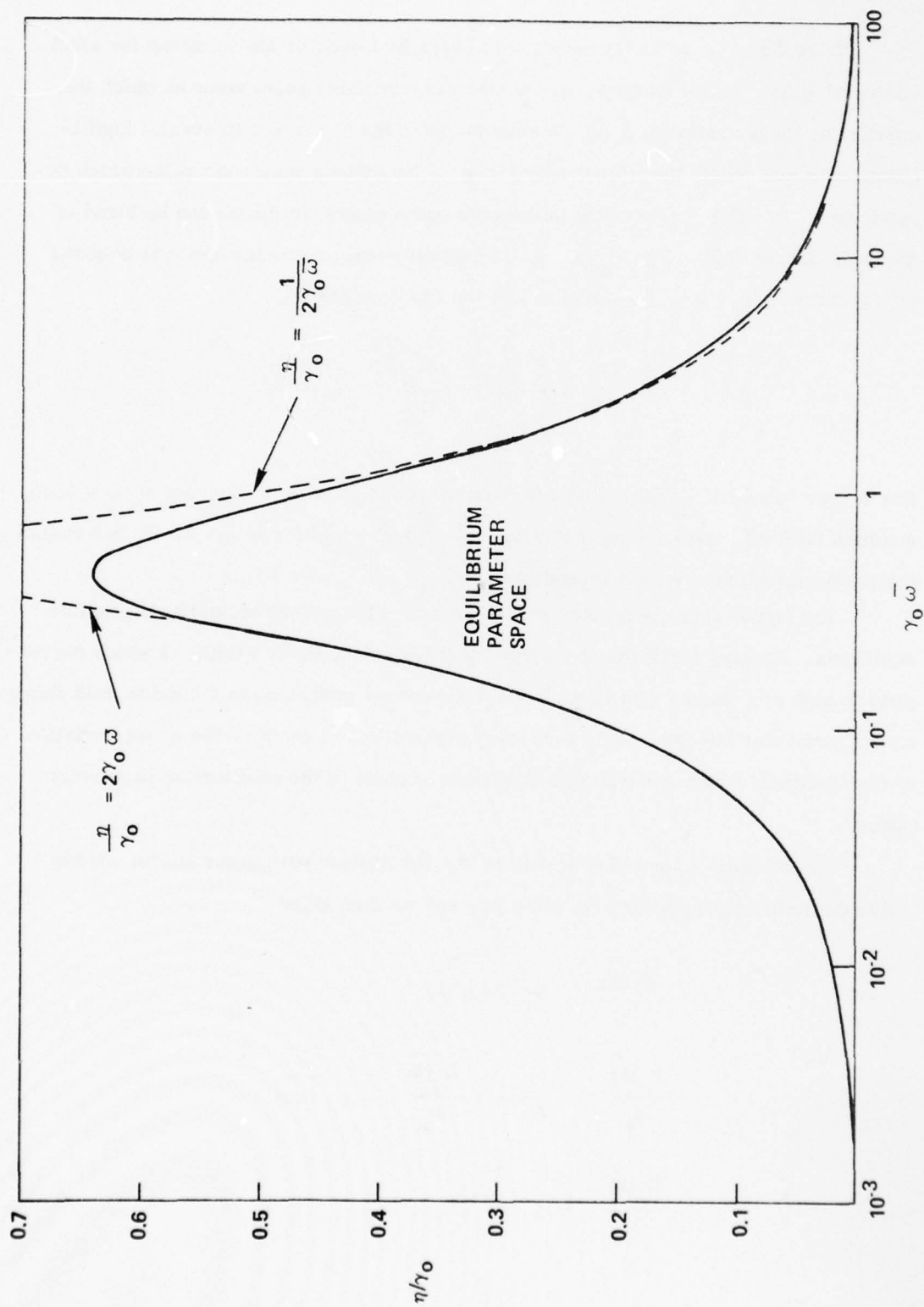
Figure 7-22. Equilibrium Parameter Space.

At any $\bar{x}$ we may calculate $g_o = [\bar{h}(\bar{x}) \, \gamma_\perp(\bar{x})]^{-1}$, and if $g_o > 1$, we may designate the chosen $\bar{x}$ as the (normalized) equilibrium beam radius, $\bar{a}$, which is numerically equal to $\gamma_o v_\theta(a)/c$. For $\bar{x} \geq \bar{a}$, the fields are given by

$$E_r(\bar{x}) = E_r(\bar{a}) \, \frac{\bar{a}}{\bar{x}} = \frac{1}{\beta_o} \, B_\theta(\bar{x})$$

$$B_z(\bar{x}) = B_o$$

where $B_o/B_i = 1 - \bar{a}\,\bar{f}(\bar{a})$ is the ratio of the external guide field to that at the center of the beam. This ratio measures the diamagnetic strength, $1 - B_i/B_o$.

In terms of these quantities, we may calculate ν/γ_o for the beam,

$$\frac{\nu}{\gamma_o} \equiv \frac{e^2}{\gamma_o mc^2} \int_0^a 2\pi r \, dr \, n(r)$$

$$= -\frac{1}{2} \frac{g_o}{(\eta/\gamma_o)(\gamma_o \omega)} \, \bar{a}\,\bar{f}(\bar{a})$$

If the beam is enclosed in a concentric conducting shell of radius, b, the self-field energy per unit length, W, is given by

$$\frac{W}{W_M} = \frac{2}{\bar{a}^2} \frac{2\gamma_o^2 - 1}{(b/a)^2 (B_o/B_i)^2} \left[\int_0^{\bar{a}} x dx \, \bar{f}^2(x) + \bar{a}^2 \bar{f}^2(\bar{a}) \, \ln \frac{b}{a} \right]$$

where $W_M \equiv \pi b^2 (B_o^2/8\pi)$ is the guide field energy per unit length. The integral in this equation is computed numerically along with the field equations for $\bar{f}$ and $\bar{h}$. The potential well depth, Φ_o, associated with the beam is given by

67

$$\frac{\Phi_o}{\gamma_o B_o b} = \frac{-1}{\bar{a}} \ \frac{1}{(b/a)(B_o/B_i)} \ \left[\int_0^{\bar{a}} \bar{f}(x) \, dx + \bar{a} \, \bar{f}(\bar{a}) \, \ell n \, \frac{b}{a} \right]$$

and this integral is also computed numerically.

To complete the specification of a particular equilibrium, we need to specify γ_o and either n_o or B_o. Knowing γ_o, we determine η and hence ω_p/Ω_o,

$$\frac{\omega_p}{\Omega_o} = \frac{B_i}{B_o} \ \frac{\eta}{\sqrt{g_o}}$$

which relates n_o and B_o. Since $g_o = (\omega_p L_o/c)^2$, we can determine L_o, and all equilibrium quantities are then known explicitly.

To illustrate the above discussion, we construct a particular equilibrium in detail. For example, for $\gamma_o \bar{\omega} = 0.3$ and $\eta/\gamma_o = 0.5$, which is within the equilibrium parameter space, we can discuss the self-consistent equilibrium having normalized beam radius, $\bar{a} = \gamma_o v_\theta(a)/c = 0.8$. In this example the results of the numerical integration of the field equations are $\bar{f}(0.8) = -0.826$, $\bar{h}(0.8) = 0.228$, $W/W_M = 0.114 \, (2\gamma_o^2 - 1)$ and $\Phi_o = 0.2875 \, \gamma_o B_o b$, for $b/a = 2$. The appropriate g_o for this beam radius is $g_o = 2.63$ since $\gamma_\perp(0.8) = 1.67$. With these results we can derive $\nu/\gamma_o = 5.80$, $\omega_p a/c = 4.33$, $\omega_p/\gamma_o \Omega_o = 0.185$ and $B_o/B_i = 1.66$.

For definiteness, we now specify $B_o = 20$ kG and $\gamma_o = 11$. Then, $\omega_p = 6.53 \times 10^{10}$ sec^{-1}, $n_o = 1.5 \times 10^{13}$ cm^{-3}, $L_o = 0.75$ cm, and the beam radius is $a = 2$ cm with $b = 4$ cm for the conducting outer wall. The guide field energy is $W_M = 80$ J/cm^3, and therefore the field energy associated with the beam is $W = 2.2$ kJ/cm since $W/W_M = 27.6$. The average energy density associated with the beam field is 44 J/cm, and the depth of the potential well between the beam center and the conducting wall is 75.5 MV. The electrostatic field is maximum at the beam edge, where $E_r = -33$ MV/cm and falls to $E_r = -16.5$ MV/cm at the wall.

The beam line density for this equilibrium is $N = 2.3 \times 10^{14}$ cm^{-1}, corresponding to 36.5 μC/cm of stored charge or a beam current, $I = 1.1$ MA. Since $\gamma_o \gamma_\perp = 18.3$, which is 8.85 MeV electron energy, the total kinetic energy of the beam is 320 J/cm. The equilibrium fields and density profile are plotted in Figure 7-23. On this figure we see that the beam density is close to uniform out to the beam edge.

Although the input parameters $\gamma_o \bar{\omega}$ and η/γ_o are useful for simplifying the solution to the field equations, they are not the most useful set when searching for a range of parameters in which favorable equilibria for energy storage are found. As the previous example illustrates, there is no question about the existence of equilibria which can store large quantities of energy. The remaining question concerns only the range of equilibrium parameters in which such equilibria exist.

Within the present formalism we must specify six parameters, $\gamma_o \bar{\omega}$, η/γ_o, $\gamma_o v_\theta (a)/c$, γ_o, b/a and either n_o or B_o, to completely specify an equilibrium solution. A more relevant set to the design of experiments would replace the first two parameters, $\gamma_o \bar{\omega}$ and η/γ_o, by $\omega_p a/c$ and $\omega_p/\gamma_o \Omega_i$ (there are many other possibilities). The relationship between these two sets of parameters follows from

$$\frac{\omega_p a}{c} = \sqrt{g_o} \, \frac{\bar{a}}{\gamma_o \bar{\omega}}$$

$$\frac{\omega_p}{\gamma_o \Omega_i} = \frac{\eta/\gamma_o}{\sqrt{g_o}}$$

or

$$\left(\frac{\omega_p a}{c} \right) \left(\frac{\omega_p}{\gamma_o \Omega_i} \right) = \bar{a} \, \frac{\eta/\gamma_o}{\gamma_o \bar{\omega}} \, .$$
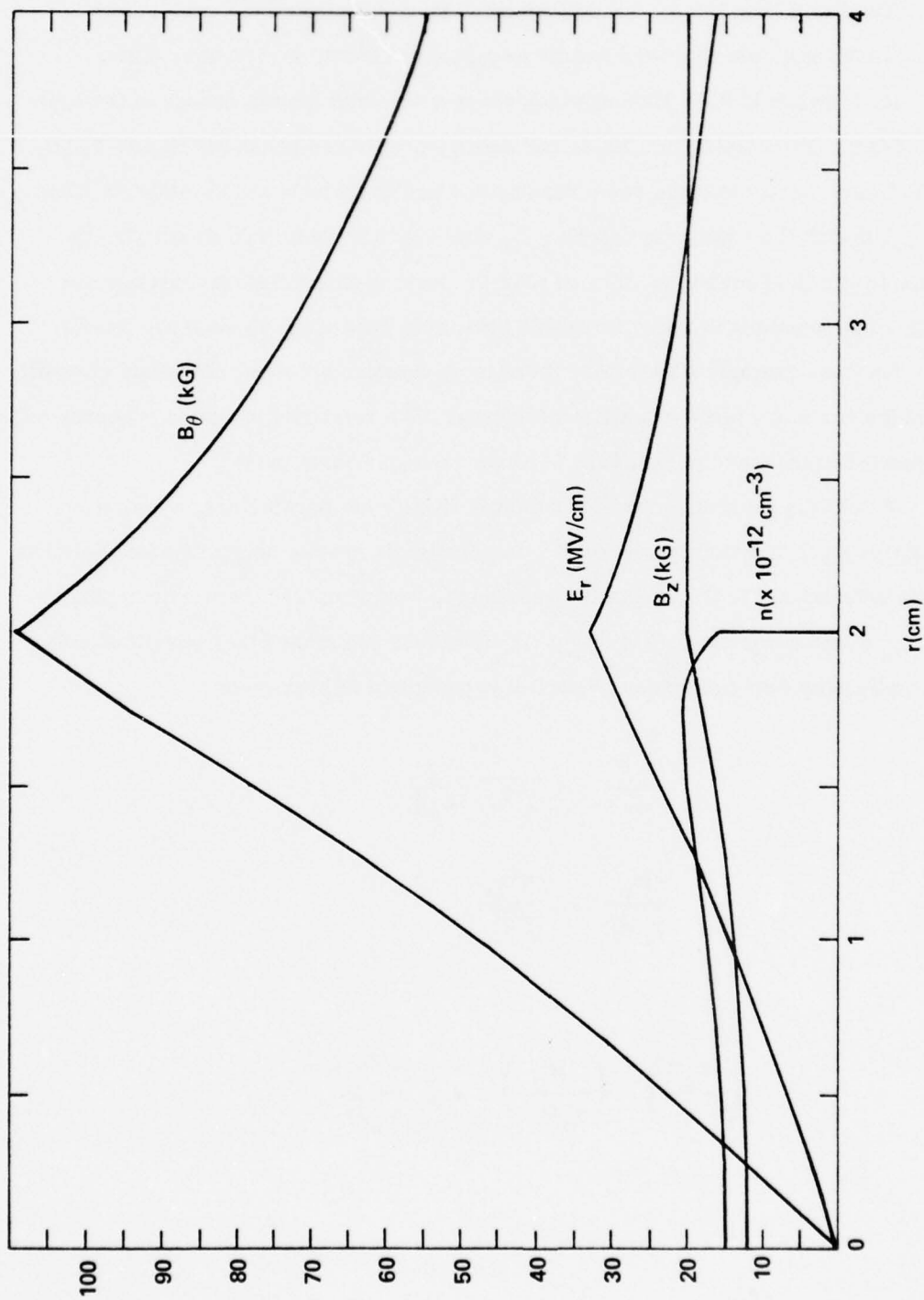
Figure 7-23. Equilibrium Density and Field Profiles for $\gamma_o \bar{\omega} = 0.3$, $\eta/\gamma_o = 0.5$, $\gamma_o v_\theta(a)/c = 0.8$, $\gamma_o = 11$ and $B_o = 20$ kG.

These equations give us a procedure for inverting our formalism so that $\omega_p a/c$ and $\omega_p/\gamma_o \Omega_i$ can be specified instead of $\gamma_o \bar{\omega}$ and η/γ_o. We first note that since $g_o > 1$ for equilibrium,

$$\frac{\eta}{\gamma_o} = \sqrt{g_o} \, \frac{\omega_p}{\gamma_o \Omega_i} > \frac{\omega_p}{\gamma_o \Omega_i}$$

is required. From Figure 7-22, there is a bounded region of $\gamma_o \bar{\omega}$ for which this inequality is satisfied. We need only examine values of $\gamma_o \bar{\omega}$ within this range. In particular, for $\omega_p/\gamma_o \Omega_i > 0.63$, there are no equilibria.

Having specified $\omega_p a/c$, $\omega_p/\gamma_o \Omega_i$ and $\bar{a} \equiv \gamma_o v_\theta (a)/c$, we pick a value for $\gamma_o \bar{\omega}$ within the range given by $\eta/\gamma_o > \omega_p/\gamma_o \Omega_i$ on Figure 7-22 and solve for η/γ_o,

$$\frac{\eta}{\gamma_o} = \frac{\gamma_o \bar{\omega}}{\bar{a}} \left(\frac{\omega_p a}{c} \right) \left(\frac{\omega_p}{\gamma_o \Omega_i} \right)$$

From Figure 7-22, we find the maximum value of (η/γ_o) at the particular choice of $\gamma_o \bar{\omega}$. For equilibria to be possible at all with these parameters, we must have

$$\left(\frac{\eta}{\gamma_o} \right)_{max} \geq \frac{\eta}{\gamma_o} > \frac{\omega_p}{\gamma_o \Omega_i}$$

If these conditions are violated, we choose a new value for $\gamma_o \bar{\omega}$ and begin again. When the inequality is satisfied, we integrate the field equations to $\bar{x} = \bar{a}$, and solve for g_o. If $g_o > 1$ is satisfied, we have a solution which has the correct value of the product, $(\omega_p a/c)(\omega_p/\gamma_o \Omega_i)$. We repeat this process for various values of $\gamma_o \bar{\omega}$ until a solution is obtained which also has the correct values of $\omega_p a/c$ and $\omega_p/\gamma_o \Omega_i$ individually.

Since $\eta/\gamma_o \leq 2\gamma_o\bar{\omega}$ for all points in the equilibrium parameter space, we know that equilibria are possible only for

$$\frac{\omega_p a}{c} \frac{\omega_p}{\gamma_o \Omega_i} \leq \frac{\gamma_o v_\theta(a)}{c} \quad .$$

We, therefore, define the composite parameter

$$\xi \equiv \frac{(\omega_p a/c)(\omega_p/\gamma_o \Omega_i)}{2\gamma_o v_\theta(a)/c} \leq 1.$$

In terms of this parameter, the two-mass approximation yields the beam-associated field energy per unit length as

$$\frac{W}{W_M} = 2(2\gamma_o^2 - 1)\left(\frac{a}{b}\right)^2 \left[\frac{(\gamma_o v_\theta/c)\xi}{1 + (\gamma_o v_\theta/c)^2 \xi}\right]^2 \left[\frac{1}{4} + \ln\frac{b}{a}\right].$$

In Figure 7-24 we plot this expression for comparison with the computed material results for W/W_M, with $b/a = 2$. For $\gamma_o v_\theta(a)/c = 0.2$ and 0.5, we see that the numerical results approach the two-mass result as ξ nears unity. This behavior is not surprising since $\xi = 1$ corresponds to the familiar relation, $\omega = \omega_p^2/2\gamma_o^2\Omega_i$. As we increase $\gamma_o v_\theta(a)/c$ to 0.9, where the two-mass approximation is not expected to hold, we find that W/W_M becomes larger than the two-mass result.

Similarly, Figure 7-25 presents the numerical results for ν/γ_o, which in the two-mass approximation is simply $\nu/\gamma_o = 0.25(\omega_p a/c)^2$. Again, we find that for $\gamma_o v_\theta(a)/c = 0.9$, the numerically calculated value of ν/γ_o lies above the two-mass result.

These calculations have shown that there is no new limit to the stored field energy as $\gamma_o v_\theta/c$ nears unity. In fact, self-consistent, fully relativistic equilibria at large values of $\gamma_o v_\theta(a)/c$ store larger quantities of energy than the two-mass approximation would predict.

72
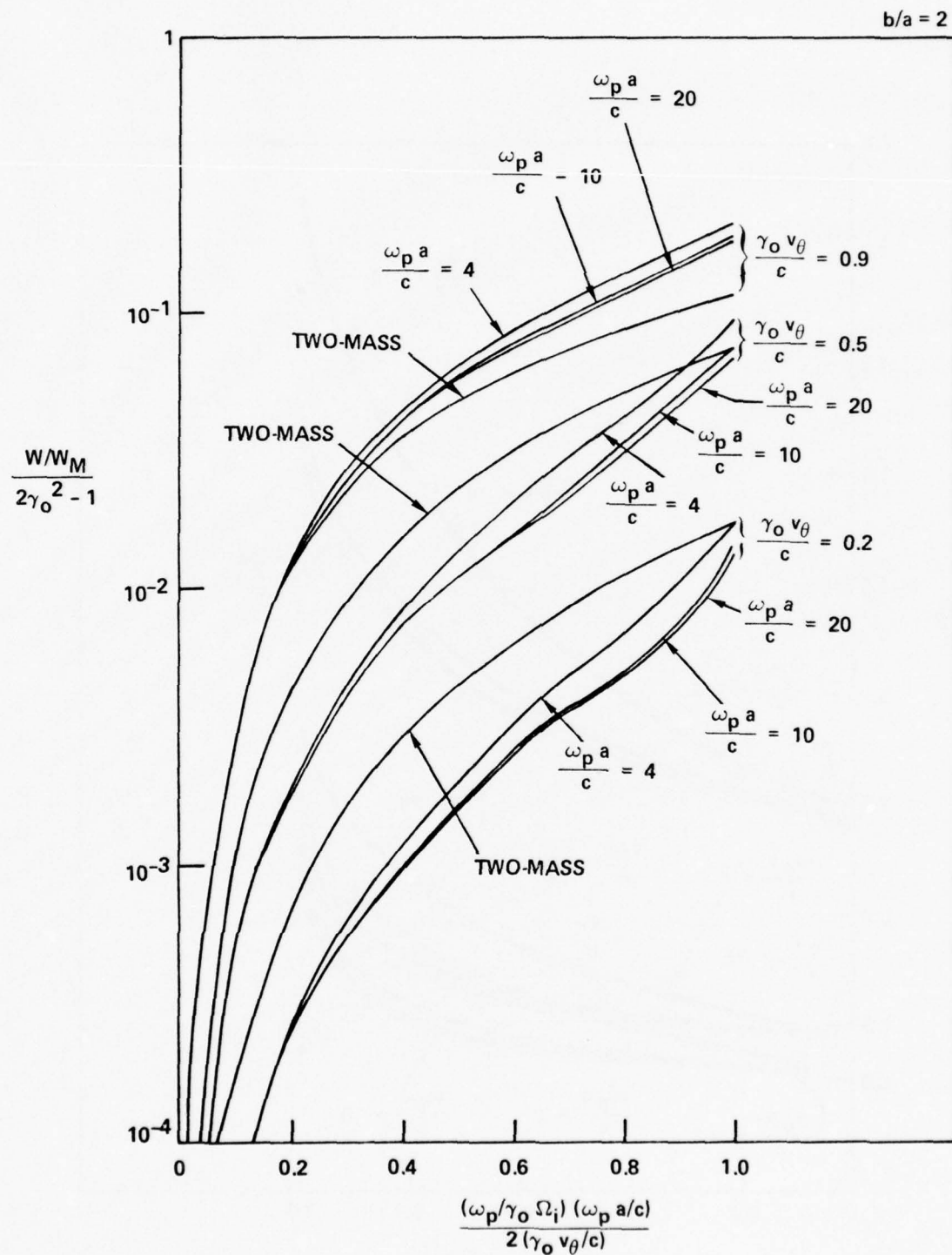
Figure 7-24. Beam-Associated Field Energy Normalized to Guide Field Energy. Rostoker-Hieronymus (Two-Mass) Result Plotted for Comparison.

73
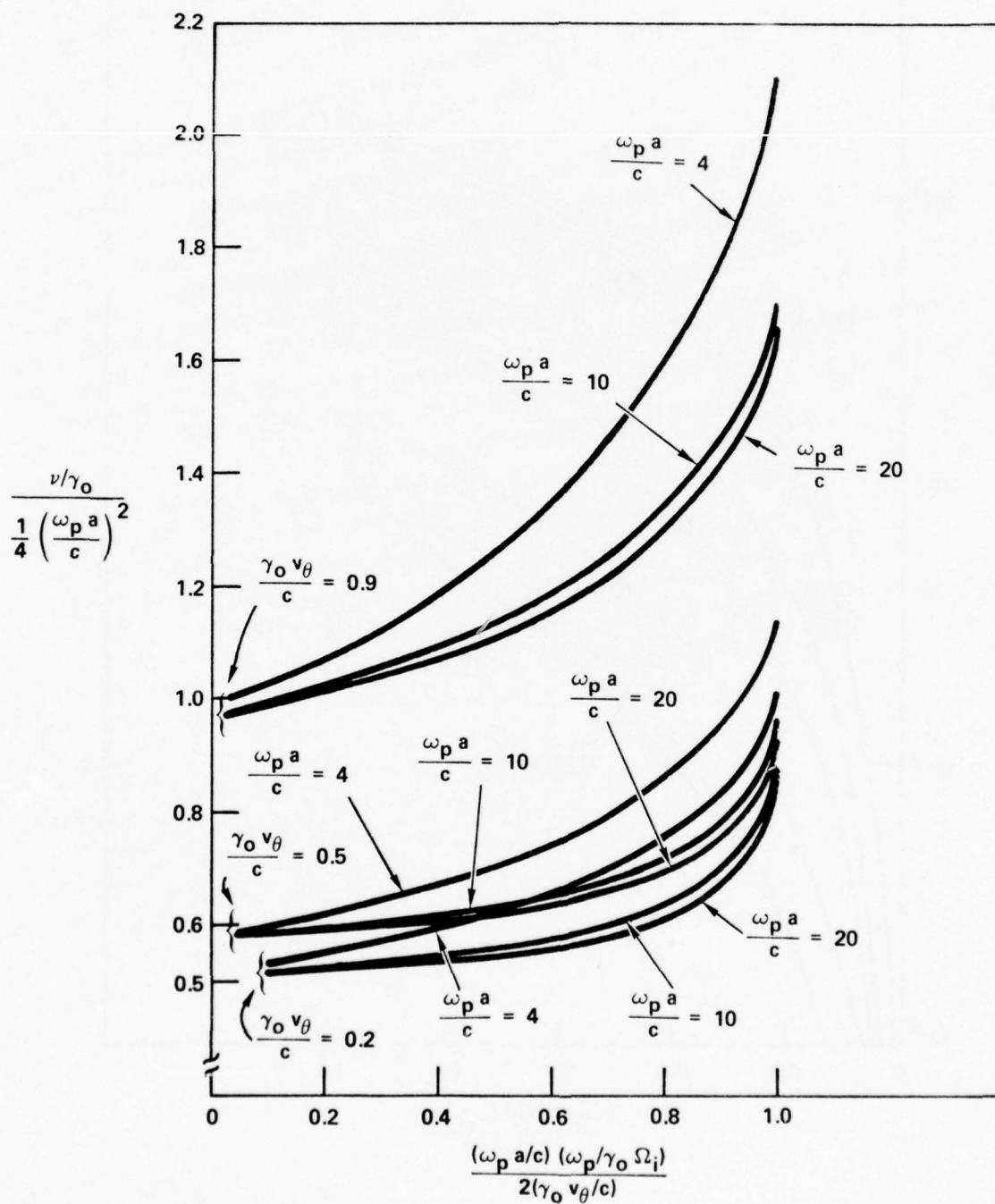
Figure 7-25. Curves of ν/γ_o. Uniform-Density Beam Has $\nu/\gamma_o = 1/4 \left(\dfrac{\omega_p a}{c} \right)^2$.

74

7.1.4   Relativistic Fluid Equations for Non-Neutral Plasma

A major obstacle in obtaining theoretical results for relativistic non-neutral
systems has been the nonexistence of a set of fluid equations with a physical basis
for closing the moment hierarchy. In the absence of such a set of equations, the
only available tool for theoretical equilibrium and stability analysis has been the
coupled Maxwell-Vlasov system of equations. This system yields analytical solu-
tions only in the simplest geometries. Fully-relativistic cylindrical rigid-rotor
equilibria, for example, require numerical integration for the equilibrium fields.
Stability analysis requires that the equilibrium particle orbits be employed as
characteristics to determine the perturbed distribution function, which in turn must
be integrable over momentum space to obtain a dispersion relation. Analytical
solutions are therefore very limited since the equilibrium fields themselves are
often not known analytically, and even then the particle orbits are usually known
only as quadratures, a form which is not useful as a characteristic. Numerical
solutions of the Maxwell-Vlasov system are possible, but generally require difficult
and expensive particle simulation techniques, which are beyond the scope of all
but the largest computers.

By contrast, non-relativistic neutral plasma physics has long benefited from
the existence of a closed hierarchy of MHD fluid equations, together with a number
of adiabatic laws and an energy principle for studying stability. This impressive
theoretical formalism has allowed the study of neutral plasma in such complicated
configurations as symmetric and asymmetric toroids, including toroids of non-
circular cross-section. Also, much of our understanding of the physical mechanisms
which underlies gross neutral plasma behavior comes from fluid analyses.

We have, therefore, undertaken the construction of a closed set of fluid
equations for non-neutral relativistic plasma. Aside from the obvious application
of such a set of equations to the electrostatic torus, a fully-relativistic system

of fluid equations would provide a significant tool in studying the physics of diodes, where the electron beam is usually non-neutral.

The most logical place to begin such an undertaking is with the two-mass approximation. Here, relativity enters in only a peripheral way, and problems associated with the non-neutrality of the system can be isolated and studied. To display the full complexity of the general problem, however, we will discuss the moments of the fully-relativistic Vlasov equation before specializing to the two-mass approximation. While it is inadequate for diode problems, the two-mass approximation is quite sufficient for describing the electron beam in an electrostatic torus, and for studying relativistic injection techniques.

The fully relativistic Vlasov equation may be written as

$$\frac{\partial f}{\partial t} + \underline{v} \cdot \nabla f - e \left[\underline{E} + \frac{1}{c} \underline{v} \times \underline{B} \right] \cdot \frac{\partial f}{\partial \underline{p}} = 0$$

where $\underline{p} = \gamma m \underline{v}$ and $\gamma = \left[1 + p^2/m^2 c^2 \right]^{1/2} = \left[1 - v^2/c^2 \right]^{-1/2}$. To compute the moments of this equation we define

$$n \equiv \int f \, d\underline{p}$$

$$\langle \cdots \rangle \equiv \frac{1}{n} \int (\dots) f \, d\underline{p} \quad .$$

The relativistic moment equations are then given by

$$\frac{\partial n}{\partial t} + \nabla \cdot n \langle \underline{v} \rangle = 0$$

$$\frac{\partial}{\partial t} \, n \langle \underline{v} \rangle + \nabla \cdot n \langle \underline{v} \, \underline{v} \rangle + \frac{ne}{m} \, \underline{E} \cdot \left\langle \frac{1}{\gamma} \, \underline{\underline{I}} - \frac{\underline{v} \, \underline{v}}{\gamma c^2} \right\rangle + \frac{ne}{mc} \, \left\langle \frac{\underline{v}}{\gamma} \right\rangle \times \underline{B} = 0$$

$$\frac{\partial}{\partial t} \, n \left\langle \frac{1}{\gamma} \right\rangle + \nabla \cdot n \left\langle \frac{\underline{v}}{\gamma} \right\rangle - \frac{1}{mc^2} \, ne \left\langle \frac{\underline{v}}{\gamma^2} \right\rangle \cdot \underline{E} = 0$$

$$\frac{\partial}{\partial t} n \left\langle \frac{\underline{v}}{\gamma} \right\rangle + \nabla \cdot n \left\langle \frac{\underline{v}\,\underline{v}}{\gamma} \right\rangle + \frac{ne}{m} \underline{E} \cdot \left\langle \frac{1}{\gamma^2} \underline{\underline{I}} - \frac{2\,\underline{v}\,\underline{v}}{\gamma^2 c^2} \right\rangle + \frac{ne}{mc} \left\langle \frac{\underline{v}}{\gamma^2} \right\rangle \times \underline{B} = 0$$

$$\frac{\partial}{\partial t} n \langle \underline{v}\,\underline{v} \rangle + \nabla \cdot n \langle \underline{v}\,\underline{v}\,\underline{v} \rangle + \frac{ne}{m} \left[\underline{E} \left\langle \frac{\underline{v}}{\gamma} \right\rangle + \left\langle \frac{\underline{v}}{\gamma} \right\rangle \underline{E} - \frac{2}{c^2} \underline{E} \cdot \left\langle \frac{\underline{v}\,\underline{v}\,\underline{v}}{\gamma} \right\rangle \right]$$

$$+ \frac{ne}{mc} \left[\left\langle \frac{(\underline{v} \times \underline{B})\,\underline{v}}{\gamma} \right\rangle + \left\langle \frac{\underline{v}\,(\underline{v} \times \underline{B})}{\gamma} \right\rangle \right] = 0$$

$$\frac{\partial}{\partial t} n \left\langle \frac{\underline{v}\,\underline{v}}{\gamma} \right\rangle + \nabla \cdot n \left\langle \frac{\underline{v}\,\underline{v}\,\underline{v}}{\gamma} \right\rangle + \frac{ne}{m} \left[\underline{E} \left\langle \frac{\underline{v}}{\gamma^2} \right\rangle + \left\langle \frac{\underline{v}}{\gamma^2} \right\rangle \underline{E} - \frac{3}{c^2} \underline{E} \cdot \left\langle \frac{\underline{v}\,\underline{v}\,\underline{v}}{\gamma^2} \right\rangle \right]$$

$$+ \frac{ne}{mc} \left[\left\langle \frac{(\underline{v} \times \underline{B})\,\underline{v}}{\gamma^2} \right\rangle + \left\langle \frac{\underline{v}\,(\underline{v} \times \underline{B})}{\gamma^2} \right\rangle \right] = 0 \quad .$$

The equations are the usual continuity equation, which is the zeroth-moment of Vlasov's equation, together with the $\underline{v}$-moment, $\int d\underline{p}\,\underline{v}\,\left[\text{Vlasov Equ.}\right]$, which is necessary to determine $\langle \underline{v} \rangle$ in the continuity equation. The remaining equations, which are the moments with respect to γ^{-1}, $\underline{v}/\gamma$, $\underline{v}\,\underline{v}$ and $\underline{v}\,\underline{v}/\gamma$, are all required to close the second ($\underline{v}$-moment) equation. The moment hierarchy which is obtained by this procedure is seen to be a multiply-branched system, in which each moment couples not only to the next moment, but to several higher moments as well. This property precludes closure of the set in the usual manner, i.e. by neglecting a single quantity such as heat flow. The situation is more complicated here compared with the non-relativistic moment equations because of the occurence of γ in relativistic mechanics. In the non-relativistic domain only moments with respect to 1, $\underline{v}$, $\underline{v}\,\underline{v}$, etc. need be computed because $\underline{p} = m\underline{v}$ and kinetic energy is $E = mv^2/2$, i.e., half the trace of the $\underline{v}\,\underline{v}$-moment. Relativistic mechanics has $\underline{p} = \gamma m\underline{v}$ and $E = \gamma mc^2$, which requires a distinction between $\underline{p}$ and $\underline{v}$ moments, as well as requiring separate moment equations for energy (the γ-moment) and pressure

(the $\underline{p}\,\underline{v}$-moment). At the present time there is no general physical technique for terminating the relativistic hierarchy of moment equations.

For various specific applications the hierarchy can be closed by postulating the form of the distribution function, which is then employed to explicitly calculate the form of the unknown quantities required for closure. This technique was employed by Toepfer[2], who used a relativistic Maxwellian to study steady-state solutions, and by Mosher[3], who employed a mono-energetic distribution to study e-beam interactions with high-Z plasma. The results obtained by this technique are only as valid as the assumed distribution function. In Toepfer's work, for example, the use of a Maxwellian to study steady-state problems is reasonable since the departure from a Maxwellian behavior is only valid in the collisional regime where equilibrium times are short.

We turn now to the two-mass approximation, in which the electrons are relativistic in one direction only, i.e., $v_z = V + (v_z - V)$, where $V \gg v_\perp$, $|v_z - V|$. In this approximation, V is a constant, $\beta_o \equiv V/c$, and $\gamma_o \equiv (1 - \beta_o^2)^{-1/2}$. Rigid-rotor Vlasov equilibrium and stability analysis in both cylindrical and large aspect-ratio toroidal geometries have been performed in this approximation by Rostoker and Hieronymus[4]. These results have been presented in a previous Final Report.

The Vlasov equation in the two-mass approximation is written as

$$\frac{\partial f}{\partial f} + \underline{v} \cdot \nabla f - \frac{e}{\gamma_o m} \left[\underline{E}_\perp + \frac{1}{c} (\underline{v} \times \underline{B})_\perp \right] \cdot \frac{\partial f}{\partial \underline{v}_\perp} - \frac{e}{\gamma_o^3 m} \left[E_\parallel + \frac{1}{c} (\underline{v} \times \underline{B})_\parallel \right] \cdot \frac{\partial f}{\partial \underline{v}_\parallel} = 0$$

where $f = f(\underline{x}, \underline{v}, t)$ and $\perp$, $\parallel$ refer to directions perpendicular and parallel to $\underline{V}$.

---

[2] A.J. Toepfer, Phys. Rev. $\underline{A3}$, 1444 (1971).

[3] D. Mosher, Bull. Am. Phys. So. $\underline{19}$, 856 (1974).

[4] J. Hieronymus, Ph.D. Thesis, Cornell University (1971).

We define the quantities,

$$n \equiv \int f \, d\underline{v}$$

$$\bar{n} <\underline{v}> = \int \underline{v} \, f \, d\underline{v}$$

$$\underline{\underline{P}} \equiv m \int (\underline{v} - <\underline{v}>)(\underline{v} - <\underline{v}>) \, f \, d\underline{v}$$

$$\underline{\underline{Q}} \equiv m \int (\underline{v} - <\underline{v}>)(\underline{v} - <\underline{v}>)(\underline{v} - <\underline{v}>) \, f \, d\underline{v} \quad .$$

With these definitions, the first three moments of Vlasov's equation are

$$\frac{\partial n}{\partial t} + \nabla \cdot n <\underline{v}> = 0$$

$$nm \frac{d<\underline{v}>}{dt} = -\nabla \cdot \underline{\underline{P}} - \frac{ne}{\gamma_o} \left[\underline{E}_\perp + \frac{1}{c} (<\underline{v}> \times \underline{B})_\perp \right] - \frac{ne}{\gamma_o^3} \left[\underline{E}_\parallel + \frac{1}{c} (<\underline{v}> \times \underline{B})_\parallel \right]$$

$$\frac{\partial}{\partial t} \underline{\underline{P}} + \nabla \cdot \left[<\underline{v}> \underline{\underline{P}} + \underline{\underline{Q}} \right] + \underline{\underline{P}} \cdot \nabla <\underline{v}> + \left[\underline{\underline{P}} \cdot \nabla <\underline{v}> \right]^T$$

$$+ \frac{e}{\gamma_o mc} \left[\underline{\underline{P}} \, (\times \underline{B})_\perp - (\underline{B}\times)_\perp \underline{\underline{P}} \right] + \frac{e}{\gamma_o^3 mc} \left[\underline{\underline{P}} \, (\times \underline{B})_\parallel - (\underline{B} \times)_\parallel \underline{\underline{P}} \right] = 0$$

where $d/dt \equiv \partial/\partial t + <\underline{v}> \cdot \nabla$ and the cross-product operators $(\underline{B}\times)_{\perp, \parallel}$ and $(\times\underline{B})_{\perp, \parallel}$ are defined by

$$(\underline{B}\times)_{\perp, \parallel} \, \underline{w} \equiv (\underline{B} \times \underline{w})_{\perp, \parallel}$$

$$\underline{w} \, (\times\underline{B})_{\perp, \parallel} \equiv (\underline{w}\times \underline{B})_{\perp, \parallel}$$

for any vector $\underline{w}$. Here again $\perp, \parallel$ are with respect to $\underline{V}$. The quantity $\left[\underline{\underline{P}} \cdot \nabla <\underline{v}> \right]^T$

79

is the transpose of $\underline{\underline{P}} \cdot \nabla <\underline{v}>$.

This set of equations may be closed by setting the heat flow tensor to zero, i.e. $\underline{\underline{Q}} = 0$. Unlike ordinary one-fluid MHD theory, however, it is unnecessary to assume a form of Ohm's law to complete the equations. In particular, the infinite conductivity assumption, $\underline{E} + <\underline{v}> \times \underline{B}/c = 0$, is very restrictive for the single-species equations considered here. This assumption would drop all electromagnetic terms from the force equation since for a pure electron plasma the current density is $\underline{J} = -ne <\underline{v}>$ and the charge density is $\rho = -ne$. The infinite conductivity equation is therefore equivalent to setting $\rho \underline{E} + \underline{J} \times \underline{B}/c = 0$. In the one-fluid MHD equations[5] the situation is entirely different because infinite conductivity is expressed as $\underline{E} + \underline{U} \times \underline{B}/c = 0$ where $\underline{U}$ is the center-of-mass velocity given by

$$\underline{U} \equiv \frac{\sum mn <\underline{v}>}{\sum mn}$$

and the summation is over particle species.

To check the fluid equations, we begin by comparing the steady-state solutions from the Vlasov formalism with the steady-state fluid equations. To construct an exact two-mass Vlasov equilibrium, we begin with the two-mass equations of motion,

$$\gamma_o m \left[\frac{d v_r}{dt} - \frac{v_\theta^2}{r} \right] = -e \left[E_r + \frac{1}{c} v_\theta B_z - \frac{1}{c} v_z B_\theta \right]$$

$$\gamma_o m \left[\frac{d v_\theta}{dt} + \frac{v_r v_\theta}{r} \right] = \frac{e}{c} v_r B_z$$

$$\gamma_o^3 m \frac{d v_z}{dt} = -\frac{e}{c} v_r B_\theta$$

---

[5] See for example I.B. Bernstein and S.K. Trehan, Nucl. Fusion $\underline{1}$, 3 (1960).

for a cylindrical beam with self-consistent fields E_r, B_θ, B_z which are functions of the radial coordinate only. The constants of motion associated with the equations of motion are

$$H = \frac{1}{2}\gamma_o m (v_r^2 + v_\theta^2) + \frac{1}{2}\gamma_o^3 m v_z^2 - e\, \Phi\,(r)$$

$$P_\theta = \gamma_o m r\, v_\theta - \frac{e}{c} r\, A_\theta\,(r)$$

$$P_z = \gamma_o^3 m\, v_z - \frac{e}{c} A_z\,(r) \quad.$$

We write the equilibrium distribution function as

$$F(\underline{x},\ \underline{v}) = \frac{\gamma_o^4 m^2}{2\pi}\ n_o\, \delta\,(H - \omega_o P_\theta - \epsilon_o)\, \delta\,(P_z - \gamma_o^3 m\, V)$$

$$= \frac{\gamma_o m}{2\pi}\, n_o\, \delta\,[W_\perp + \frac{1}{2}\gamma_o^3 m\, v_z^2 + U(r)]\, \delta\,[v_z - \frac{e}{\gamma_o^3 mc} A_z - V]$$

where

$$W_\perp = \frac{1}{2}\,\gamma_o m\,[v_r^2 + (v_\theta - \omega_o r)^2]$$

$$U(r) = \frac{e}{c}\omega_o r\, A_\theta - e\Phi - \frac{1}{2}\gamma_o m\,(\omega_o r)^2 - \epsilon_o \quad.$$

The moments of $F(\underline{x},\ \underline{v})$ which are required to determine the equilibrium fields are

$$.\ n(r) = n_o \Theta\,(a-r)$$

$$n(r) <v_\theta> = n_o \omega_o r\, \Theta\,(a-r)$$

$$n(r) <v_z> = n_o\,(V + \frac{e}{\gamma_o^3 mc} A_z)\, \Theta\,(a-r)$$

81

where $\Theta(x)$ is the unit step function, which is unity for $x \geq 0$ and zero for $x < 0$.
The beam radius, $r = a$, is given by $\psi(a) = 0$, where

$$\psi(r) = \frac{1}{2} \gamma_o^3 m \left(V + \frac{e}{\gamma_o^3 mc} A_z\right)^2 + U(r)$$

and we have assumed $\psi(r<a) < 0$ and $\psi(r>a) > 0$ as can be demonstrated a posteriori.
Higher moments of $F(\underline{x}, \underline{v})$, which are required in the steady-state fluid equations
are

$$P_{rr} = P_{\theta\theta} = -\gamma_o^{-1} n_o \psi(r) \Theta(a-r)$$

$$\underline{\underline{Q}} = 0 .$$

The remaining components of the pressure tensor are zero, and also $<v_r> = 0$.

We can now show that the steady-state fluid equations are satisfied. The
continuity equation is

$$\nabla \cdot n <\underline{v}> = n \nabla \cdot <\underline{v}> + <\underline{v}> \cdot \nabla n = 0$$

which is satisfied because $<v_r> = 0$ and all quantities depend only on r. We therefore
have

$$n \nabla \cdot <\underline{v}> = <\underline{v}> \cdot \nabla n = 0 .$$

The θ and z components of the momentum equation are trivially staisfied. The
radial component is also satisfied because

$$\nabla \cdot \underline{\underline{P}} = \hat{e}_r \left[n_o m \omega_o^2 r - \frac{n_o e}{\gamma_o} \left(E_r + \frac{<v_\theta>}{c} B_z - \frac{<v_z>}{c} B_\theta \right) \right]$$

$$= - \left[n m <\underline{v}> \cdot \nabla <\underline{v}> + \frac{ne}{\gamma_o} \left(\underline{E} + \frac{1}{c} <\underline{v}> \times \underline{B} \right) \right] \cdot \hat{e}_r \hat{e}_r .$$

The pressure equation is satisfied because

$$\nabla \cdot <\underline{v}> \underline{\underline{P}} = <\underline{v}> \cdot \nabla \underline{\underline{P}} = 0$$

$$\frac{e}{\gamma_o mc} \left[\underline{\underline{P}} \, (x\underline{B})_\perp - (\underline{B}x)_\perp \, \underline{\underline{P}} \right] = 0$$

while

$$\underline{\underline{P}} \cdot \nabla <\underline{v}> + \left[\underline{\underline{P}} \cdot \nabla <\underline{v}> \right]^T = -\frac{e}{\gamma_o^3 mc} \left[\underline{\underline{P}} \, (x\underline{B})_{\shortparallel} - (\underline{B}x)_{\shortparallel} \, \underline{\underline{P}} \right]$$

$$= \frac{n_o e}{\gamma_o^4 mc} \, \psi(r) \, B_\theta \, [\hat{e}_r \hat{e}_z + \hat{e}_z \hat{e}_r] \ .$$

We used $\nabla \cdot <\underline{v}> = 0$, $<v_r> = 0$ and $\underline{\underline{P}} = \underline{\underline{P}}(r)$ in obtaining the above results. The steady-state fluid equations are therefore satisfied by the moments of a Vlasov equilibrium.

To complete the equilibrium calculation, we compute the fields from Maxwell's equations. The result can be used to calculate $<v_z>$ explicitly,

$$<v_z> = V + \frac{e}{\gamma_o^3 mc} A_z(r) = V I_o \left(\frac{\omega_p r}{\gamma_o c} \right)$$

where I_o is the modified Bessel function of zero order and $\omega_p^2 = 4\pi n_o e^2 / \gamma_o m$. For this solution to be meaningful, we must require $V \gg |<v_z> - V|$, which implies that the argument of the Bessel function be small. The equilibrium is therefore valid when

$$\nu / \gamma_o^3 \ll 1/4$$

which is only a weak restriction on ν / γ_o. In this limit the equilibrium obtained above reduces exactly to the Rostoker-Hieronymus two-mass equilibrium.

83

Returning now to the full set of fluid equations, closed with the assumption $\underline{\underline{Q}} = 0$, we can establish the adiabatic law for isotropic pressure, $\underline{\underline{P}} = p\,\underline{\underline{I}}$, by taking the trace of the pressure equation,

$$3\,\frac{dp}{dt} + 5p\,\nabla \cdot \langle\underline{v}\rangle = 0 \ .$$

We use $\nabla \cdot \langle\underline{v}\rangle = -n^{-1}\,dn/dt$, which follows from the continuity equation, to obtain the adiabatic equation of state

$$\frac{d}{dt}\,(pn^{-5/3}) = 0.$$

The same result follows from ordinary one-fluid MHD, provided the additional assumption of infinite conductivity is made. The adiabatic law for the two-mass fluid equations does not require this assumption. As an aside, we note that the double-adiabatic law, or Chew-Goldberger-Low theory, does not follow from our set of fluid equations.

Using the adiabatic law derived above, the linearized fluid equations may be written as

$$\frac{\partial n_1}{\partial t} + \nabla \cdot n_1 \underline{v}_o = -\nabla \cdot n_o \underline{v}_1$$

$$n_o m \left[\frac{\partial \underline{v}_1}{\partial t} + \underline{v}_o \cdot \nabla \underline{v}_1 + \underline{v}_1 \cdot \nabla \underline{v}_o \right] + n_1 m \underline{v}_o \cdot \nabla \underline{v}_o$$

$$= -\nabla p_1 - \frac{n_o e}{\gamma_o} \left[\underline{E}_{1\perp} + \frac{1}{c}\,(\underline{v}_o \times \underline{B}_1)_\perp + \frac{1}{c}\,(\underline{v}_1 \times \underline{B}_o)_\perp \right]$$

$$- \frac{n_o e}{\gamma_o^3} \left[\underline{E}_{1\parallel} + \frac{1}{c}\,(\underline{v}_o \times \underline{B}_1)_\parallel + \frac{1}{c}\,(\underline{v}_1 \times \underline{B}_o)_\parallel \right]$$

$$- \frac{n_1 e}{\gamma_o} \left[\underline{E}_{o\perp} + \frac{1}{c}\,(\underline{v}_o \times \underline{B}_o)_\perp \right] - \frac{n_1 e}{\gamma_o^3} \left[\underline{E}_{o\parallel} + \frac{1}{c}\,(\underline{v}_o \times \underline{B}_o)_\parallel \right]$$

$$\frac{\partial p_1}{\partial t} + \underline{v}_o \cdot \nabla p_1 + \underline{v}_1 \cdot \nabla p_o = -\frac{5}{3} p_o \nabla \cdot \underline{v}_1 - \frac{5}{3} p_1 \nabla \cdot \underline{v}_o$$

$$\nabla \times \underline{E}_1 = -\frac{1}{c} \frac{\partial \underline{B}_1}{\partial t}$$

$$\nabla \times \underline{B}_1 = -\frac{4\pi e}{c} [n_o \underline{v}_1 + n_1 \underline{v}_o] + \frac{1}{c} \frac{\partial \underline{E}_1}{\partial t}$$

$$\nabla \cdot \underline{E}_1 = -4\pi e n_1 \qquad \nabla \cdot \underline{B}_1 = 0$$

where we have dropped the angle brackets, $\langle \ \rangle$, from our notation. The presence of the zero-order velocity, $\underline{v}_o$, is required by Earnshaw's theorem, which states that there are no static equilibria for an unneutralized collection of charged particles. A non-neutral equilibrium, therefore, must be dynamic in character. This feature of the equations spoils the usual derivation of the energy principle, which does not apply in its conventional form to non-neutral systems.

To study the stability of finite-radius equilibria, such as the rigid-rotor equilibrium described earlier, the linearized fluid equations become a coupled set of ordinary first-order differential equations which in general may be solved numerically by the Runge-Kutta integration procedure. Analytical solutions are possible in special cases.

As an example we analyze the well-known diocotron instability, and compare our result with Levy's non-relativistic analysis. We assume an equilibrium specified by $n_o(r), v_\theta^o(r), v_z^o(r), p_o(r), E_r^o(r), B_\theta^o(r), B_z^o(r)$ for an annular beam with inner radius, a, and outer radius, b. The diocotron mode is an electrostatic, incompressible, azimuthal mode of an unneutralized beam. We therefore specialize the analysis to perturbations which satisfy

$$\underline{E}_1 = -\nabla \Phi_1,$$
$$\underline{B}_1 = 0$$
$$\nabla \cdot \underline{v}_1 = 0$$

and assume all perturbed quantities to be of the form

$$n_1\,(r,\,\theta,\,t) \;=\; n_1(r)\,e^{i\ell\theta - i\omega t}$$

with no dependence on the z-coordinate.

   We define the frequencies

$$\Omega_\theta \;=\; \frac{e\,B_\theta^{\,o}}{\gamma_o\,mc}$$

$$\Omega_z \;=\; \frac{e\,B_z^{\,o}}{\gamma_o\,mc}$$

$$\bar\omega \;=\; \omega - \frac{\ell\,v_\theta^{\,o}}{r}$$

and solve for v_{1r} in the linearized momentum equations,

$$-i\,\bar\omega\,v_{1r} - \left(\frac{2\,v_\theta^{\,o}}{r} - \Omega_z\right)v_{1\theta} - \Omega_\theta v_{1z} \;=\; \frac{-1}{mn_o}\,\frac{dp_1}{dr} + \frac{n_1}{mn_o^2}\,\frac{dp_o}{dr} + \frac{e}{\gamma_o m}\,\frac{d\Phi_1}{dr}$$

$$-i\,\bar\omega\,v_{1\theta} + \left(\frac{1}{r}\,\frac{d}{dr}\,r\,v_\theta^{\,o} - \Omega_z\right)v_{1r} \;=\; \frac{-i\ell}{mn_o r}\,p_1 + \frac{ie\ell}{\gamma_o mr}\,\Phi_1$$

$$-i\,\bar\omega\,v_{1z} + \left(\frac{dv_z^{\,o}}{dr} + \frac{\Omega_\theta}{\gamma_o^2}\right)v_{1r} \;=\; 0\ .$$

The θ and z components of $\underline{v}_1$ are simply

$$v_{1\theta} \;=\; \frac{i\,v_{1r}}{\bar\omega}\left(\frac{1}{r}\,\frac{d}{dr}\,r\,v_\theta^{\,o} - \Omega_z\right) + \frac{\ell}{n_o m\bar\omega}\,\frac{p_1}{r} - \frac{\ell}{\bar\omega r}\,\frac{e\,\Phi_1}{\gamma_o m}$$

$$v_{1z} \;=\; \frac{-i\,v_{1r}}{\bar\omega}\left(\frac{d\,v_z^{\,o}}{dr} + \frac{\Omega_\theta}{\gamma_o^2}\right)\ .$$

Using the linearized pressure equation, we obtain

$$p_1 = \frac{-i\, v_{1r}}{\bar{\omega}} \; \frac{d\,p_o}{dr} \; .$$

Therefore

$$v_{1\theta} = \frac{i\, v_{1r}}{\bar{\omega}} \left(\frac{1}{r} \frac{d}{dr} r\, v_\theta^o - \Omega_z + \frac{\ell}{mn_o \bar{\omega} r} \frac{d\,p_o}{dr} \right) - \frac{\ell}{\bar{\omega} r} \frac{e\, \Phi_1}{\gamma_o m}$$

and v_{1r} is given by

$$\frac{-i\, v_{1r}}{\bar{\omega}} = \frac{1}{\bar{\Omega}^2} \left\{ \frac{n_1}{mn_o^2} \frac{d\,p_o}{dr} + \frac{e}{\gamma_o m} \left[\frac{d\,\Phi_1}{dr} - \left(\frac{2 v_\theta^o}{r} - \Omega_z \right) \frac{\ell}{\bar{\omega} r} \Phi_1 \right. \right.$$

$$\left. \left. - \frac{\ell^2}{mn_o \bar{\omega}^2 r^2} \frac{d\,p_o}{dr} \Phi_1 \right] \right\}$$

where

$$\bar{\Omega}^2 \equiv \bar{\omega}^2 - \left(\frac{2 v_\theta^o}{r} - \Omega_z \right) \left(\frac{1}{r} \frac{d}{dr} r\, v_\theta^o - \Omega_z \right) - \frac{2\ell}{mn_o \bar{\omega} r} \frac{d\,p_o}{dr} \left(\frac{2 v_\theta^o}{r} - \Omega_z \right)$$

$$- \Omega_\theta \left(\frac{d v_z^o}{dr} + \frac{\Omega_\theta}{\gamma_o^2} \right) \; .$$

The perturbed density then follows from the linearized continuity equation

$$n_1 = \frac{-i\, v_{1r}}{\bar{\omega}} \; \frac{d\,n_o}{dr}$$

which is the source function in Poisson's equation.

For an equilibrium with constant v_z^o and uniform density, n_o, within the annulus and for a pressure profile, $p_o(r)$, is goes smoothly to zero at the beam edges, Poisson's equation is simply

87

$$\frac{1}{r}\frac{d}{dr}\, r\,\frac{d\Phi_1}{dr} - \frac{\ell^2}{r^2}\,\Phi_1 = 0$$

with jump boundary conditions at the beam edges, $r = a$ and $r = b$. On the inner surface, for example, the jump condition is

$$\left(\frac{d\Phi_1}{dr}\right)_{a^+} - \left(\frac{d\Phi_1}{dr}\right)_{a^-} = \frac{\omega_p^2}{\bar{\Omega}^2(a)}\left[\left(\frac{d\Phi_1}{dr}\right)_{a^+} - \left(\frac{2\,v_\theta^o(a)}{a} - \Omega_z(a)\right)\frac{\ell\,\Phi_1(a)}{a\,\bar{\omega}(a)}\right]$$

where

$$\bar{\Omega}^2(a) = \left(\omega - \frac{\ell\,v_\theta^o(a)}{a}\right)^2 - \left(\frac{2\,v_\theta^o(a)}{a} - \Omega_z(a)\right)^2 - \frac{\Omega_\theta^2(a)}{\gamma_o^2} \ .$$

If we take the non-relativistic limit ($\gamma_o = 1$, $\Omega_\theta = 0$) and look for low frequency disturbances such that

$$\omega,\ \frac{v_\theta^o(a)}{a},\ \omega_p \ll \Omega_z(a)$$

we recover Levy's[6] formulation exactly. The stability analysis then proceeds as in Levy's work, where the characteristic frequency (or timescale) is seen to be ω_p^2/Ω_z. Retaining relativistic effects in our analysis, in the low-frequency regime, the characteristic frequency is reduced to $(\omega_p^2/\Omega_z)\,[1 + \Omega_\theta/\gamma_o\Omega_z)^2]^{-1}$, which implies a reduced growth rate for the instability in the relativistic regime. The condition for stability, that the beam have only one free surface, is the same in both the relativistic and non-relativistic regimes.

---

[6] R.H. Levy, Phys. Fluids 8, 1288 (1965).

7.1.5 Switching an Unneutralized Electron Beam in a Torus

Any analysis of switching an unneutralized electron beam in a torus must assume linear stability of the beam. Without linear stability the energy storage would not be possible since nearly any pure electron mode, if unstable, would grow at a rate comparable to $\omega_{pe} = (4\pi \, ne^2/\gamma_o m)^{1/2}$. At $n = 10^{12}$ cm^{-3} and $\gamma_o = 5$, we have $\omega_{pe}^{-1} \simeq 4 \times 10^{-11}$ sec. Any beam instability would e-fold in amplitude in <1 ns at this density and energy. The rapid growth rate for instabilities suggests one approach to switching, viz. changing some parameter to trigger an instability.

Given linear stability, the only instabilities possible are those which result from a large-amplitude perturbation, one comparable in magnitude to the equilibrium value for some quantity. For example, by inserting a rod into the torus, we can produce a kink perturbation with initial amplitude comparable to the beam radius. Alternatively, Rosenbluth has suggested that we switch the torus by injecting a fast plasmoid into the beam, thereby rapidly charge neutralizing a local region, i.e., $\delta E_r \sim E_r$, which results in an unstable neutral plasma mode.

A separate line of reasoning takes advantage of the linear stability of the beam. Such approaches as dropping a pellet into the beam or magnetically moving the beam into a metal target have been considered and rely on beam stability during switching.

The basic objective in all switching schemes is to charge neutralize and stop the beam in a time of order an electron transit time $\sim 2\pi R/c$. The external circuitry has time constants which are long compared with the switching time, and therefore the field energy will be dissipated in the target material heating it and producing x-rays by Bremsstrahlung.

Plasma Switch (Rosenbluth)

Fast theta-pinch hydrogen plasma guns can be made to produce $3 \times 10^{18} - 10^{19}$ electron-ion pairs. Typically, about 1% of these particles are emitted in a fast plasmoid, with velocities of $10^7 - 10^8$ cm/sec (plasmoid energy ≤ 100 J). Since the

total number of electrons in the beam is $\sim 10^{17}$ in a megajoule system (and $\sim 10^{16}$ in the STP), the fast plasmoid will charge neutralize a local region of the beam in ~ 10 ns.

A neutral plasma confined in a torus cannot carry current in excess of the Kruskal-Shafranov limit. A fully neutralized electrostatic torus would therefore be grossly unstable. With the disappearance of the electrostatic field in a local region, the B_θ field will be unopposed and cause the beam to pinch. This unstable pinch motion can stop a high ν/γ beam. Targets on the wall can be used for conversion to x-rays, or alternatively, the plasma itself, which is strongly heated during the beam pinching, can become the x-ray source.

"Rod-Plunger" Switch

By making a perturbation in the wall geometry, we affect the boundary conditions which determine the equilibrium fields. It is possible to actually destroy the equilibrium locally in this manner and force a specific perturbation (i.e. a kink) to grow. We imagine a cylindrical rod which is inserted through the torus wall and pushed toward the minor axis. Initially, the rod simply compresses all the fields, E_r, B_θ, B_z about equally. When the rod has been inserted to a depth comparable to its diameter, however, the magnetic field lines will begin to slip around the sides of the rod, while the electric field lines must continue to terminate on the rod. Further insertion of the rod, therefore, results in an enhancement in E_r, but little further compression of B_θ or B_z.

Increasing E_r causes the azimuthal drift speed v_θ to increase as electrons pass near the rod, forcing a kink-shaped perturbation to form. Let δE_r be the change in E_r due to the rod. Then the azimuthal speed is

$$\frac{v_\theta}{c} = \frac{E_r}{\gamma_o^2 B_z} + \frac{\delta E_r}{B_z}$$

and we see that $\delta E_r \sim E_r/\gamma_o^2$ suffices to make a large-amplitude perturbation in v_θ. As $\gamma_o v_\theta/c$ approaches unity, the azimuthal drift motion becomes energetically impossible and the electrons will be freely accelerated toward the rod.

The switching process can be triggered by biasing the rod positive as $\gamma_o v_\theta/c$ nears unity. A bias voltage ~ 10-100 kV can be rapidly applied, and results in the formation of a large-amplitude perturbation (amplitude $\sim$ beam radius) in a time $\lesssim 1$ ns. The large kink perturbation then grows very rapidly, with a characteristic growth time <1 ns, and drives the beam into the rod which acts as a target.

This mechanism does not rely on rapid insertion of the rod, but only on fast onset of the instability. The large E_r and B_θ fields of the beam itself are utilized in switching, the bias voltage acting only as a trigger.

Pellet Switch

Perhaps the simplest approach to switching consists of dropping a metal pellet into the beam to charge neutralize and stop the beam. The pellet then heats up and emits x rays. The main problem is getting the pellet into the beam. By charging the pellet positive, the large potential between the wall and beam surface ($\sim 10^7$ - 10^8 V) can be used as an accelerator. Pellet velocities up to $\sim 10^6$ cm/sec are attainable in this way. While the total beam mass ($\sim 10^{-8}$ g) is very small, the B_θ and B_z fields prevent the beam electrons from being drawn into the pellet. Clearly a technique for moving the beam into the pellet is required.

A means of shifting the beam equilibrium through the application of a vertical magnetic field appears feasible. This approach is discussed in detail in the following section. A vertical magnetic field of ~ 300 G suffices to displace the beam a distance comparable to its diameter in ~ 10 ns. A description of a technique for producing such a field in ~ 10 ns is also presented.

Switching By Vertical Magnetic Field

A vertical magnetic field is generally employed to adjust the equilibrium position in a Tokamak. We consider this possibility for a high ν/γ electron beam in

a torus. The objective is to displace the electron beam a distance of the order of the diameter of the beam in a time of the order of 10 ns. We conclude that this is feasible with state-of-the-art electrical engineering.

We begin with the orbit equations for relativistic electrons in a large aspect ratio torus[1]

$$m\gamma_o \left(\frac{dv_x}{dt} + \frac{V_z^2}{R} \right) = -e \left\{ (E_r - \beta B_\theta) \frac{x}{r} + \frac{1}{c} v_y B_z - \frac{1}{c} v_z B_y \right\}$$

$$m\gamma_o \frac{dv_y}{dt} = -e \left\{ (E_r - \beta B_\theta) \frac{y}{r} - \frac{1}{c} v_x B_z \right\}$$

$$v_z = V_z \left[1 + \frac{r}{R} \cos\theta \right]$$

(x, y, z) are local cartesian coordinates as illustrated in Figure 7-26, (r, θ) are local polar coordinates corresponding to (x, y). These equations are identical to Eq. (11) of reference 1 except for the addition of an external magnetic field B_y which results in the additional term $(e/c) v_z B_y$ in the x-component of the orbit equation. Since

$$-e(E_r - \beta B_\theta) \frac{x}{r} = \frac{\omega_p^2}{2\gamma_o^2} m\gamma_o x$$

where $\omega_p^2 = 4\pi n e^2 / \gamma_o m$ is the beam plasma frequency, the toroidal term $m\gamma_o V_z^2/R$ can be removed by the transformation

$$x' = x - \frac{2\gamma_o^2}{\omega_p^2} \frac{V_z^2}{R} \quad .$$

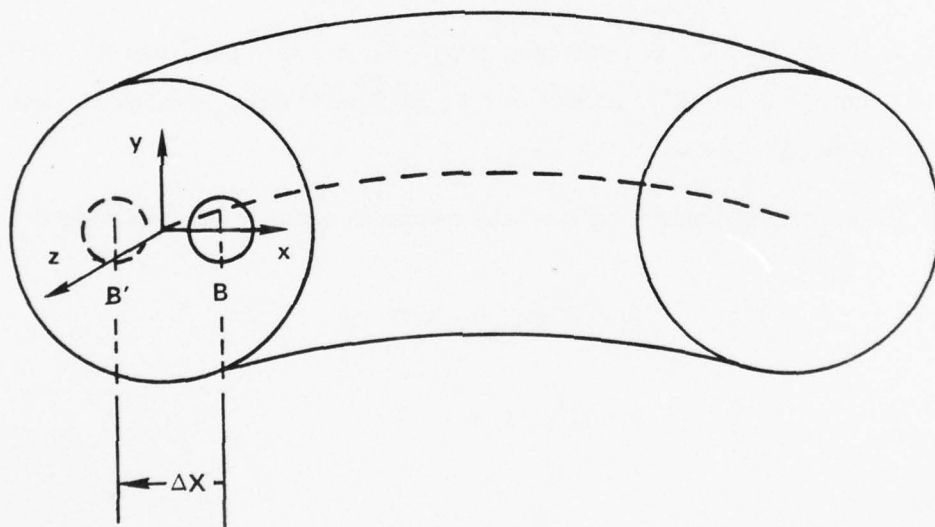[1] N. Rostoker, Particle Accelerators 5, 93 (1973).

92

Figure 7-26. Local Coordinates for a Torus.

This means that the beam is not centered in the torus but shifted to the position B a distance $2\gamma_o^2 V_z^2 / R\omega_p^2$ from the center. Similarly, it is evident that the effect of the vertical field B_y is to shift the center of the beam from B to B' by a displacement

$$\Delta x = -\frac{e}{c} V_z B_y \frac{2\gamma_o^2}{\omega_p^2} \frac{1}{m\gamma_o}$$

$$= -2\gamma_o^2 \left(\frac{V_z}{\omega_p}\right) \frac{\Omega_y}{\omega_p}$$

where $\Omega_y = eB_y / \gamma_o mc$. For example, if $\gamma_o = 21$, $n = 10^{13}$ cm^{-3} and $B_y = 300$ G, $\Delta x = 4.4$ cm. For the STP, we have $n \approx 4 \times 10^{11}$ cm^{-3} and $\gamma_o = 5$, which yields $B_y = 195$ G for $\Delta x = 4$ cm.

The x and y components of the orbit equations can be written as follows:

$$\ddot{x} = \Omega^2 x - \Omega_z \dot{y} + V_z \Omega_y (t)$$

$$\ddot{y} = \Omega^2 y + \Omega_z \dot{x}$$

where

$$\Omega^2 = \frac{\omega_p^2}{2\gamma_o^2} \quad, \quad \Omega_z = \frac{eB_z}{\gamma_o mc} \quad; \quad \Omega_y(t) = \frac{eB_y(t)}{\gamma_o mc} \quad.$$

In terms of the complex variable $\zeta = x + iy$ these equations can be combined to

$$\ddot{\zeta} - i\Omega_z \dot{\zeta} - \Omega^2 \zeta = V_z \Omega_y (t) \quad.$$

MICROCOPY RESOLUTION TEST CHART

NATIONAL BUREAU OF STANDARDS-1963-A
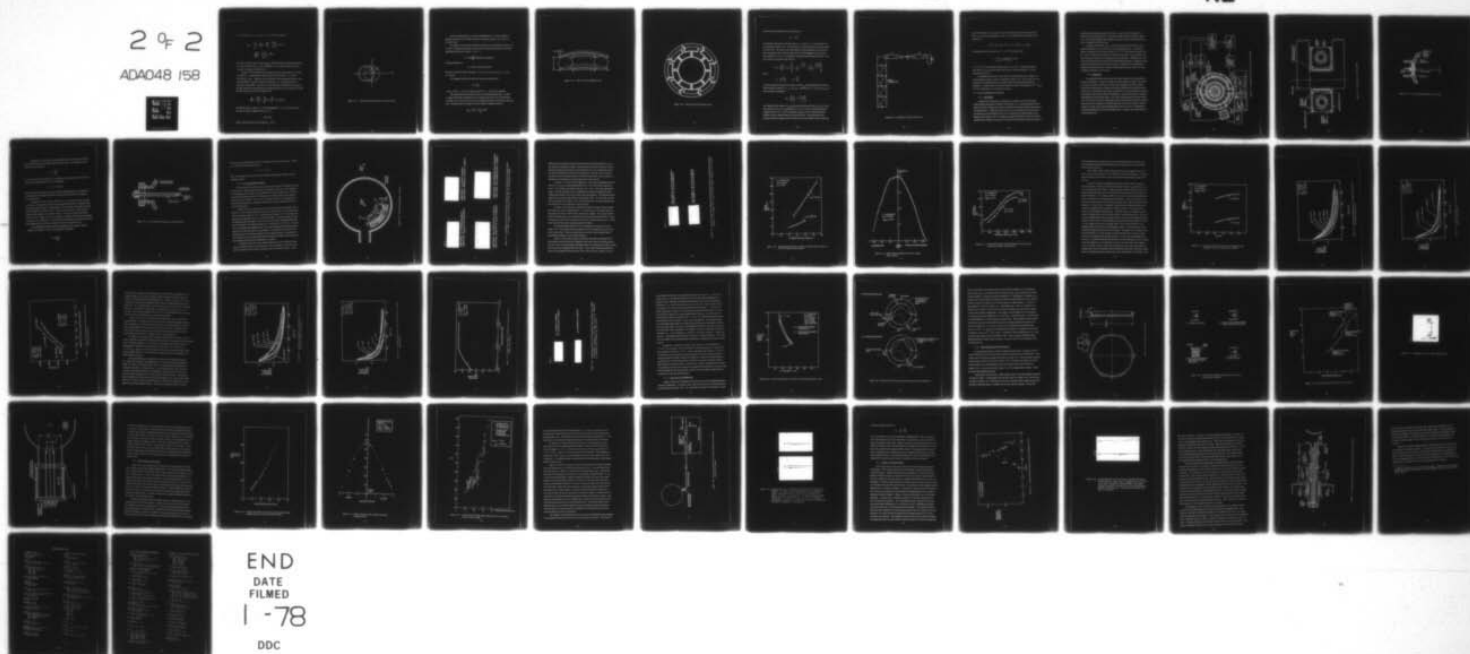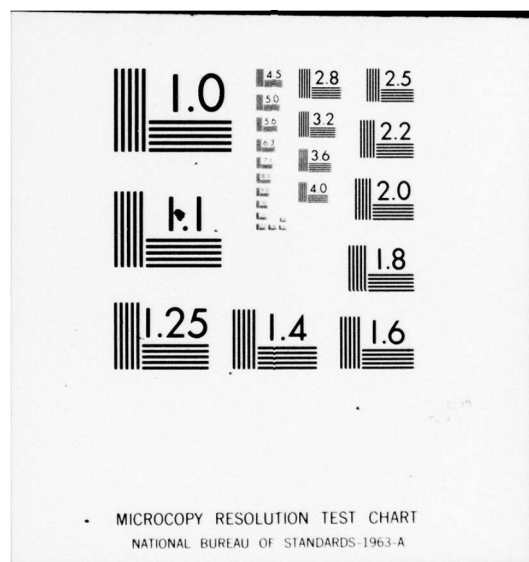
Assume that $B_y(t) = 0$, $t \leq 0$; $B_y(t) = B_y$, $t > 0$, then the solution is

$$\zeta(t) = \frac{-V_z \Omega_y}{\Omega^2} + \left(\zeta(0) - \frac{\dot{\zeta}(0)}{i\Omega_z} + \frac{V_z \Omega_y}{\Omega^2} \right) \exp i\,\omega_s t$$

$$+ \left(\frac{\dot{\zeta}(0)}{i\Omega_z} - \frac{V_z \Omega_y}{\Omega_z^2} \right) e^{i\Omega_z t} \ .$$

$\zeta(0)$, $\dot{\zeta}(0)$ are initial values for $\zeta(t)$ and $\omega_s = \Omega^2/\Omega_z$ is the slow precession frequency. It has been assumed that $\omega_s \ll \Omega_z$ or $\Omega^2/\Omega_z^2 \ll 1$. The orbital motion described by equation is illustrated in Figure 7-27.

The term $e^{i\Omega_z t}$ describes the fast precession at the gyrofrequency of the large toroidal field. The gyroradius of the precession is quite small. It is of order (velocity$/\Omega_z$) $< c/\Omega_z$. The term $\exp i\,\omega_s t$ describes a slow precession about a center that is shifted by $V_z \Omega_y /\Omega^2$ compared to the case $\Omega_y = 0$. This agrees with our expression for Δx above. However, it is now clear that the timescale for establishing this deflection is determined by the precession frequency ω_s; the speed with which the beam moves from B to B' in Figure 7-26.

$$\frac{\Delta x}{\Delta t} \cong \frac{V_z \Omega_y}{\Omega^2} \Big/ \frac{\Omega_z}{\Omega^2} \cong V_z \frac{\Omega_y}{\Omega_z} = V_z (B_y/B_z) \ .$$

We assume that $B_y = 300$ G, $B_z = 20$ kG so that $\Delta x/\Delta t = 4.5 \times 10^8$ cm/sec and the time for one beam to displace from B to B' is

$$\Delta t \cong 10 \text{ ns}$$

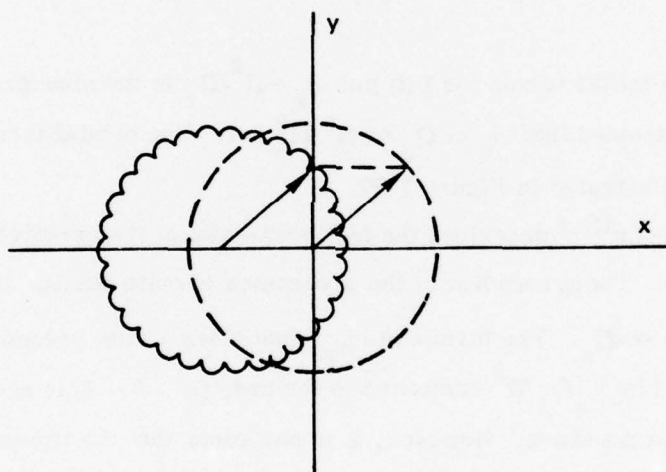which is also the result for STP where $B_z = 15$ kG.

95

Figure 7-27. Orbital Motion Produced by a Vertical Field B_y.

We have assumed that B_y is turned on instantaneously. In order to displace the beam in about 10 ns, it will be necessary to increase B_y from zero to 300 G in about this time.

We assume a set of toroidal windings to produce B_y as illustrated in Figure 7-28. In order to estimate the inductance of the coil we calculate the inductance/unit length neglecting the toroidal curvature. For w >> b

$$\ell \cong 8 \log \left(\frac{w}{b}\right) \text{ nanohenries/centimeter} \quad.$$

The total inductance is

$$L \cong 2\pi R \ell \cong 16 \pi R \, \log \, (w/b) \text{ nH}$$

where R is the major radius of the torus. For R = 50 cm, w = 30 cm, b = 1.5 cm, L = 7500 nH.

The magnetic field in the vicinity of the electron beam will be

$$B_y \cong \frac{4}{5} \frac{I}{w} \quad.$$

For B_y = 300 G, I = 11.25 kA, while in the STP, I = 7.3 kA will be required.

We assume that the coil will be driven by a high voltage pulse line. In order to reduce the effective inductance the coil would be split into N coils as illustrated in Figure 7-29. Each of the coils is to be connected in parallel and driven by the pulse line. The pulse line must supply a current NI and the magnetic energy is

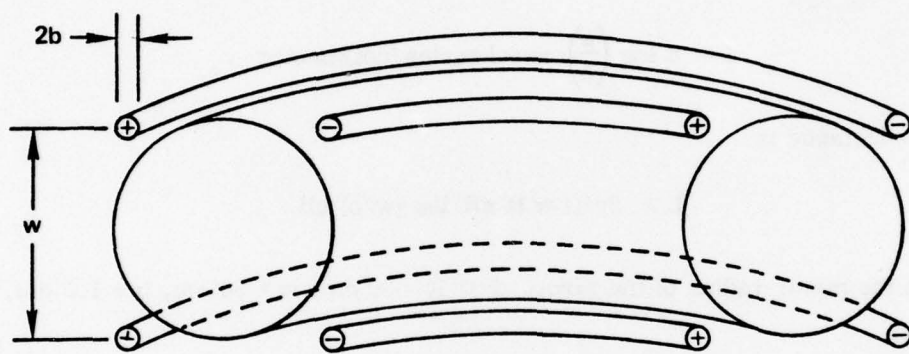$$W_M = \frac{1}{2} LI^2 = \frac{1}{2} \frac{L}{N^2} (NI)^2 \quad.$$

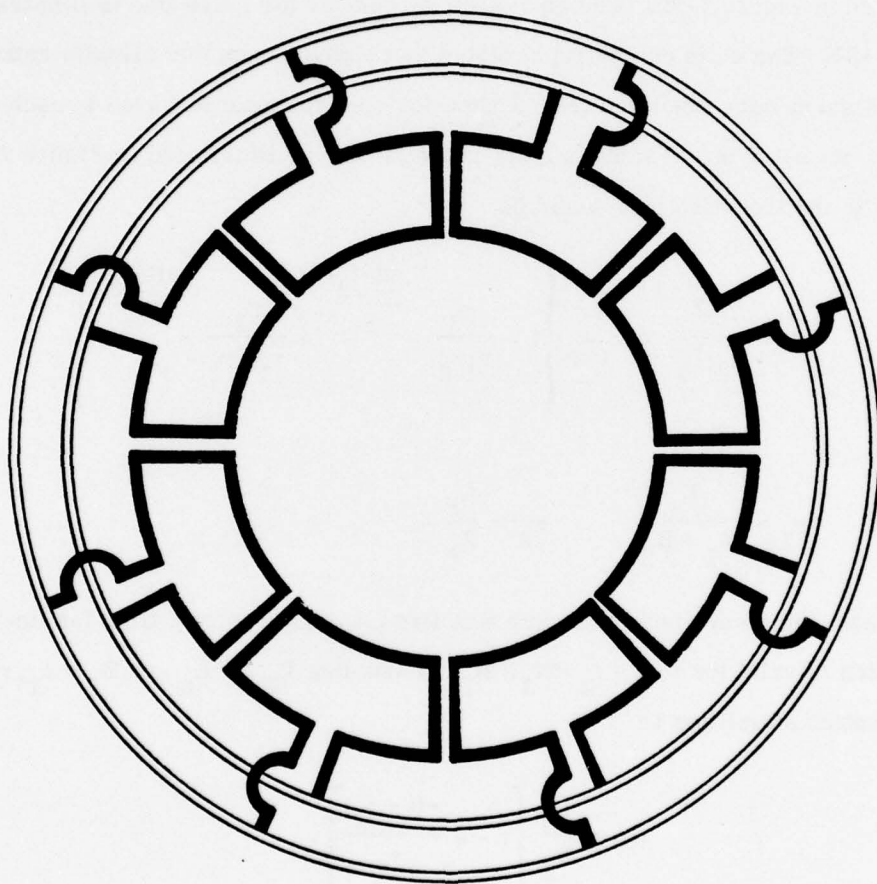Figure 7-28. Coils for Vertical Magnetic Field.

Figure 7-29. Split Coil and Coaxial Pulse Line.

Therefore the load inductance for the pulse line is

$$L_E = L/N^2 \ .$$

The effective inductance for the pulse line is L_E = 7500/64 = 117 nH assuming N = 8 as illustrated in Figure 7-29. The equivalent circuit for the pulse line is illustrated in Figure 7-30. The coils can be represented as lumped parameter circuits rather than transmission lines since the transit time for electromagnetic waves in each coil is $(2\pi R/8c) \cong 1.2$ ns. From analysis of the pulse line illustrated in Figure 7-30, the current in the inductive load would be

$$I(t) = \frac{2 Z_2}{L_E L_s} \ V \tau_1 \tau_2 \left\{ 1 - \frac{\tau_1}{\tau_1 \tau_2} e^{\frac{-(t-t_2)}{\tau_1}} + \frac{\tau_2}{\tau_1 - \tau_2} e^{\frac{-(t-t_2)}{\tau_2}} \right\}$$

where

$$\tau_1 = \frac{L_s}{Z_1 + Z_2} \qquad \tau_2 = \frac{L_E}{Z_2} \ .$$

Time is measured from when the switch S is fired; t_2 is the transit time for line Z_2. This equation is valid for $0 < t - t_2 < 2t_1$, $2t_2$. Assuming $L_E \gg L_s$ and $Z_1 \cong Z_2$, $\tau_2 \gg 1$ and the equation simplifies to

$$I(t) = \frac{V_o}{Z_2} \left[1 - e^{\frac{-(t - t_2)}{\tau_2}} \right].$$

The risetime of the current is L_E/Z_2 and since this must be about 10 ns, $Z_2 \cong 12\Omega$. The current rises to V_o/Z_2 which must be 8 × 11.25 = 90 kA so that the pulse line voltage is about 1 MV. In STP a pulse line voltage of 700 kV would be required. Clearly, this is a standard state-of-the-art pulse line. We assume that an oil dielectric would be employed and the radius of the outer cylinder would be about the
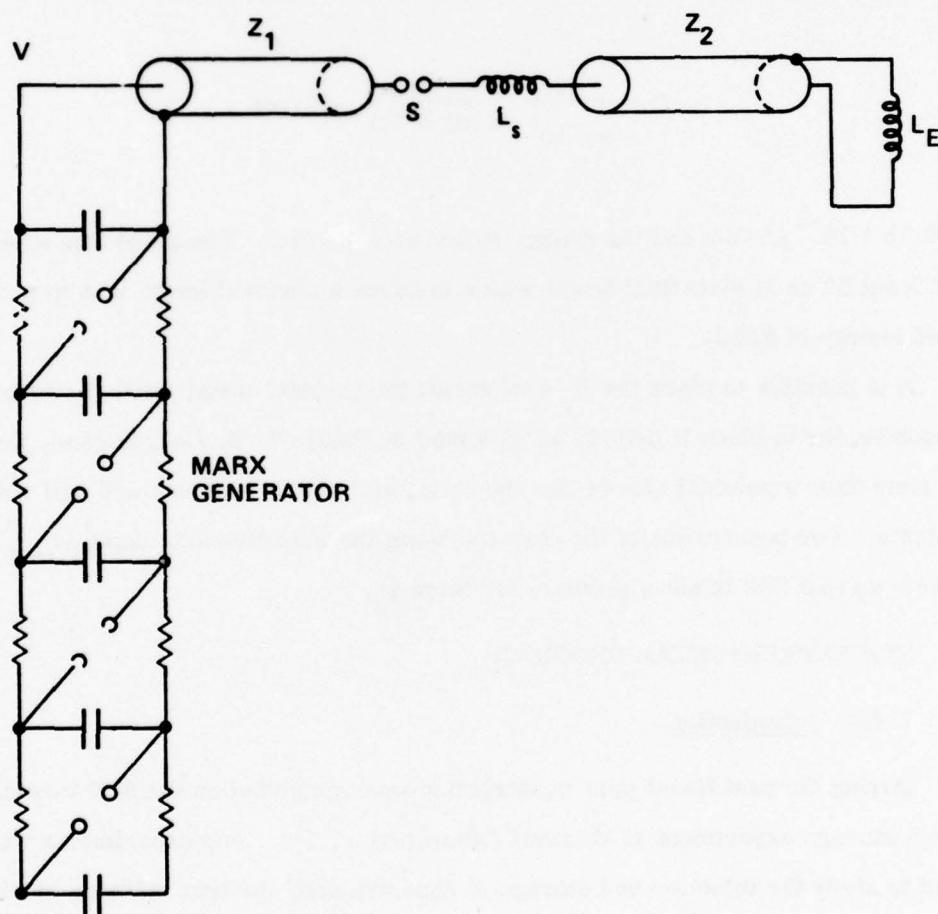
Figure 7-30. Equivalent Circuit of Pulse Line.

same as the torus, i.e. R_o = 50 cm, since Z = 60 log R_o/R_i the inside radius would be R_i = 41 cm to give an impedance of 12 Ω. The energy stored in the magnetic field of the coil is

$$\frac{1}{2} LI^2 = \frac{1}{2} \times 7500 \times 10^{-9} \times (11.25 \times 10^3)^2 = 474 \text{ Joules} \ .$$

The energy stored in the pulse line is $(1/2)$ CV^2/unit length where

$$C = \frac{1}{9 \times 10^5} \frac{1}{2 \log R_o/R_i} \ \mu F/cm \ .$$

$C = 0.28 \times 10^{-5} \mu F$/cm and the energy stored is 1.4 J/cm. The pulse line should be at least 20 ns in electrical length which involves a physical length of 6 m and a *stored energy* of 840 J.

It is possible to place the B_y-coil inside the toroidal metal wall. However, it is much easier to place it outside as indicated in Figure 7-28. In this case, the metal wall must have a poloidal slot or the magnetic field will be shielded and will not penetrate. For penetration of the electron beam the inductive skin depth is $\gamma_o^{3/2}$ (c/ω_p) = 17.5 cm so that this is not a problem for large γ_o.

7.2 STP EXPERIMENTAL PROGRAM

7.2.1 Introduction

During the past fiscal year construction was completed on the STP toroidal energy storage experiment at Maxwell Laboratories, Inc., and experiments were initiated to study the injection and storage of unneutralized electron columns and beams in toroidal geometry. During the course of the year, some modifications were made to the machine to correct magnetic field errors resulting from nonuniformities in the stainless steel vacuum vessel. In addition, during the latter part of the year vertical magnetic field windings were added to provide the vertical magnetic field necessary for

controlling the equilibrium position of the beam. A plan view of the machine as modified is shown in Figure 7-31, and a cross sectional drawing is shown in Figure 7-32. The vertical magnetic field windings are driven by a bank of marine batteries which is switched by an SCR circuit.

During the course of the year, a 40 kV thermionic electron injector was developed which injects ~ 100 μcoulombs of charge into the machine. This injected charge corresponds to an electron density of $\sim 10^{10}$ cm^{-3} and creates a potential well of ~ 300 kV. This amount of charge is sufficient to provide the E_r x B_ϕ particle rotational transform necessary for confining accelerated particles. Efforts near the end of the year have focused on acceleration of the injected charge into a relativistic beam. While these efforts have not yet been successful, we believe we have identified the problem area involved and have outlined an experimental program which will lead to significant relativistic beam currents.

7.2.2 Diagnostics

Two different kinds of probes have been used to measure the charge injected into the STP machine. Figure 7-33 shows one of these types of probes. This probe is called a wall probe and consists of a flat circular stainless steel disk mounted flush with the stainless steel vacuum vessel wall but electrically insulated from the vacuum wall. The stainless steel disk is connected to a 50 Ω cable and 50 Ω termination through a high vacuum electrical feedthrough. This probe provides two separate measurements of the injected charge. First, the probe measures the charge induced on the wall of the torus by the accumulation of the electron column inside the machine. Since the probe is connected to ground through 50 Ω, the induced charge on the disk produces a voltage across the termination when it flows to ground. Integrating the voltage appearing across the 50 Ω termination gives a measure of the total charge injected into the torus.
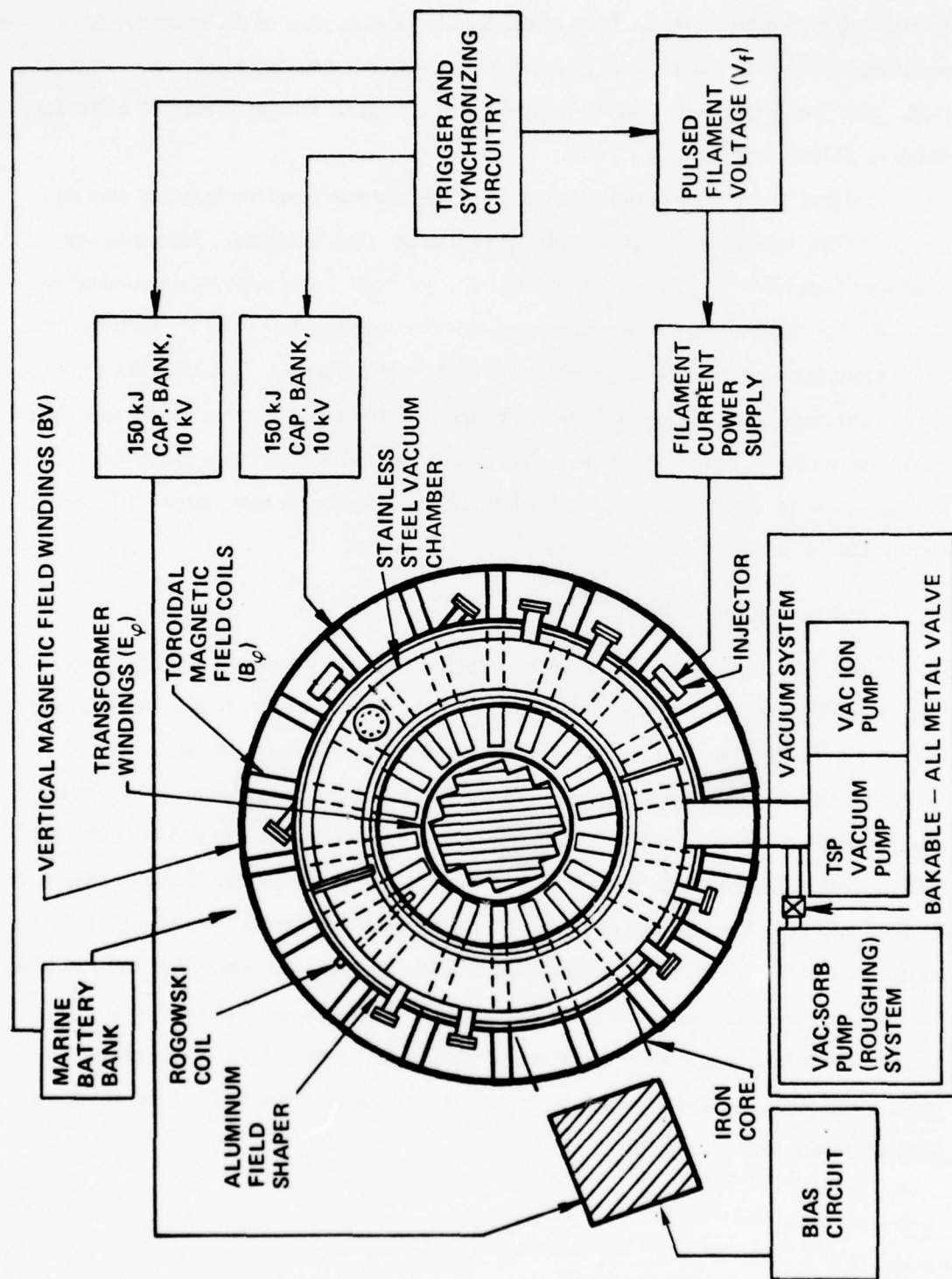
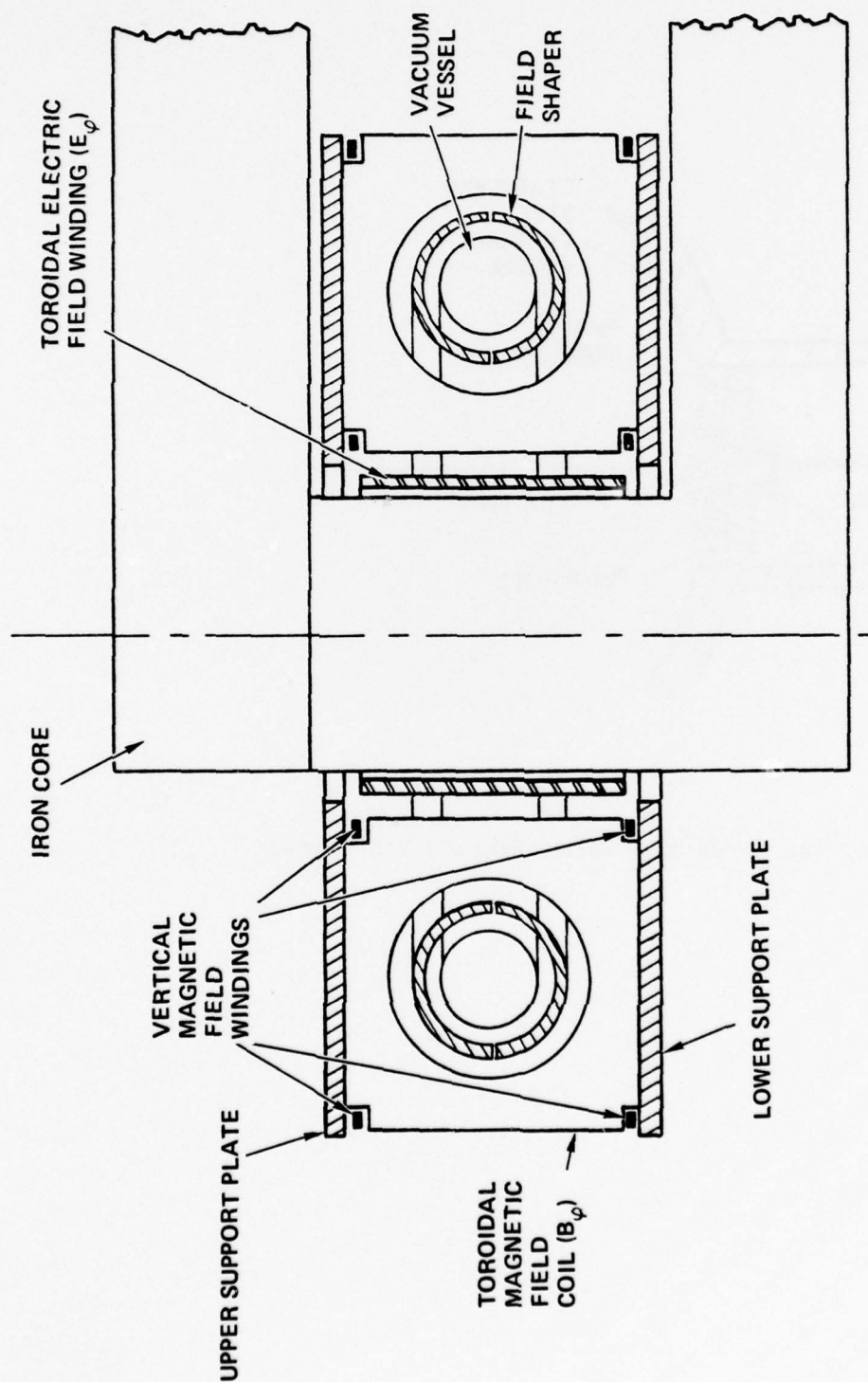Figure 7-31. Operational Layout for the DNA-STP Machine.

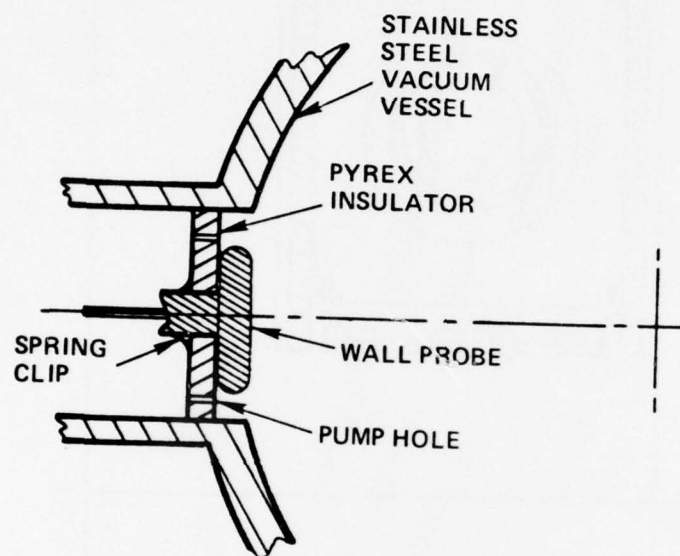Figure 7-32. Cross Section of the STP Machine.

Figure 7-33. Cross-Sectional Drawing of a Wall Probe.

In addition, the wall probes couple capacitively to the diocotron surface flute modes which can exist in an unneutralized electron column. The frequency of the diocotron mode is given by

$$\omega_d = \frac{\omega_p^2}{2\omega_c} .$$

As a result, the electron density may be determined by measuring the diocotron frequency if the magnetic field is known. Specifically,

$$n = 6.9 \times 10^8 \, f_d B$$

where the diocotron frequency f_d is in Hz and the magnetic field B is in Webers/m^2. For most of the experiments described, wall probes were placed at two different toroidal locations.

Another probe used is shown in Figure 7-34. This probe consists of a glass tube with a .020" diameter tungsten wire protruding from the end. The probe which is movable radially through a vacuum fitting is used to measure the depth and profile of the potential well created by the non-neutral charge collection. This provides a measure of the density in the electron column. The probe is connected through a 10 MΩ to 10 kΩ voltage divider to an operational amplifier which drives a terminated 50Ω cable to an oscilloscope. For most of the measurements described in this report, the potential probe was located toroidally 180° from the injection sector.

Assuming that the electron density distribution in the electron column is uniform, the density is related to the potential well depth by
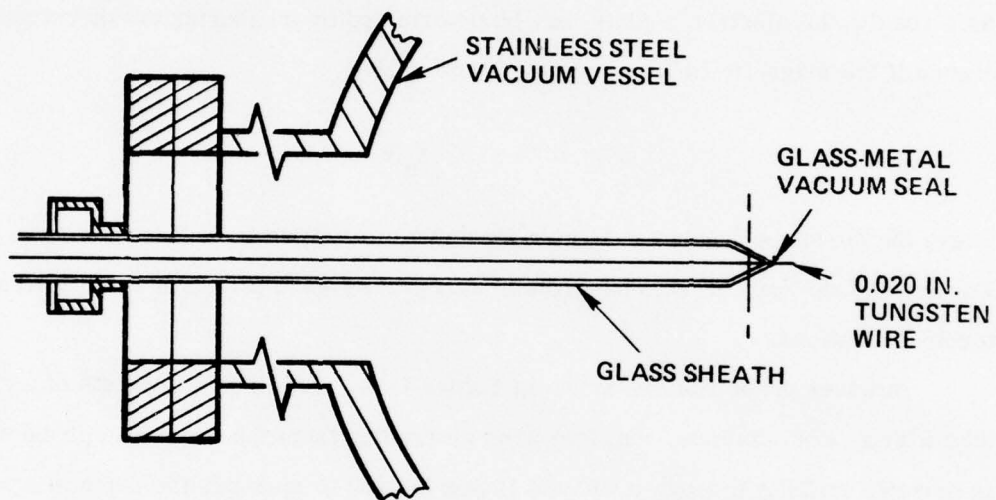
$$V_o = \frac{neb^2}{4\epsilon_o} ,$$

Figure 7-34. Cross-Sectional Drawing of a Potential Probe.

where V_o is the potential at the center of the column and b is the beam radius. Taking b = 8 cm (the vacuum wall radius) gives

$$n = 3.45 \times 10^4 V_o.$$

Thus, the potential probe provides a third method of measuring the electron density inside the column.

7.2.3 Low Voltage Injector Studies

The first injector assembly used to inject charge into the STP machine is shown in Figure 7-35. This injector consisted of 12 thoriated, carburized, .024" diameter, 4" long filament wires located in one quadrant of the minor circumference. Molybendum plates are placed parallel to the filament wires and the filament bias voltage is applied across the plates. This results in an electric field which is perpendicular to the toroidal magnetic field, causing the electrons to acquire an ExB drift velocity toward the minor axis.

Figure 7-36 shows oscilloscope traces of machine operation using this kind of injector. For this shot the magnetic field had a risetime of 2 msec, reaching a maximum (at the minor axis) of 4.7 kG. An injector bias voltage of 4.0 kV was used, and injection was begun after 1.8 msec. The bias voltage was crowbarred after 200 μsec terminating the injection phase. The lower trace in the upper right hand photograph shows the potential well depth time history at a sensitivity of 10.7 kV/div. As can be seen, the potential well depth builds to a maximum during injection and then begins to decay after the injection process is terminated. The upper trace in the lower left photograph shows the wall probe signal gives the injected charge ($\sim$8 μcoulombs for this shot) which is in good agreement with the potential well depth measurement if an approximately uniform charge distribution is assumed.

The bottom trace in the lower right photograph shows the diocotron oscillations on a fast time sweep (1 μsec/division). These oscillations occur late in time when the potential probe is located near the center of the electron column. (This
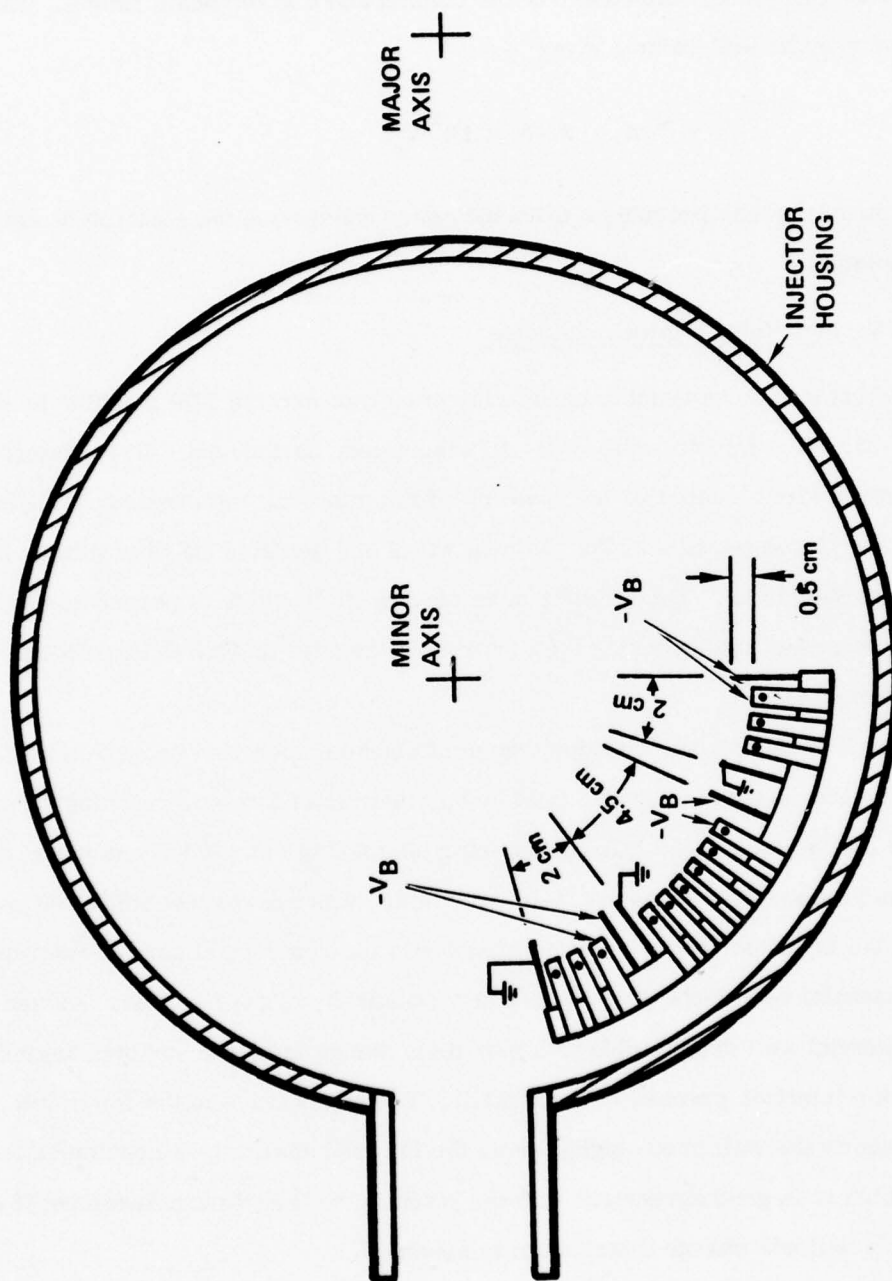
109

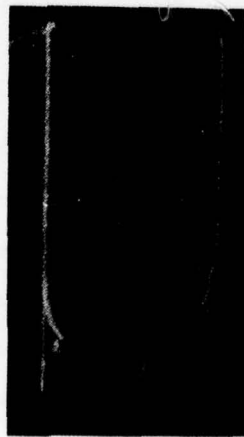Figure 7-35. Linear Electron Injector – End View.

110

UPPER TRACE: I_{inj}, 10 A/DIV, 1 mSEC/DIV
LOWER TRACE: POTENTIAL, 10.7 kV/DIV, 1 mSEC/DIV

UPPER TRACE: WALL PROBE, 50 mV/DIV, 200 μSEC/DIV
LOWER TRACE: WALL PROBE, 50 mV/DIV, 1 μSEC/DIV

UPPER TRACE: B_{φ}, 3.2 kG/DIV, 500 μSEC/DIV
LOWER TRACE: V_{BIAS}, 4.0 kV/DIV, 500 μSEC/DIV

UPPER TRACE: WALL PROBE, 5 mV/DIV, 20 μSEC/DIV
LOWER TRACE: POTENTIAL, 10.7 kV/DIV, 20 μSEC/DIV

Figure 7-36. Oscillograph Traces of STP Machine Operation Using Low Voltage Linear Charge Injector.
$T/4 = 2$ msec, B_{φ} max $= 4.7$ kG, $V_{bias} = 4.0$ kV $t_{inj} = 1.8$ msec, $\Delta t_{CB} = 200$ μsec.

E-153

111

indicates that the potential probe perturbs the electron column sufficiently to cause the diocotron oscillations to begin). Measurements of the electron density from the diocotron frequency give values of electron density which are somewhat lower than the densities obtained from the probe measurements. However, this is probably reasonable since the diocotron waves are surface modes and the electron density is undoubtedly somewhat lower near the edge of the electron column.

In Figure 7-37 we show probe signals for a case where the magnetic field rise time was 3.5 msec, the peak magnetic field was 5.8 kG, and the bias voltage was 5.0 kV. The potential well depth in this case was ~ 30 kV. The lower two traces in Figure 7-37 show diocotron wave oscillations taken with two different wall probes located approximately 90° apart toroidally around the machine. The diocotron modes should have zero phase shift parallel to the magnetic field. As can be seen, the two wall probe signals are in phase. These measurements thus provide verification that the observed waves are indeed the diocotron modes.

In Figure 7-38 we show the variation of potential well depth with the injector bias voltage for the low voltage injector. As can be seen, the well depth (and hence the charge) was found to scale linearly with the bias voltage. This scaling indicates that the injected charge can be significantly increased by increasing the bias voltage. Advantage was taken of this scaling later in the year to obtain an increase of ~10 fold in the injected charge and resulting potential well depth.

The radial potential profile for the low voltage linear injector is shown in Figure 7-39. The profile can be reasonably well fit by a parabolic curve over much of the minor radius. This is consistent with an electron column density which is approximately uniform over the column diameter.

Figure 7-40 shows the variation in potential well depth as a function of the time delay between the start of the magnetic field and the start of the injection phase As can be seen, the peak potential well depth attained is maximum late in time for both the 3.5 and 2 msec magnetic field rise times. More recent results with another injector of only slightly different geometry do not show this same variation, however.
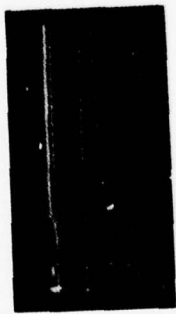
WALL PROBE #2: 50 mV/DIV, 200 μSEC/DIV
POTENTIAL: 10.7 kV/DIV, 200 μSEC/DIV

WALL PROBE #1: 50 mV/DIV, 0.5 μSEC/DIV
WALL PROBE #2: 50 mV/DIV, 0.5 μSEC/DIV

E-154

Figure 7-37. Diocotron Wave and Potential Probe Measurements Using Low Voltage Linear Injector. $B_{\phi max}$ = 5.3 kG, V_{bias} = 5.0 kV, t_{inj} = 2.2 msec, Δt_{CB} = 100 μsec, T/4 = 3.5 msec.
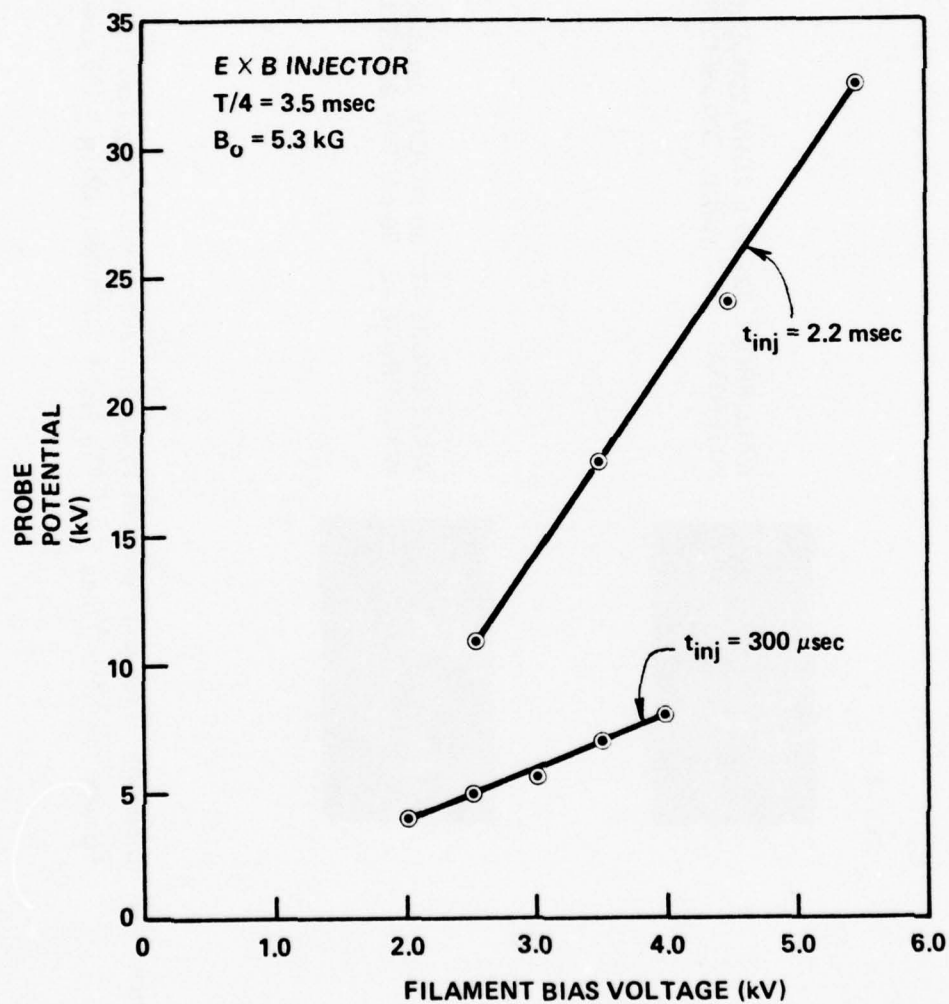
113

Figure 7-38. Potential Well Depth as a Function of Injector Bias Voltage for the Low Voltage, Linear Injector.
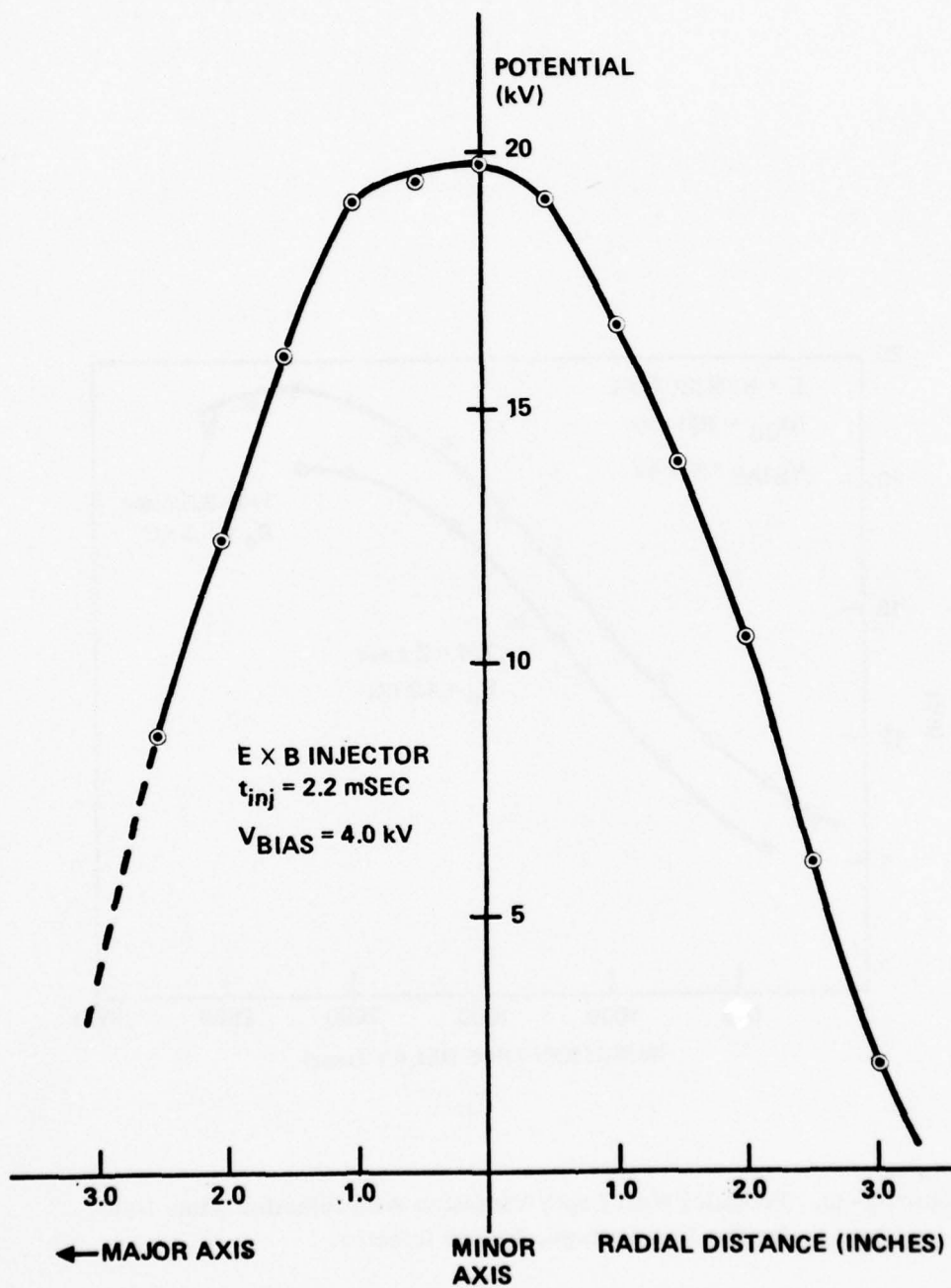
Figure 7-39. Radial Potential Profile for the Low Voltage,
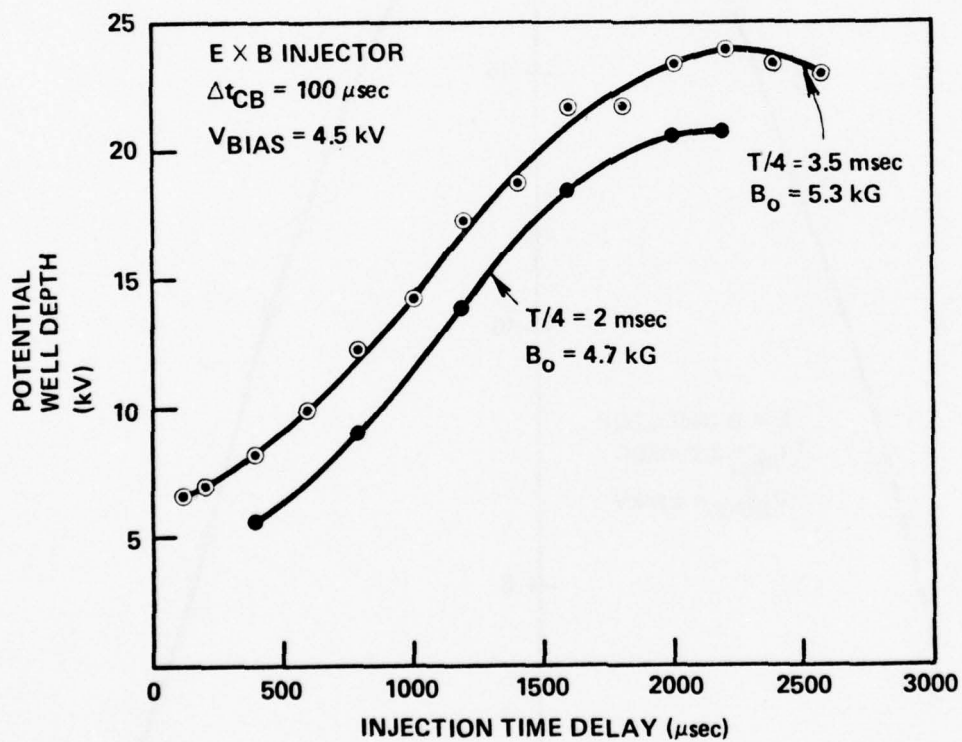Linear Injector.

115

Figure 7-40. Potential Well Depth Variation With Injection Time Delay for the Low Voltage, Linear Injector.

This indicates that this behavior may be due to magnetic field errors (due to magnetic field penetration through the stainless vacuum liner) which were accentuated by this injector geometry.

The variation of the potential well depth with the peak magnetic field at the minor axis is shown in Figure 7-41 for both early and late time injection. The potential well depth was observed to be only a weak function of the magnetic field for this injector.

In order to study the containment time of the electron column, provisions have been made to crowbar the injection voltage after a time Δt_{cb} which can be set by an external time delay control. After the injection voltage has been removed, the electron density begins to decay, and this decay has been observed for a number of different conditions. For example, Figure 7-42 shows the variation of the potential decay as a function of the peak magnetic field strength. Each curve in Figure 7-42 has been normalized to its own peak value so that the decay rates can be more easily compared. As can be seen, a systematic improvement in containment time occurs as the peak magnetic field is increased. Similarly, Figure 7-43 shows the decay rate for several different injection times. This figure shows a systematic improvement in containment time as the injection window is moved to later times. However, since the magnetic field during the decay time also increases as the injection window is moved to later times, it is interesting to compare the data from Figures 7-42 and 7-43 on a single plot in terms of magnetic field. This is done in Figure 7-44 by plotting the decay time (time for the potential to decay to $1/e$ times the peak value) against the magnetic field at the start of injection. The upper curve is obtained from the data of Figure 7-43 where the time at which injection starts is varied, and the lower curve is obtained from the data of Figure 7-42 where the peak magnetic field is varied. A primary difference between the two curves is that upper curve was taken with a bias voltage of 4.0 kV while the lower curve was taken with a bias voltage of 5.0 kV. However, the two curves have very nearly the same slope, and should essentially lay on top of one another if they had both been taken at the same bias voltage. There is a departure from this trend at very early injection times on the upper curve.
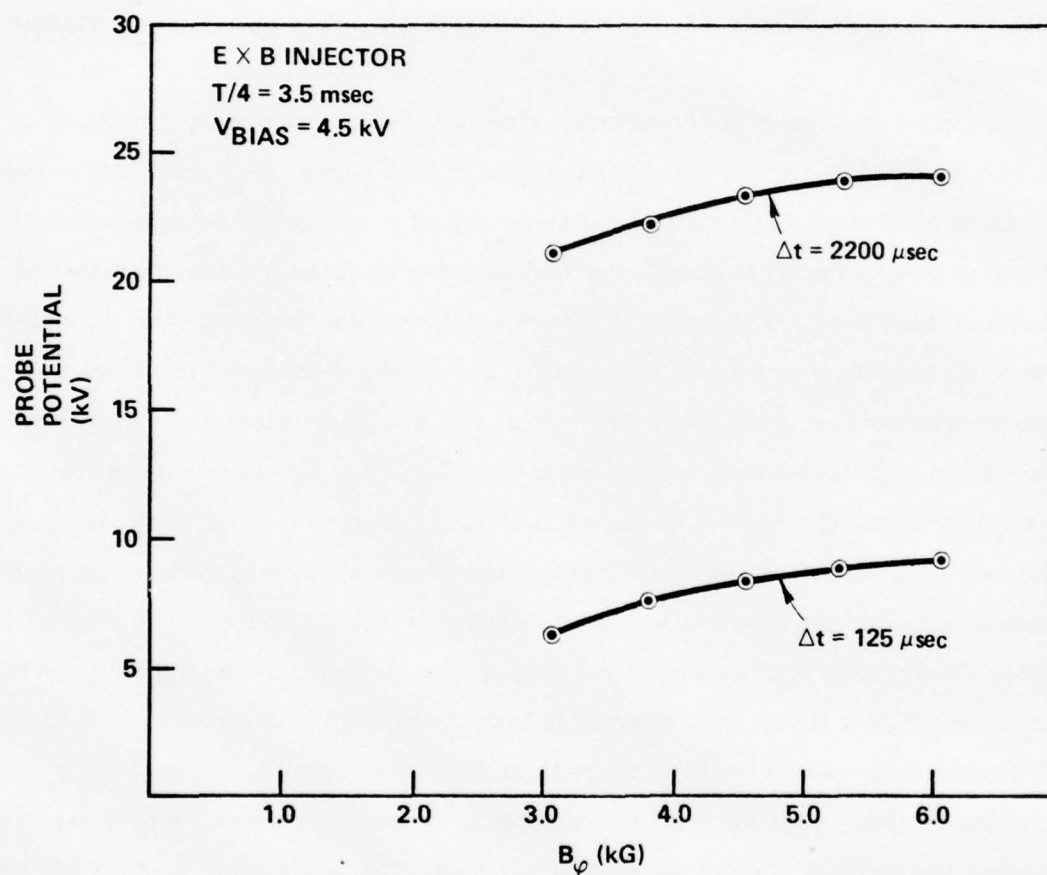
117

Figure 7-41. Variation of Potential Well Depth with Magnetic Field
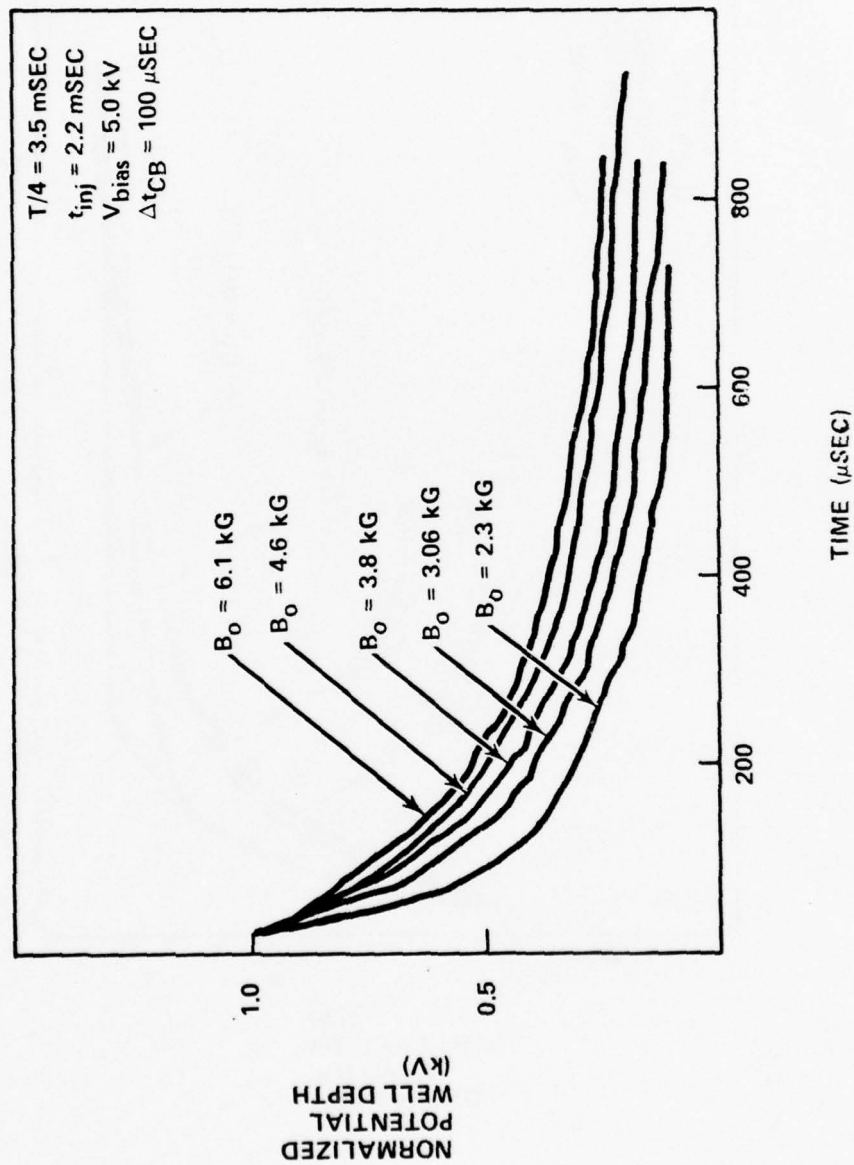Strength for the Low Voltage, Linear Injector.

Figure 7-42. Variation of Potential Decay with Magnetic Field for the Low Voltage, Linear Injector.
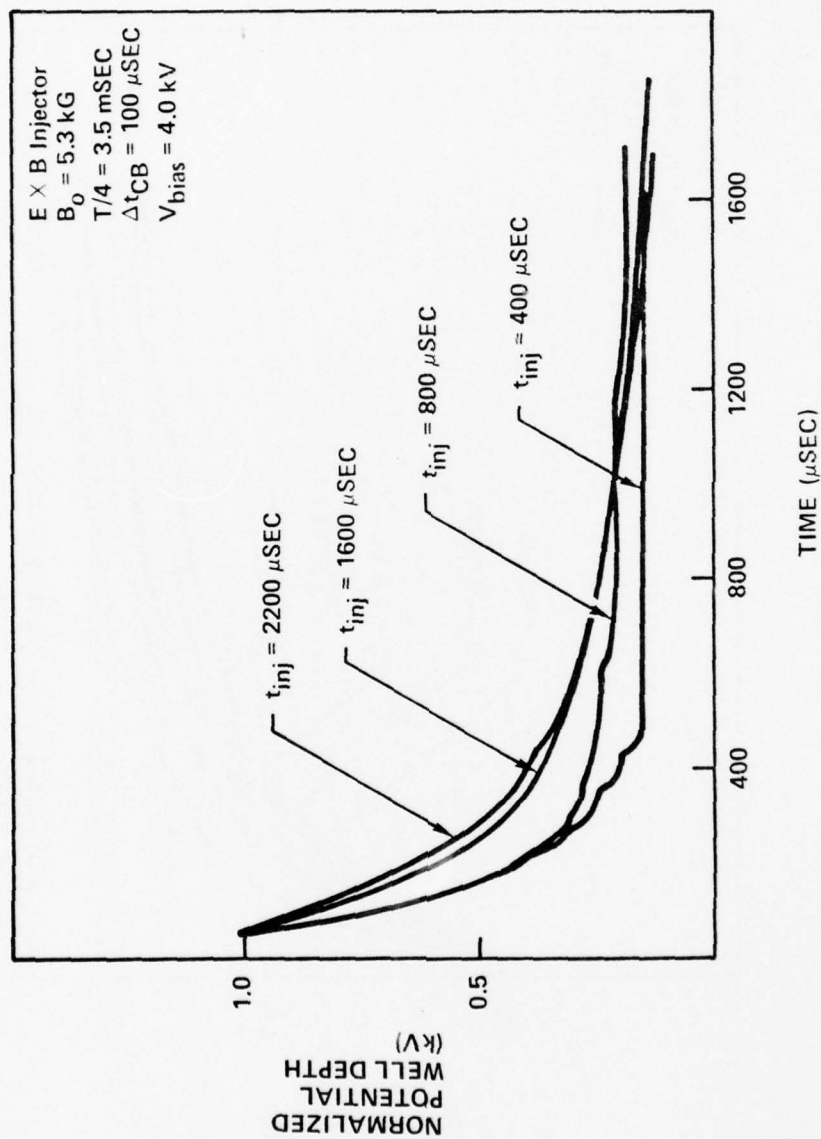
119

Figure 7-43. Variation of Potential Decay with Injection Time for the Low Voltage, Linear Injector.
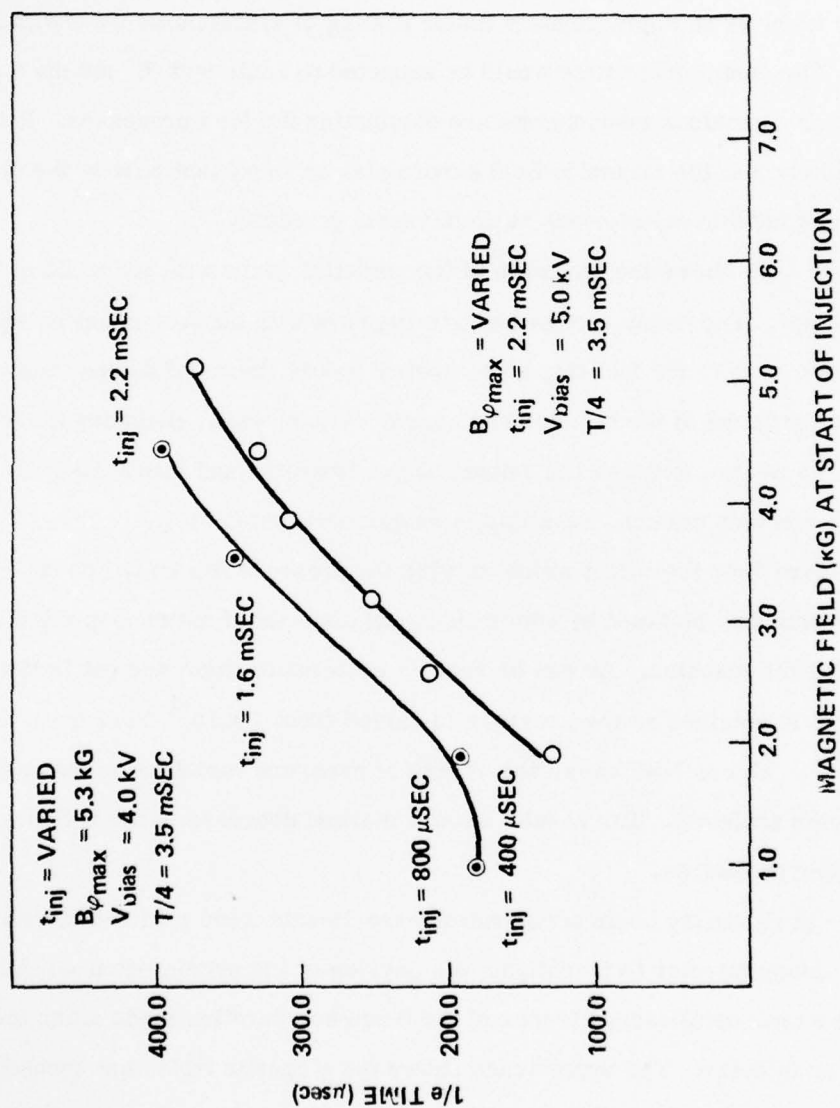
120

Figure 7-44. Decay Time Variation with Magnetic Field for the Low Voltage, Linear Injector.

121

However, this is probably at least partially due to the fact that the magnetic field is changing rapidly early in time so that the average magnetic field during the decay period is somewhat higher than the plotted points. The data of Figure 7-44 is interesting since it shows an approximately linear scaling of containment time with magnetic field. The containment time would be expected to scale with B^2 unless magnetic field errors or anomalous mechanisms are dominating the loss processes. It is, therefore, likely that the magnetic field errors play an important part in the electron loss processes for this injector and vacuum vessel geometry.

Figure 7-45 shows the variation of the potential decay with the width of the injection window. The decay rate is found to improve with shorter injection windows. This is probably due to the fact that some neutral gas is liberated during injection by electron bombardment of the injector and nearby vacuum wall. Reducing the width of the injection window reduces the amount of gas liberated and hence the ion component in the electron column, resulting in longer containment time.

In Figure 7-46 the effect which varying the pressure has on the decay rate are shown. This data was obtained by admitting small amounts of methane gas into the chamber prior to firing the machine. As can be seen, a systematic improvement in the containment time is obtained as the pressure is varied from 1×10^{-6} Torr down to 8×10^{-9} Torr. Figure 7-47 shows the effects of pressure variation on the peak potential well depths achieved. The results show a marked decrease in the potential well depth at higher pressures.

Some preliminary beam acceleration experiments were performed with the low voltage linear injector to investigate the physics of the acceleration mechanism. Figure 7-48 shows oscilloscope traces of the beam acceleration mode using the low voltage linear injector. The upper trace shows the magnetic field, the second trace shows the accelerating electric field, and the lower trace shows the beam current measured with a Rogowski loop on a sweep speed of 20 μsec/division. The injection phase was started 2.2 msec after the start of the magnetic field. The injection window width was ~100 μsec, and the acceleration phase was begun at 2300 μsec which corresponds to the end of the injection window. The beam current pulse width of ~30 μsec
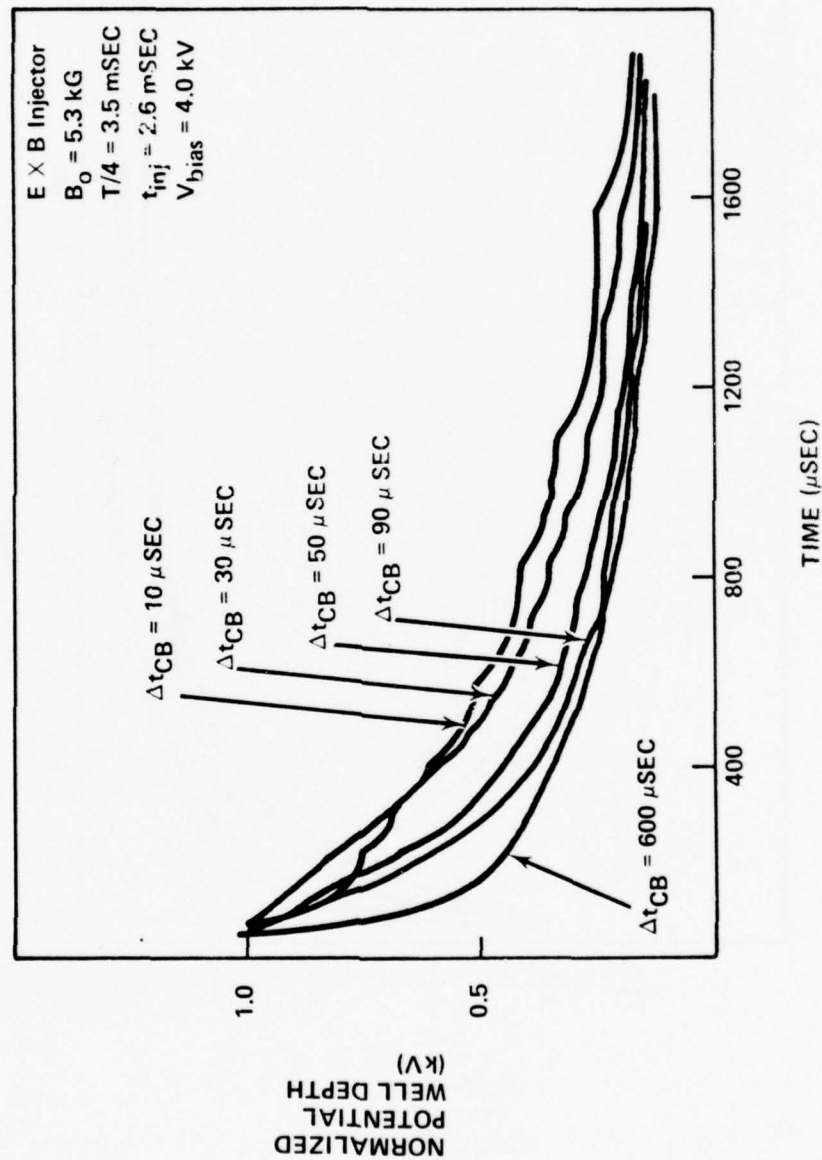
122

Figure 7-45. Variation of Potential Decay with Injection Crowbar Time - for the Low Voltage, Linear Injector.
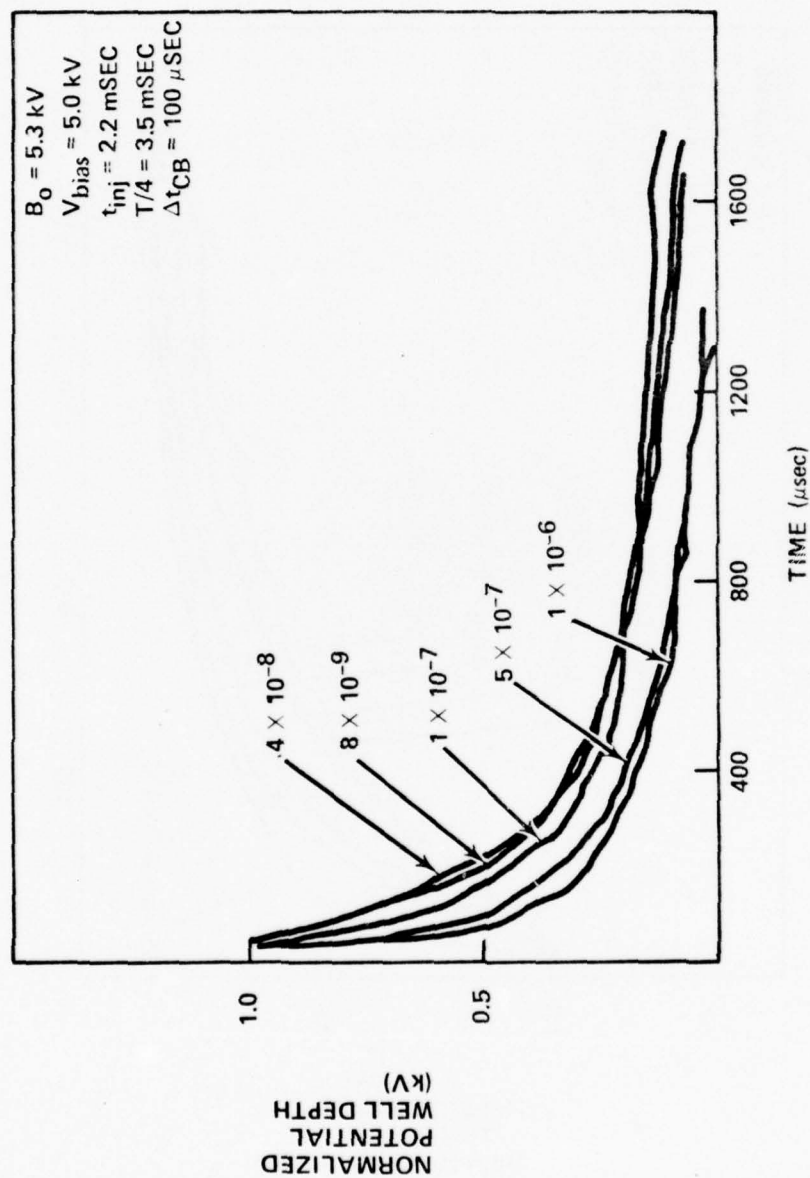
123

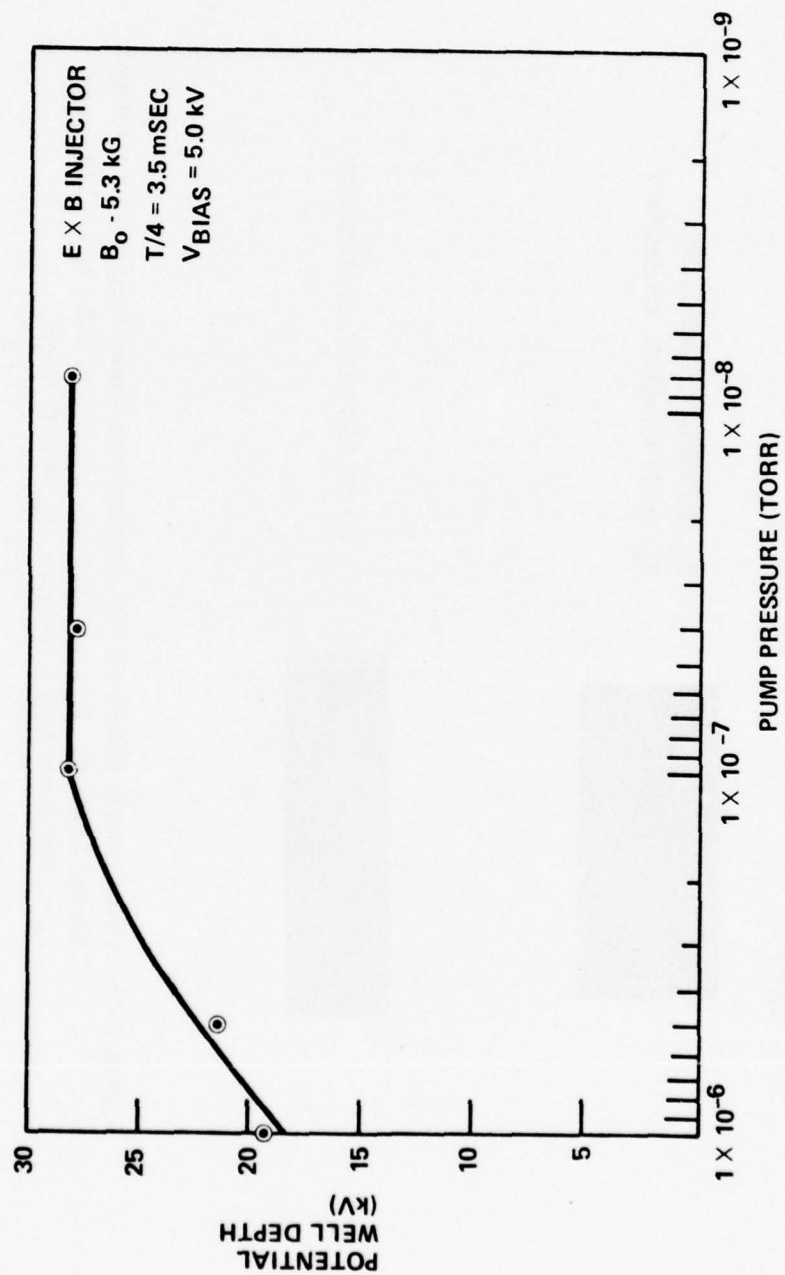Figure 7-46. Variation of Decay Rate with Pressure for the Low Voltage, Linear Injector.

Figure 7-47. Potential Well Depth as a Function of Pressure for the Low Voltage, Linear Injector.

125

B_φ: 3.2 kG/DIV, 1 mSEC/DIV
E_φ: 0.127 V/cm/DIV, 1 mSEC/DIV

I_B: 88 AMPS/DIV, 20 μSEC/DIV

E-155

Figure 7-48. Oscilloscope Traces of STP Acceleration Mode Using the Low Voltage, Linear Injector. $B_\varphi max = 5.3$ kG, $V_{bias} = 5.5$ kV, $t_{inj} = 2200\ \mu$sec, $t_A = 2300\ \mu$sec, $t_{CB} = 100\ \mu$sec, $E_\varphi = 0.15$ V/cm.

126

is consistent with the time to accelerate the electrons from rest to $\gamma \sim 1.05$ to 1.06. At this value of γ the electron drift to the wall due to the toroidal magnetic field gradient is more rapid than the precession around the minor axis which cancels the drift effects. As a result, the electrons are lost to the wall. That is, more charge is required to provide the rotational transform needed for higher γ. This point is further illustrated in Figure 7-49 which shows the theoretical and measured current pulse width as a function of the accelerating electric field E_ϕ. As can be seen, the current pulse widths are consistent with $\gamma \sim 1.05$ to 1.06. This agrees with theoretical predictions of the maximum γ which can be supported by ~ 12 μcoulomb charge. The accelerated beam appears to be stable and well behaved for the duration of the 20 to 30 μsec pulse width. However, the peak amplitude of the current pulse is considerably lower than would be expected. For example, a total of 12 μcoulombs of charge accelerated to $\gamma \sim 1.05$ corresponds to a current of ~ 350 amps, and only ~ 50 amps was observed. This indicates that only part of the charge is being accelerated. This could be due to magnetic field inhomogenieties resulting in the trapping of the charge in local mirrors.

In summary, using the low voltage, linear injector, electron densities of $\sim 10^9$ cm^{-3} were achieved. This corresponds to an injected charge of ~ 12 μcoulombs and a potential well depth of ~ 33 kV. Charge containment times (time to $1/e$) of several hundred μsec were observed, and preliminary beam acceleration experiments showed current pulse widths in agreement with theory, but beam currents which were anomalously low. The injected charge was found to scale linearly with the injector bias voltage for the linear injector. Based on these results, modifications were made to the toroidal vacuum vessel to improve the magnetic field uniformity, and at the same time modifications were incorporated to allow for the use of higher voltage injectors in order to increase the injected charge.

7.2.4 Vacuum Vessel Modifications

Figure 7-50 shows a comparison of the STP vacuum vessel configuration before and after modification. For clarity, some of the ports not involved in the modification have been left off of Figure 7-50. The modification consisted of removing the ceramic
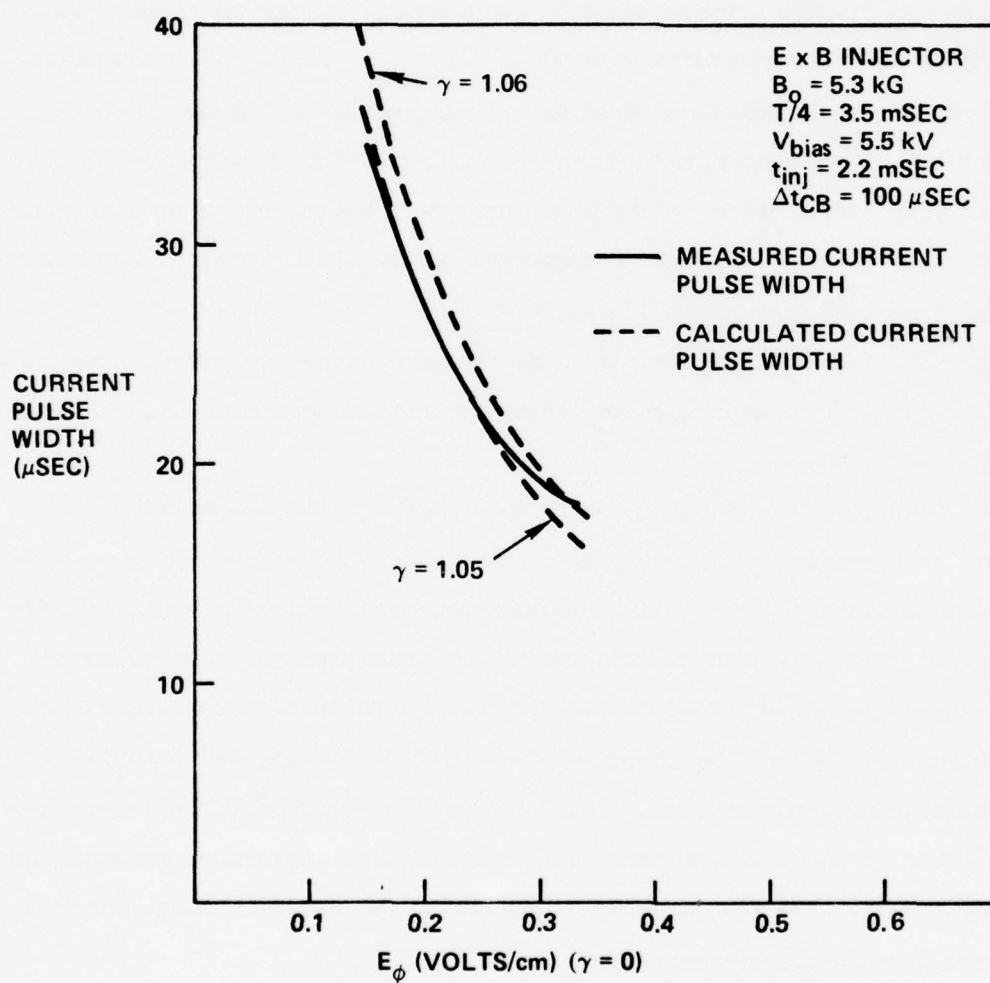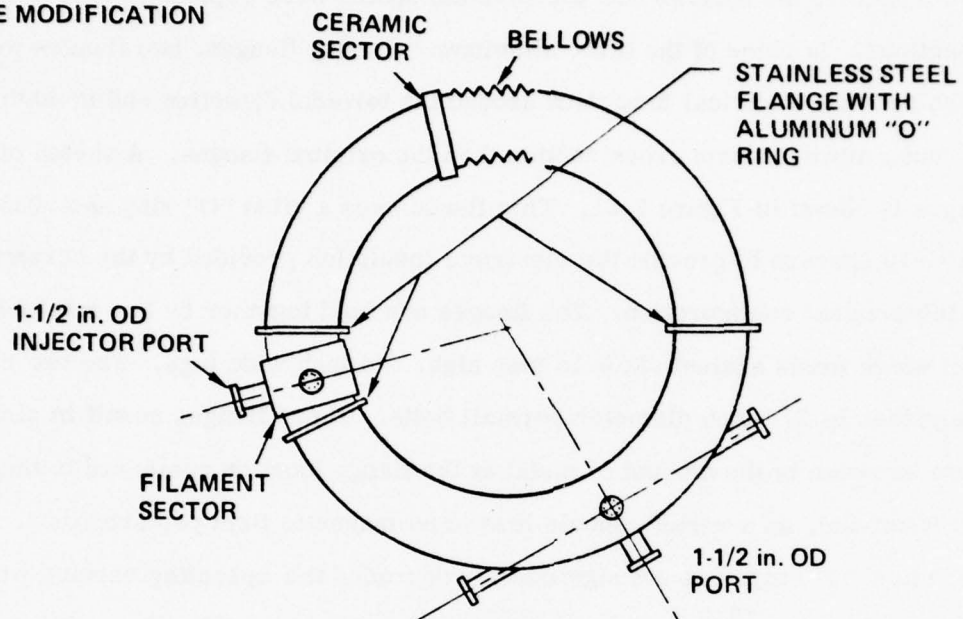
127

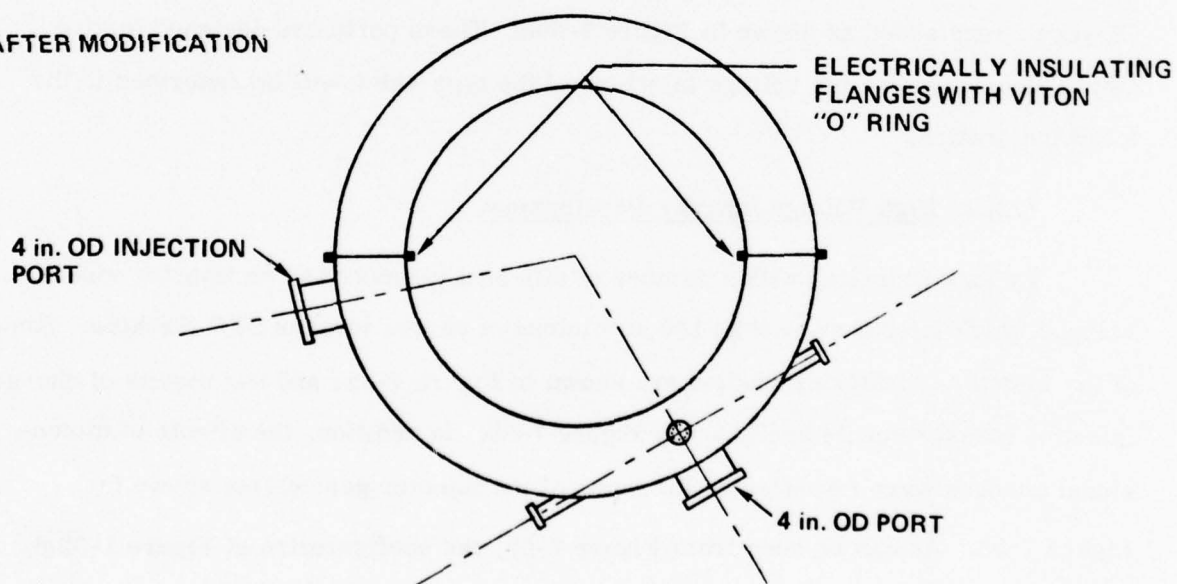Figure 7-49. Current Pulse Width as a Function of Accelerating Electric Field.

128

Figure 7-50. Sketch of STP Vacuum Vessel Features Involved in Modification.

129

sector, the bellows, the filament sector, and the three aluminum "O" ring flanges. The ceramic sector, the bellows and the filament sector were replaced with smooth toroidal sections. In place of the three aluminum "O" ring flanges, two flanges were added which provide electrical insulation around the toroidal direction and in addition provide a much more uniform cross section than the original flanges. A sketch of these flanges is shown in Figure 7-51. This flange uses a viton "O" ring and .035 inch thick G-10 spacers to provide the electrical insulation provided by the ceramic sector in the original configuration. The flanges are held together by two rotatable G-10 rings which press against six 0.15 inch high, 3/4 inch wide lugs. The two rings are held together by 3/8 inch diameter permali bolts. These flanges result in almost no effective increase in the amount of metal at the flange location compared to the torus wall itself and, as a result, should lead to no magnetic field perturbations. The use of viton "O" rings has not significantly degraded the operating vacuum which is typically in the low 10^{-9} Torr range. In addition to these modifications, two 4 inch OD ports were added as shown in Figure 7-50b. These ports are designed to give ample clearance for high voltage injectors of the type which will be described in the following section.

7.2.5 High Voltage Injector Development

By experimenting with a number of different geometries, an injector was developed which injects more than 100 μcoulombs of charge into the STP machine. Some of the injector geometries studied are shown in Figure 7-52, and the results of charge injection measurements are given in Figure 7-53. In addition, the effects of dimensional changes were investigated for some of the injector geometries shown in Figure 7-52. As can be seen from Figure 7-53, the configuration of Figure 7-52(d) gave the largest injected charge.

On the basis of these tests, a high voltage injector was built using the geometry on Figure 7-52(d). A photograph of this device is shown in Figure 7-54, and a sketch is shown in Figure 7-55. This device uses a four conductor high voltage vacuum feed through to bring the injector voltages and currents into the machine. These feed
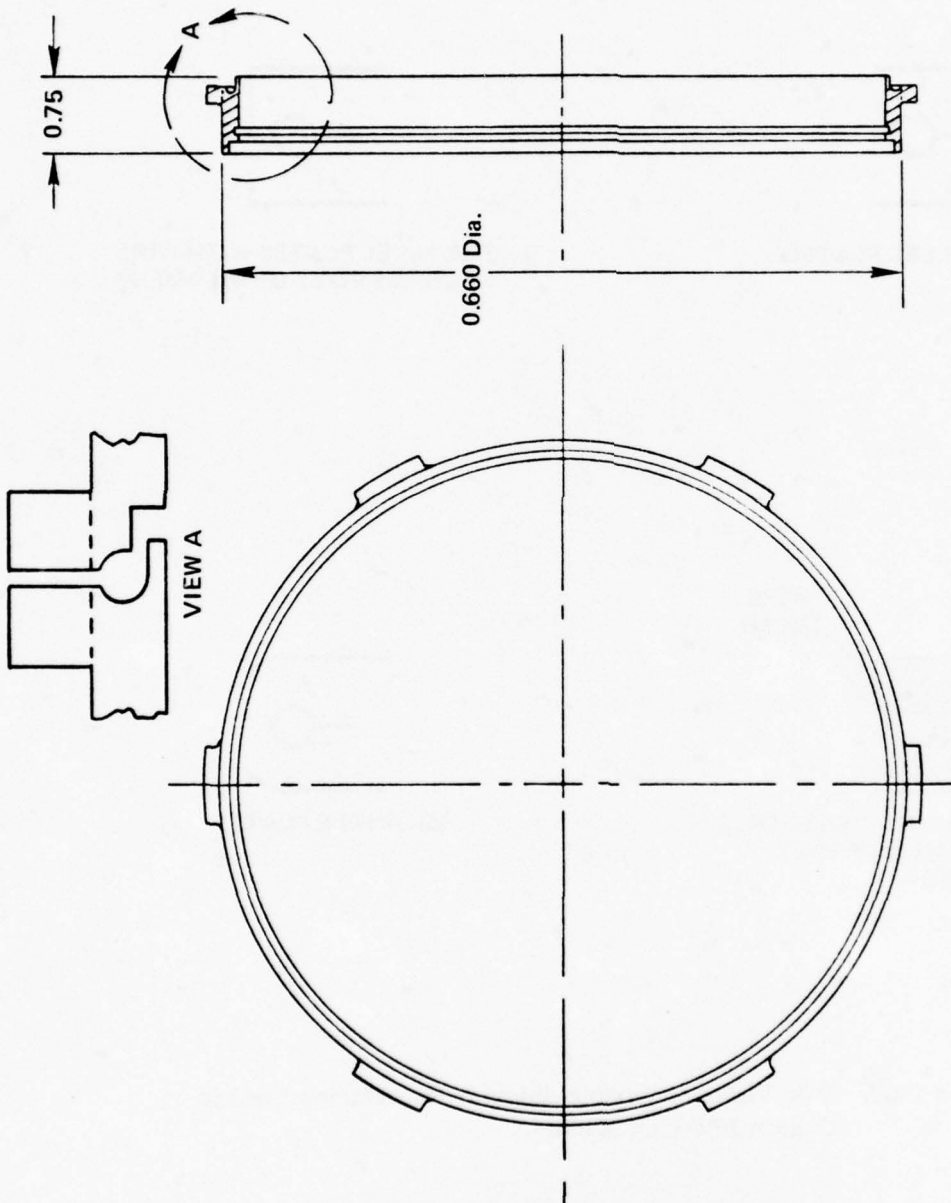
130

Figure 7-51. STP Insulating Vacuum Flange.

0.75

0.660 Dia.

A

VIEW A
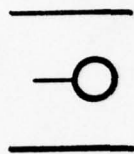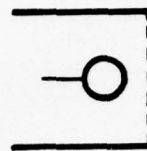
(a) PARALLEL PLATES

(b) PARALLEL PLATES WITH WIRE
MESH IN FRONT OF FILAMENT
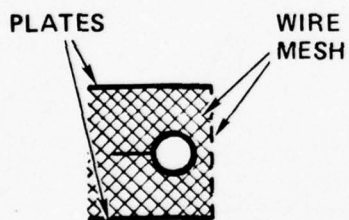
PLATES   WIRE
                MESH

(c) PARALLEL PLATES WITH
WIRE MESH ON FRONT
AND SIDES
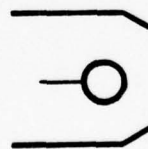
(d) ANGLE PLATES

Figure 7-52. Side Views of Various Injector Geometries Used in
Charge Injection Studies.

Figure 7-53. Summary of Results of Injector Geometry Study.

133

B-150

Figure 7-54. Photograph of the STP High Voltage Injector.

Figure 7-55. Sketch of High Voltage Injector.

135

throughs are mounted on a 6" OD vacuum flange and the entire assembly is designed to fit inside a 4 inch OD port. This large port size allows large distances between the high voltage injector components and the torus walls which are at ground potential. The feed through flang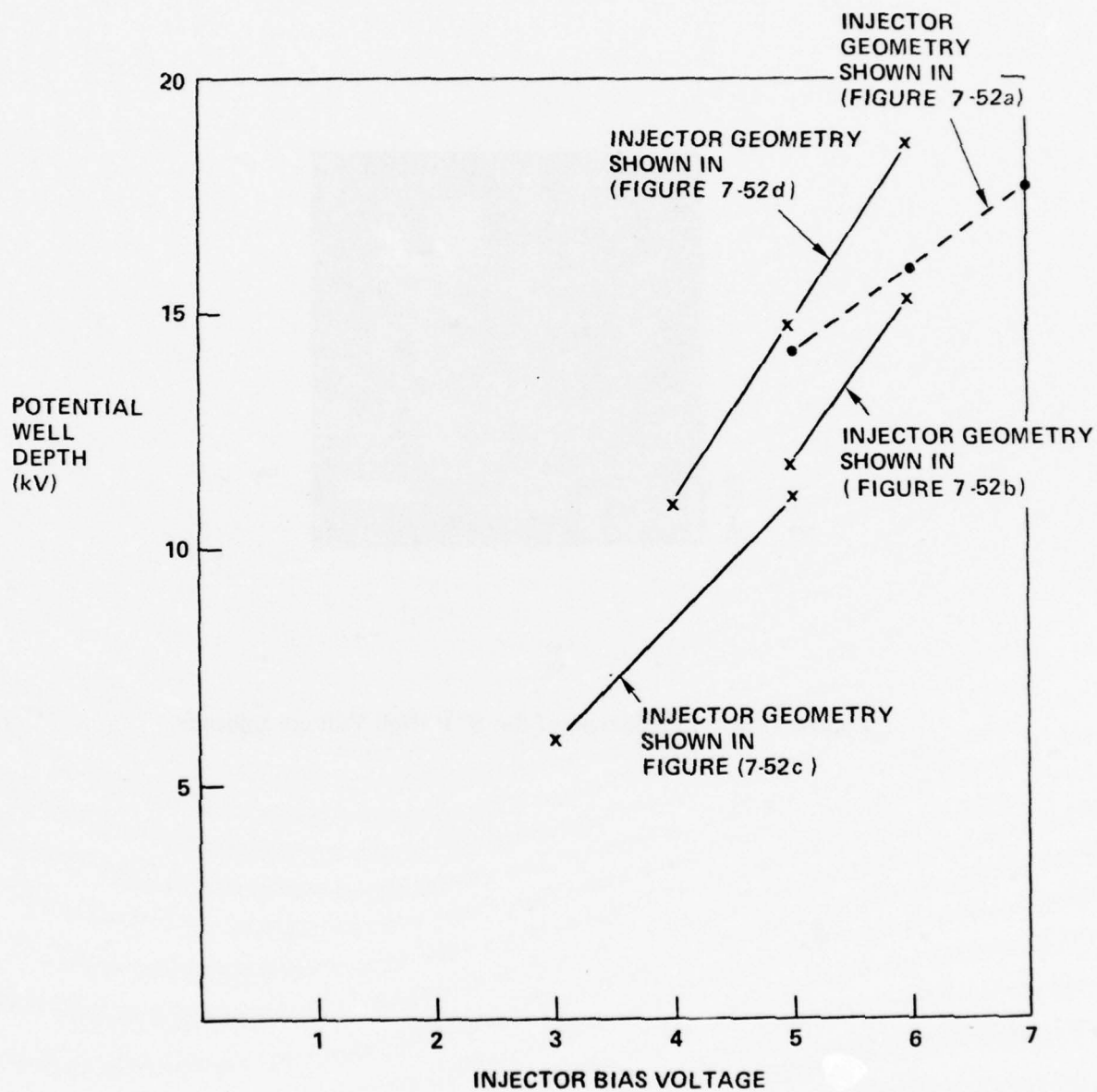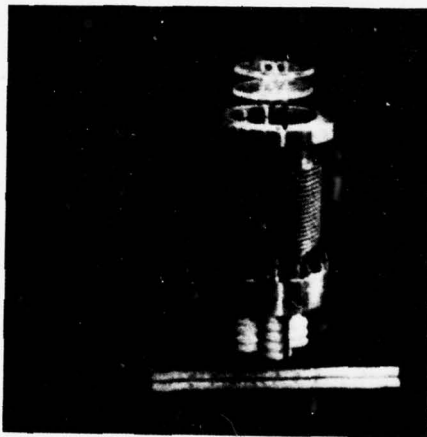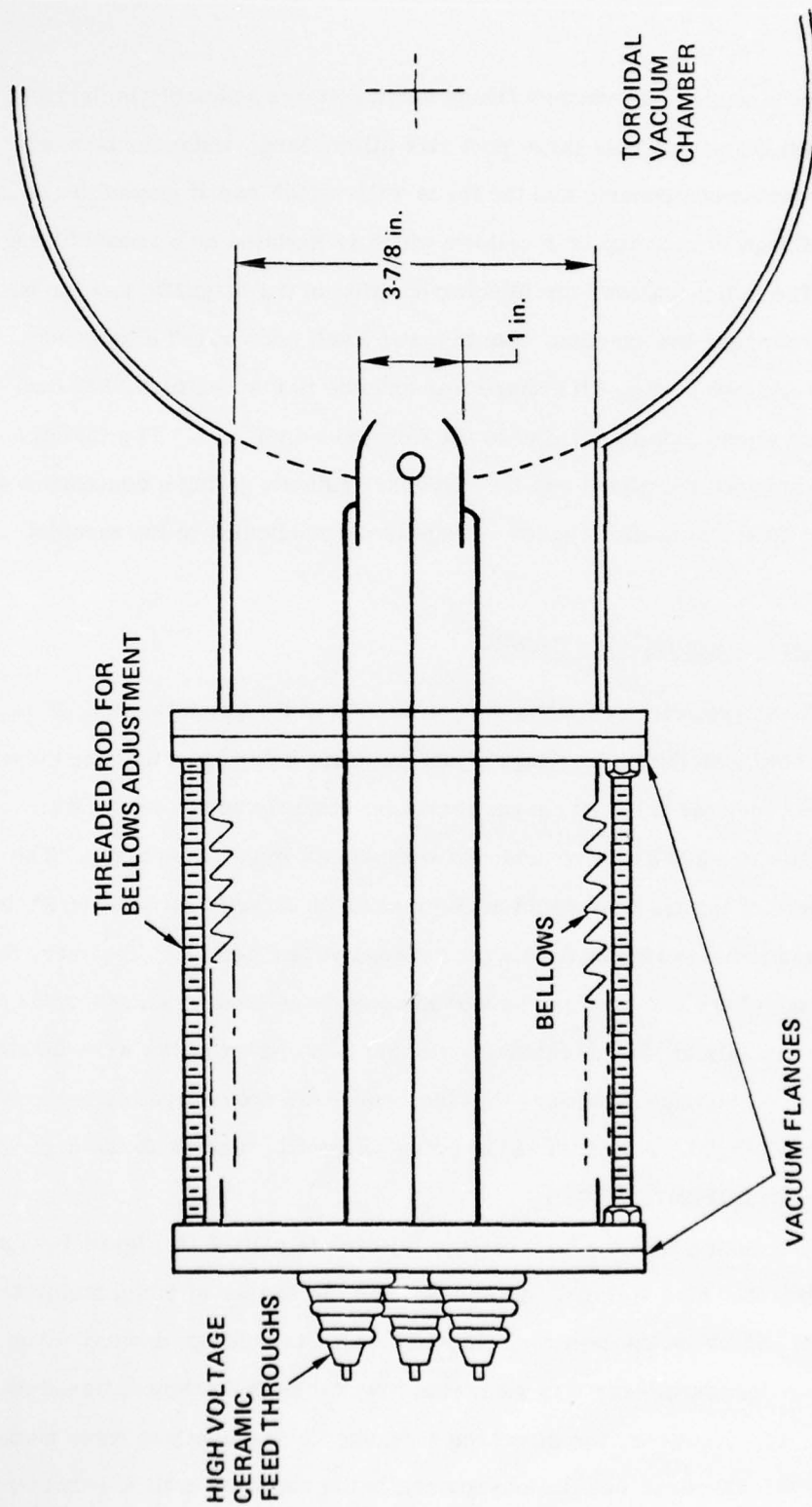e is mounted on a bellows which is mounted on a vacuum flange at the machine. The bellows allows the injector position in the magnetic field to be changed without disturbing the vacuum. The injector itself consists of a tungsten dispenser cathode and two plates. The dispenser cathode is a seven turn, 1/4 inch OD helical filament whose axis is parallel to the toroidal minor axis. The injector voltage is applied between the plates and the dispenser cathode giving a configuration where the electric field due to the injector voltage is perpendicular to the toroidal magnetic field.

7.2.6 High Voltage Injector Results

Figure 7-56 shows potential probe measurements of the potential well depth due to charge injected with the high voltage injector. This data shows that the potential well depth and hence the injected charge increases linearly with injector bias voltage. Potential wells of ~300 kV were achieved with ~35 kV injector voltages. The voltage in the center of the machine could not be measured directly above ~100 kV because the potential probes tended to flash over between 80 and 100 kV. However, the voltage at the center of the machine can be extrapolated from measurements made near the wall. In order to validate this technique a number of radial profiles were taken at various lower injector voltages to ensure that the profile did not change appreciably as the bias voltage changed. A typical radial potential profile taken with the high voltage injector is shown in Figure 7-57.

The charge injected with the high voltage injector is plotted in Figure 7-58 as a function of the injector bias voltage. As can be seen, in excess of 100 μcoulombs was obtained with ~35 kV on the injector. In some cases the charge deduced from diocotron frequency measurements was somewhat lower than that taken from potential probe measurements. However, the diocotron frequency measurements were made late in time since the diocotron oscillations generally did not start until several hundred
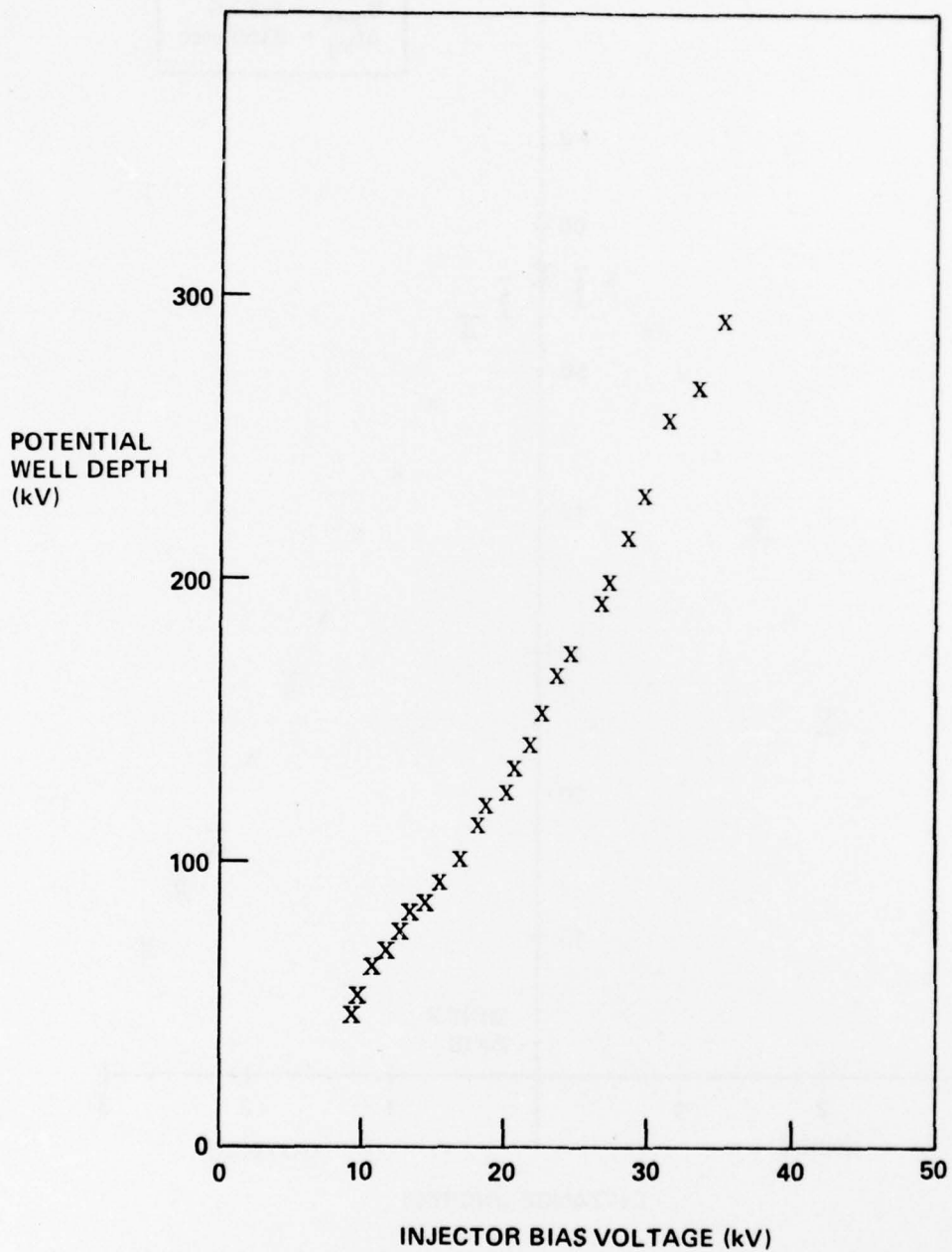
136

Figure 7-56. Potential Well Depth due to Charge Injected with the High Voltage Injector as a Function of Bias Voltage.
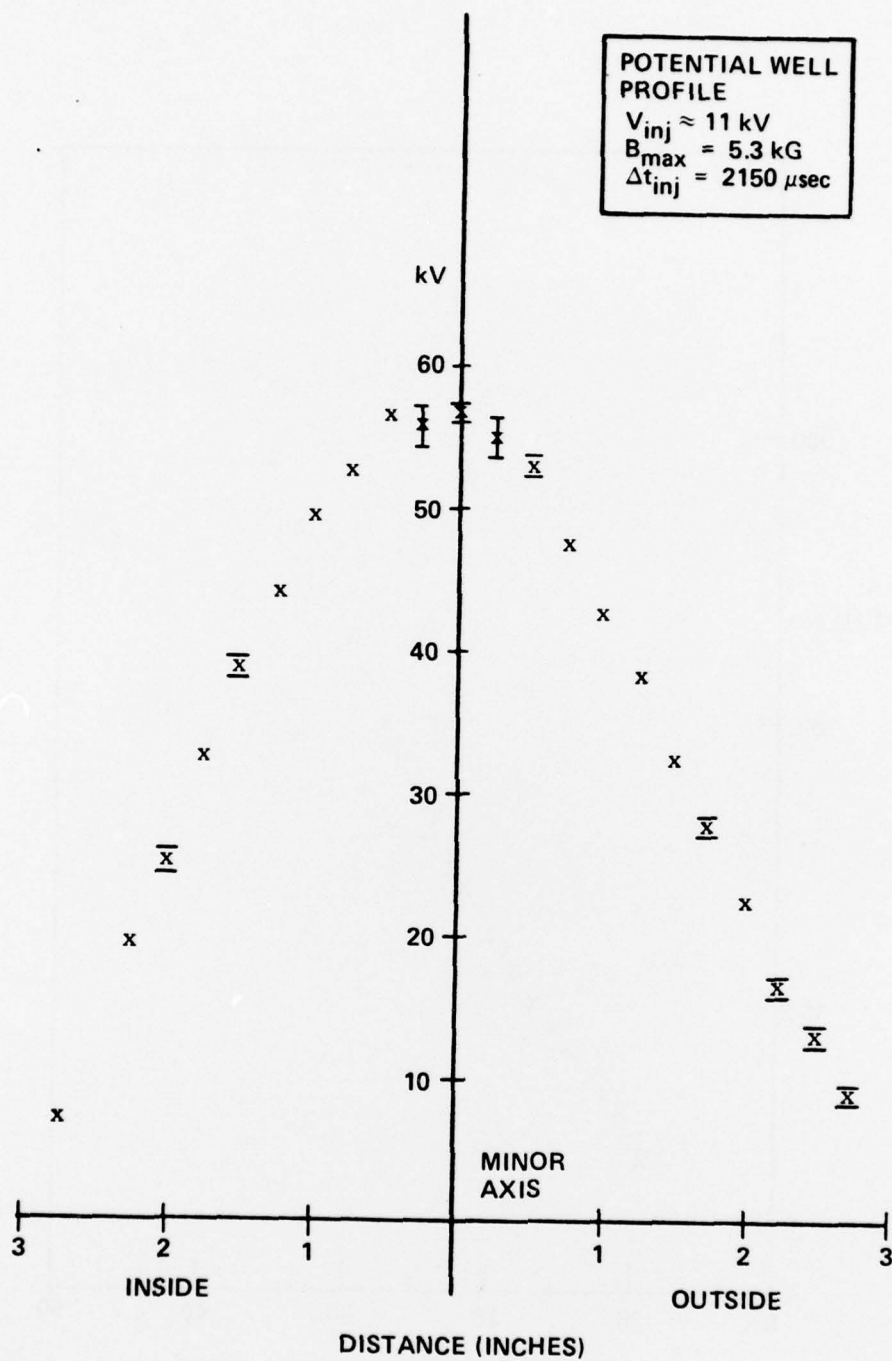
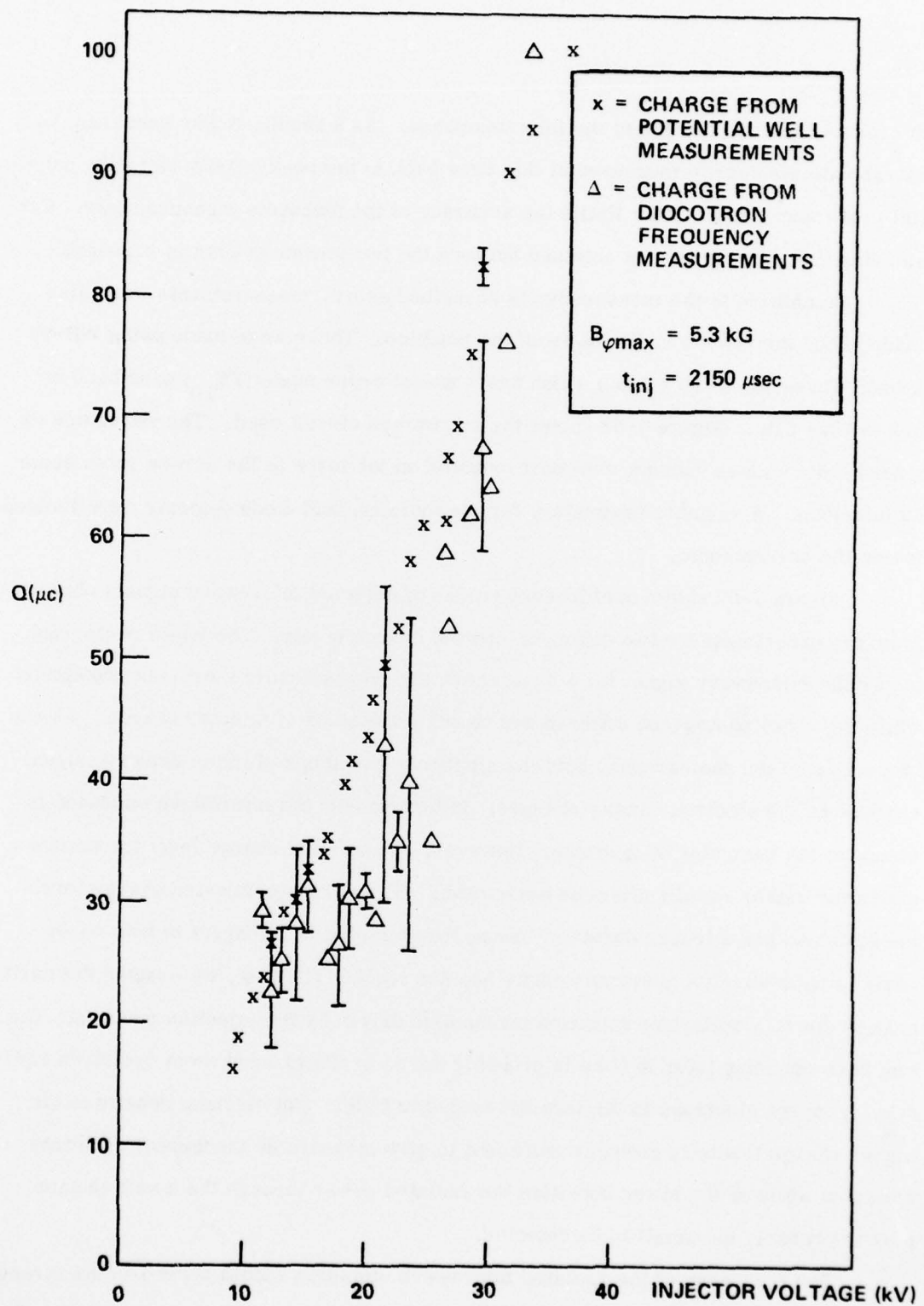Figure 7-57. Radial Potential Profile Obtained with High Voltage Injector.

138

Figure 7-58. Charge Injected with the High Voltage Injector as a Function of Injector Bias Voltage.

139

microseconds after the end of the injection phase. As a result, it was necessary to extrapolate the density measured at this time back to the peak density using the potential probe decay rate. This limits the accuracy of the diocotron measurements. Considering this, the agreement obtained between the two measurements is reasonable.

In addition to the measurements described above, measurements were also made of the microwave radiation from the machine. These were made using WR-90 x-band waveguide ($\sim 1''$ x 0.5'') which has a lowest order mode (TE_{10}) pass band of 8.2 to 12.4 GHz. Figure 7-59 shows the microwave circuit used. The waveguide extended from a glass vacuum view port mounted on the torus to the screen room some 50 feet away. A variable attenuator, ferrite isolator, and diode detector were located inside the screen room.

Figure 7-60 shows oscilloscope traces of detected microwave signals obtained from the experiment for two different injected charge levels. The upper photograph shows the microwave signal for a case where the injected charge was ~ 42 μcoulombs while the lower photograph corresponds to ~ 81 μcoulombs of injected charge. As can be seen from the photographs, both the amplitude and shape of the microwave signal changes as the electron density changes. In both cases, the microwave emission is strong at the beginning of injection. However, at the lower charge level the emission dies away rather rapidly after the early peak, while at higher injected charge levels the emission has a longer duration. Since the emission is strongest in both cases early in time when the electron density has not reached its peak, we assume the early peak is due to a collective radiation mechanism driven by the injection process. The emission occuring later in time is probably due to ordinary incoherent cyclotron radiation from the electrons in the toroidal magnetic field. The electron density at the higher charge levels is probably sufficient to give measurable incoherent cyclotron emission while at the lower densities the radiated power through the small vacuum port is probably too small to be detected.

The frequency of the radiated microwave emission should depend on the strength of the magnetic field if the emission occurs at the cyclotron frequency. The electron
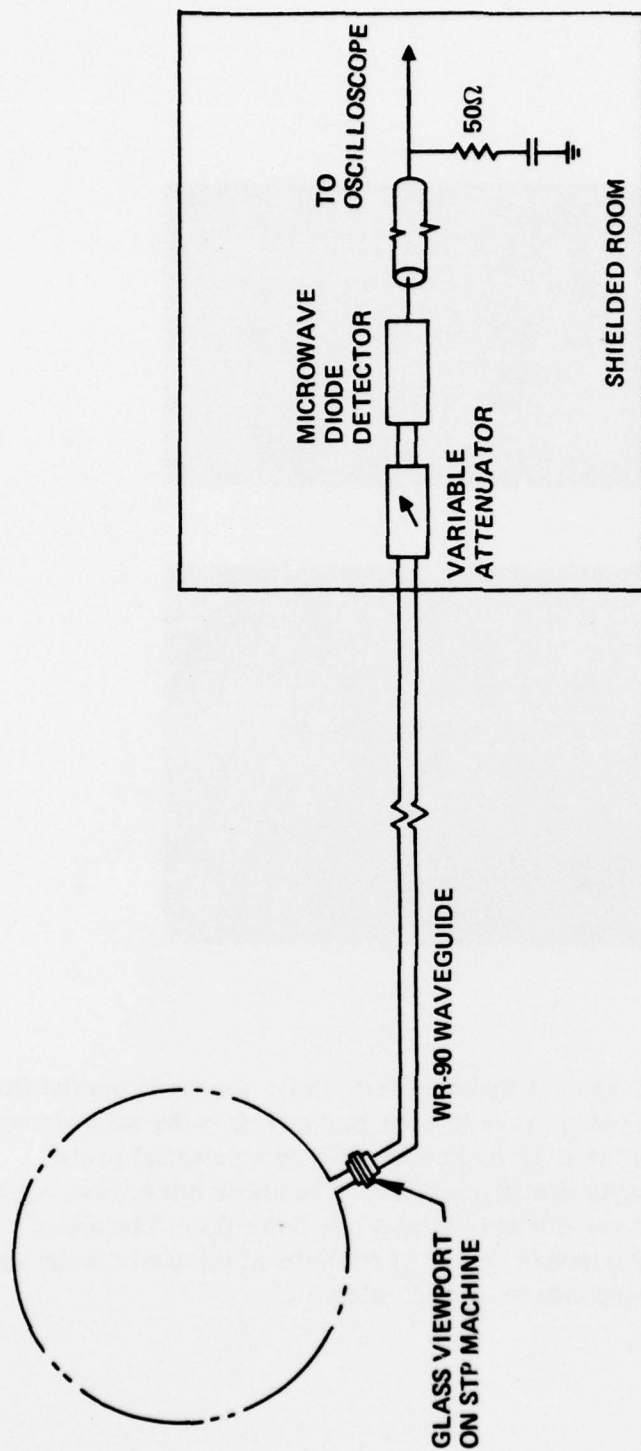
Figure 7-59. Microwave Circuit Used for Measuring Microwave Radiation From the STP Machine.

141

E-195
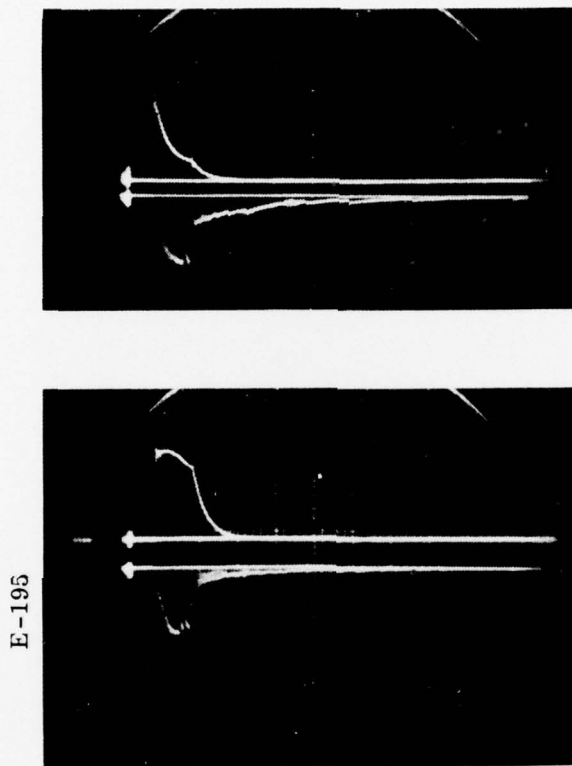
Figure 7-60. Oscilloscope Traces of Radiated Microwave Power From the STP
Machine. The upper trace in each photograph is the microwave
signal, and the lower trace in each case is a potential probe
signal. All traces are 50 μsec/div. The upper microwave signal
sensitivity is 2 mv/div and the lower is 5 mv/div. The upper
photograph corresponds to ~ 42 μCoulombs of injected change while
the lower corresponds to ~ 81 μCoulombs.

cyclotron frequency is given by

$$f_c = \frac{e}{m} \frac{B}{2\pi}$$

This corresponds to ~2.8 GHz per kilogauss of magnetic field. Thus, by changing the toroidal magnetic field in the experiment it is possible to vary the cyclotron frequency through the x-band range. Figure 7-61 shows a plot of the detected microwave signal as a function of the cyclotron frequency calculated for an electron at the minor axis of the machine as the magnetic field is varied. The magnetic field was varied both by changing the peak magnetic field and by changing the injection time, giving nearly identical results. The fact that the detected microwave power depends on the magnetic field indicates that the emission is probably cyclotron radiation.

7.2.7 Charge Acceleration Studies

The last few weeks of this year's work were devoted to charge acceleration experiments. These efforts indicated some unanticipated problems in the charge acceleration phase. Although ample charge was available to provide the $\overline{E}_r$ and $\overline{B}_\phi$ particle rotational transform to cancel the toroidal drift, and the vertical magnetic field was available for beam positioning, no large un-neutralized beam currents were established. Currents initially thought to be electron beam currents were later found to be flowing in the wall of the vacuum vessel, by-passing one of the insulating vacuum flanges which was slightly misaligned. In some cases, large currents were observed late in time due to ionization of wall material and background gas to form a plasma allowing a tokamak discharge. Figure 7-62 shows oscilloscope traces of a tokamak discharge. As can be seen, a discharge current of ~10 kA peak occurred late in time (~2msec after injection). The x-rays generated near the peak of the current pulse were found to penetrate up to ~0.25 inches of lead, indicating the presence of electrons with up to ~200 keV energy in the discharge. This implies that these electrons were contained for several thousand passes since the transformer electric field was ~0.2 volts/cm which corresponds to an energy increase of ~64 eV per transit for the electrons. The long delay before the onset of the tokamak discharge is probably the result of a slow buildup of plasma density by ionization of background

143

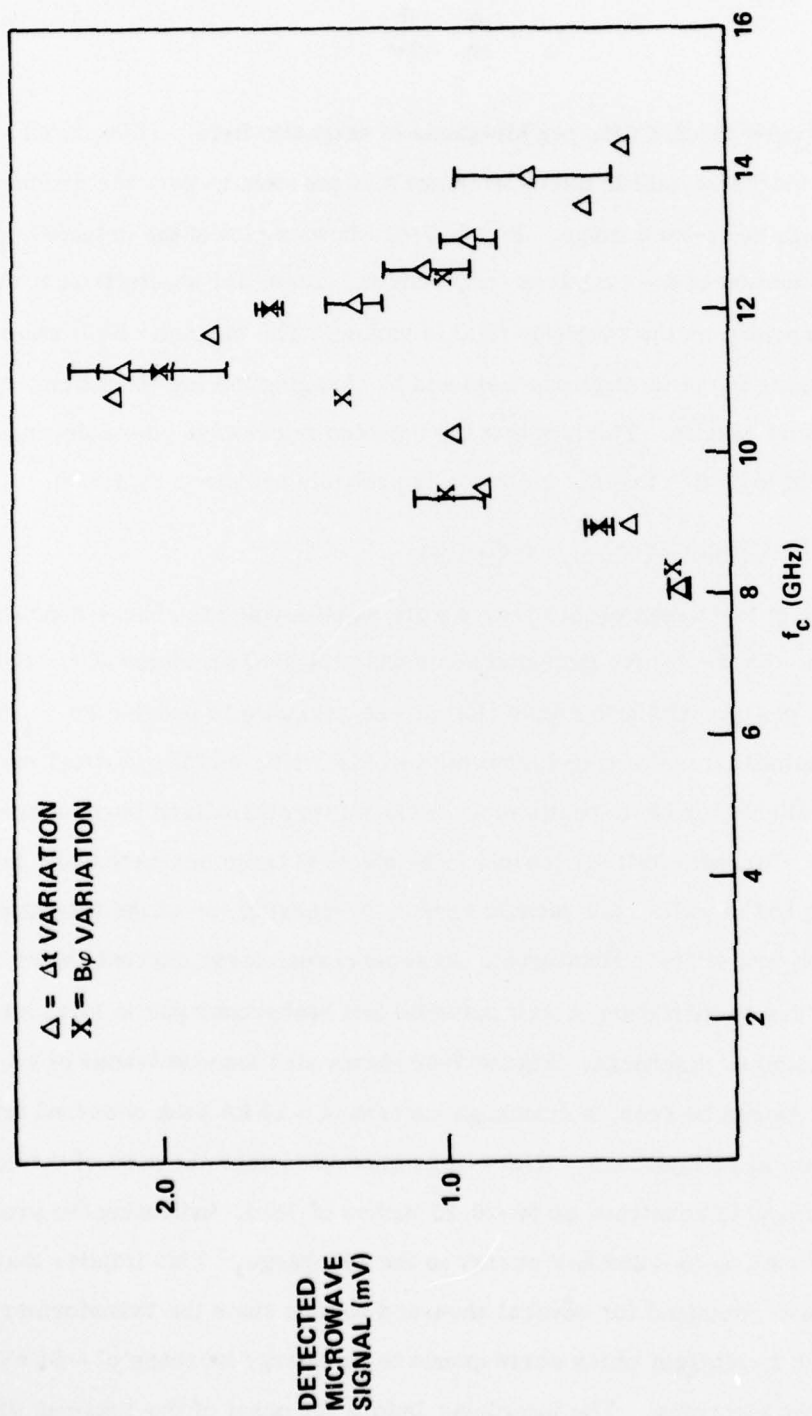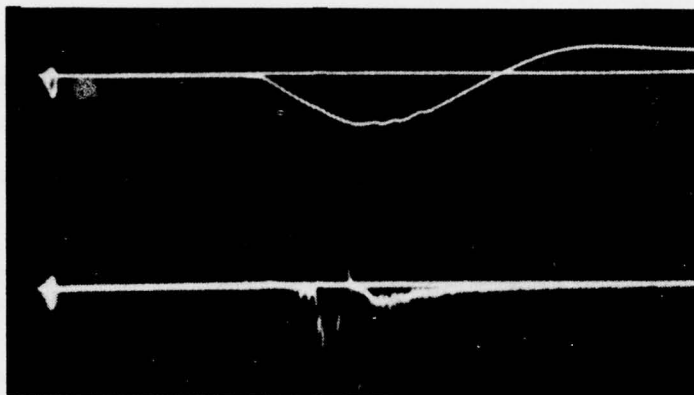Figure 7-61. Detected Microwave Signal Variation With Magnetic Field.

144

E-194

Figure 7-62. Oscilloscope Traces of a Late Time Tokamak Discharge in
the STP Machine. Upper trace: Toroidal current, 14 kA/div.
Lower trace: Scintillator - photomultiplier x-ray signal.
Horizontal sensitivity: 500 μsec/div. The oscilloscope was
triggered at injection time. The transformer electric field
was ~ 0.2 volts/cm.

145

gas and wall material. Normally, one of the insulating torus flanges (see Figure 7-51) was short circuited by ground connections between the two halves of the torus, leaving only one insulating gap in the vacuum vessel. Under these circumstances the tokamak discharges were usually observed late in time. When the ground was removed from half of the machine, thus removing the shorting path around one of the flanges, no tokamak discharge occurred. This indicates that one of the flanges drew some leakage current generating enough plasma for the tokamak discharge. This leakage current was observed to begin early in time and persist until the onset of the tokamak mode. The amplitude of this leakage current was a few hundred amps.

From the results of these experiments we conclude that the machine operates as expected in the presence of a plasma, generating a tokamak discharge, but does not generate unneutralized electron beam currents even when a large amount of charge is present. (The charge decay time is not affected by the presence of the toroidal electric field.) This suggests that the difficulties are connected with the orbits of the electrons in the unneutralized column. These orbits involve principally motion around the toroidal minor axis (due to $\overline{E} \times \overline{B}_o$ drift) so that the particles can be expected to have much greater energy perpendicular to the magnetic field than parallel to the field. Such particles would be susceptible to being trapped in small ripples in the magnetic field caused by the discrete nature of the magnetic field coils. Most of the electrons trapped in such wells would not feel the effects of the toroidal electric field since the electric field would result only in a small current even though a large amount of charge is present for several hundred microseconds after injection. This is precisely the behavior that is observed. The currents observed are ∼50 amps.

This situation can be corrected by injecting electrons with significant energy parallel to the magnetic field that they will not be trapped in magnetic wells. Such electrons would then be further accelerated by the transformer each time they passed under the insulating vacuum flanges. This injection process could be best accomplished with a relativistic injector. Figure 7-63 shows a drawing of a relativistic electron injector. Basically the device would consist of a diode driven by a marx generator. The diode is connected to the marx by a vacuum coaxial line. The insulator and marx

146

MESH ANODE

STP VACUUM VESSEL

4 IN.

8 IN.

1 IN. OD STAINLESS STEEL

9 IN.

3 IN. OD

TO PUMP

2-1/2 IN. OD GLASS

STAINLESS 4 IN. OD

LUCITE INSULATOR
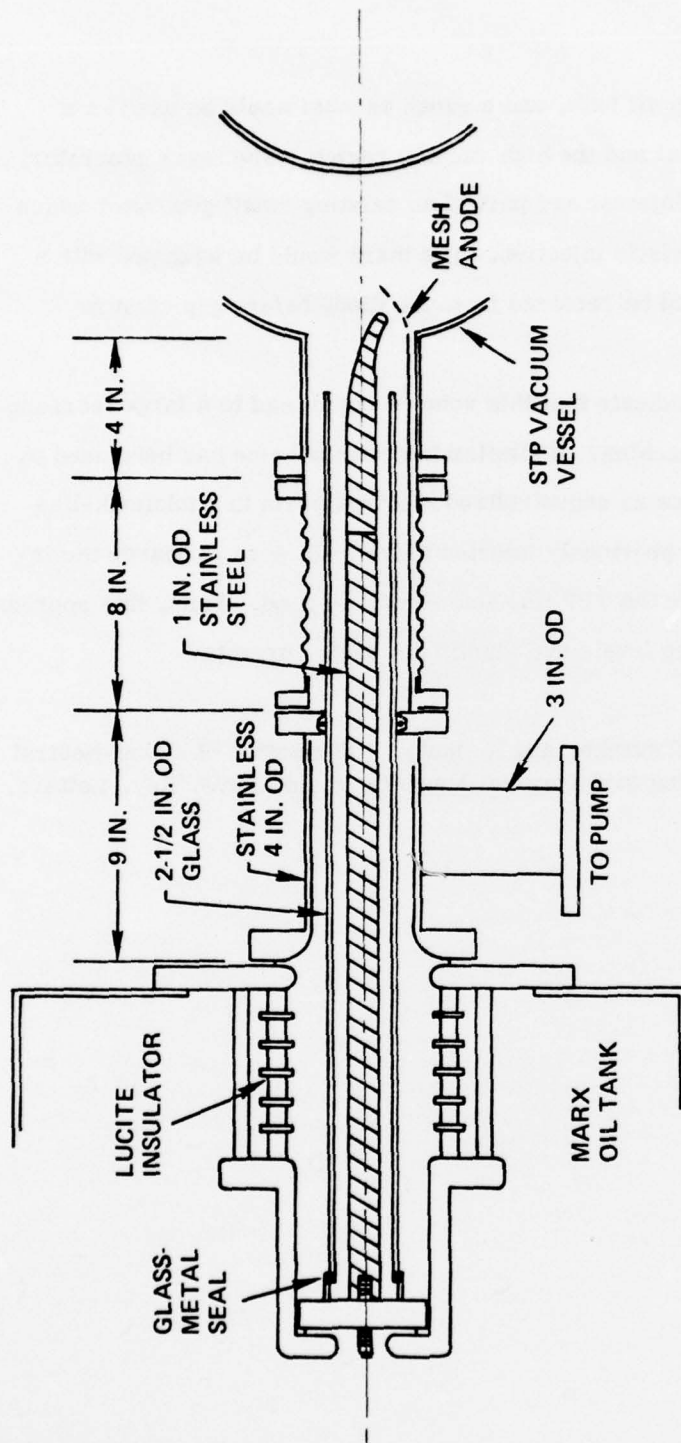
MARX OIL TANK

GLASS-METAL SEAL

Figure 7-63.   Top View of Insulator and Vacuum Coax Layout for the STP Machine.

147

generator would be located in an oil tank, and a rough vacuum would be used as a buffer region between the oil seal and the high vacuum region. The marx generator, oil tank, and insulator for this injector are part of an existing small generator which can be readily adapted to relativistic injection. The marx would be equipped with a crowbar so that the voltage could be removed from the diode before gap closure occurred.

Computer calculations indicate that this scheme could lead to a large increase in the charge level inside the machine. A similar injection scheme has been used by researchers in Japan[1] to produce an unneutralized electron beam in a tokamak-like device. With the presence of a previously injected thermionic core of charge the injection and trapping efficiency in the STP machine should be good. Thus, this approach should lead to both higher charge levels and significant beam currents.

---

[1] A. Mohri, M. Masuzake, T. Tsuzuke, and K. Ikuta. "Formation of a Non-Neutral Relativistic Electron Beam Ring in a Toroidal Magnetic Field, Phys. Rev. Letters, 34, 574 (1975).

DISTRIBUTION LIST

DEPARTMENT OF DEFENSE

Defense Documentation Center
Cameron Station
12 cy ATTN: TC

Director
Defense Intelligence Agency
    ATTN: DTICI, Robert T. Rubenstein

Director
Defense Nuclear Agency
 3 cy ATTN: TITL, Tech. Library
    ATTN: TISI, Archives
    ATTN: RAEV
    ATTN: STVL
    ATTN: DDST

Dir. of Defense Rsch. & Engineering
Department of Defense
    ATTN: S&SS (OS)

Commander
Field Command
Defense Nuclear Agency
    ATTN: FCPR

Director
Joint Strat. Target Planning Staff, JCS
    ATTN: JSAS

Chief Livermore Division, Field Command, DNA
Lawrence Livermore Laboratory
    ATTN: FCPRL

DEPARTMENT OF THE ARMY

Commander
BMD System Command
    ATTN: SSC-TEN

Dep. Chief of Staff for Rsch. Dev. & Acq.
Department of the Army
    ATTN: DAMA-CSM-N

Commander
Harry Diamond Laboratories
    ATTN: DRXDO-RBH, Paul A. Caldwell
    ATTN: DRXDO-RCC, John A. Rosado
    ATTN: DRXDO-TI, Tech. Lib.
    ATTN: DRXDO-NP

Commander
Picatinny Arsenal
    ATTN: SMUPA-ND-N-E

Commander
Redstone Scientific Information Center
US Army Missile Command
 3 cy ATTN: Chief, Documents

Commander
US Army Missile Command
    ATTN: DRCPM-PE-EA

DEPARTMENT OF THE ARMY (Continued)

Commander
US Army Nuclear Agency
    ATTN: ATCN-W

Commander
US Army Test & Evaluation Command
    ATTN: DRSTE-EL

DEPARTMENT OF THE NAVY

Chief of Naval Operations
Navy Department
    ATTN: Robert A. Blaise

Commander
Naval Electronic Systems Command
Naval Electronic Systems Command Hqs.
    ATTN: Code 5032

Commanding Officer
Naval Intelligence Support Center
    ATTN: NISC-45

Director
Naval Research Laboratory
    ATTN: Code 7701, Jack D. Brown
    ATTN: Code 5410, John Davis
    ATTN: Code 7770, Gerald Cooperstien

Officer-in-Charge
Naval Surface Weapons Center
    ATTN: Code WA501, Navy Nuc. Prgms. Off.
    ATTN: Code WR43

Commander
Naval Weapons Center
    ATTN: Code 533, Tech. Lib.

DEPARTMENT OF THE AIR FORCE

AF Weapons Laboratory, AFSC
    ATTN: DYP
    ATTN: SUL
    ATTN: CA
    ATTN: ELC
    ATTN: NT

Hq. USAF/RD
    ATTN: RDQSM

SAMSO/DY
    ATTN: DYS

SAMSO/IN
    ATTN: IND, Maj Darryl S. Muskin

SAMSO/MN
    ATTN: MNNH

SAMSO/SK
    ATTN: SKF, Peter H. Stadler

ENERGY RESEARCH & DEVELOPMENT ADMINISTRATION

University of California
Lawrence Livermore Laboratory
     ATTN: L-18
     ATTN: John Nuckolls, A Div., L-545
     ATTN: Tech. Info. Dept. L-3
     ATTN: L-153

Sandia Laboratories
     ATTN: Doc. Con. for 3141, Sandia Rpt. Coll.
     ATTN: Doc. Con. for 5240, Gerald Yonas

DEPARTMENT OF DEFENSE CONTRACTORS

Avco Research & Systems Group
     ATTN: Research Lib., A830, Rm. 7201

The BDM Corporation
     ATTN: Technical Library

The Boeing Company
     ATTN: Aerospace Library

Dikewood Industries, Inc.
     ATTN: L. Wayne Davis

EG&G, Inc.
Albuquerque Division
     ATTN: Technical Library

Ford Aerospace & Communications Corp.
     ATTN: Library
     ATTN: Donald R. McMorrow, MS G30

Ford Aerospace & Communications Operations
     ATTN: Tech. Info. Section

General Electric Company
Space Division
Valley Forge Space Center
     ATTN: Joseph C. Peden, VFSC, Rm. 4230M

General Electric Company
TEMPO-Center for Advanced Studies
     ATTN: DASIAC

Institute for Defense Analyses
     ATTN: IDA Librarian, Ruth S. Smith

ION Physics Corporation
     ATTN: H. Milde

IRT Corporation
     ATTN: R. L. Mertz

Jaycor
     ATTN: Eric P. Wenaas

Jaycor
     ATTN: Robert Sullivan

Kaman Sciences Corporation
     ATTN: Albert P. Bridges
     ATTN: John R. Hoffman
     ATTN: Walter E. Ware
     ATTN: Donald H. Bryce

Lockheed Missiles & Space Company, Inc.
     ATTN: Lloyd F. Chase

DEPARTMENT OF DEFENSE CONTRACTORS (Continued)

Maxwell Laboratories, Inc.
     ATTN: Alan C. Kolb
     ATTN: A. Richard Miller
     ATTN: Peter Korn
     ATTN: W. Clark
     ATTN: A. Mondelli
     ATTN: N. Rostoker

McDonnell Douglas Corporation
     ATTN: Stanley Schneider

Mission Research Corporation
     ATTN: Conrad L. Longmire
     ATTN: William C. Hart

Mission Research Corporation-San Diego
     ATTN: V. A. J. Van Lint

Northrop Corporation
Northrop Research & Technology Center
     ATTN: Library

Northrop Corporation
Electronic Division
     ATTN: Vincent R. DeMartino

Physics International Company
     ATTN: Doc. Con. for Sidney D. Putnam
     ATTN: Doc. Con. for Ian D. Smith
     ATTN: Doc. Con. for Bernard H. Bernstein
     ATTN: Doc. Con. for Charles H. Stallings
     ATTN: Doc. Con. for Philip W. Spence

Pulsar Associates, Inc.
     ATTN: Carleton H. Jones, Jr.

R & D Associates
     ATTN: Leonard Schlessinger
     ATTN: C. MacDonald
     ATTN: William R. Graham, Jr.

Science Applications, Inc.
     ATTN: J. Robert Beyster

Simulation Physics, Inc.
     ATTN: Roger G. Little

Stanford Research Institute
     ATTN: Setsuo Dairiki

Systems, Science & Software, Inc.
     ATTN: David A. Meskan

Systems, Science & Software, Inc.
     ATTN: Andrew R. Wilson

Texas Tech. University
     ATTN: Travis L. Simpson

TRW Defense & Space Sys. Group
     ATTN: Tech. Info. Center/S-1930

Vought Corporation
Michigan Division
     ATTN: Tech. Lib.